Washington University in St. Louis
Washington University Open Scholarship

Arts & Sciences Electronic Theses and Dissertations | Arts & Sciences

Summer 8-15-2015

Effects of Quark Matter on the Structural and Observational Properties of Compact Stars

Sophia Han
Washington University in St. Louis

Follow this and additional works at: https://openscholarship.wustl.edu/art_sci_etds

Recommended Citation
Han, Sophia, "Effects of Quark Matter on the Structural and Observational Properties of Compact Stars" (2015). *Arts & Sciences Electronic Theses and Dissertations*. 651.
https://openscholarship.wustl.edu/art_sci_etds/651

This Dissertation is brought to you for free and open access by the Arts & Sciences at Washington University Open Scholarship. It has been accepted for inclusion in Arts & Sciences Electronic Theses and Dissertations by an authorized administrator of Washington University Open Scholarship. For more information, please contact digital@wumail.wustl.edu.

WASHINGTON UNIVERSITY IN ST. LOUIS

Department of Physics

Dissertation Examination Committee:
Mark Alford, Chair
Willem Dickhoff
Francesc Ferrer
Michael Ogilvie
Lee Sobotka

Effects of Quark Matter on the Structural and Observational Properties of Compact Stars

by

Sophia Han

A dissertation presented to the
Graduate School of Arts and Sciences
of Washington University in
partial fulfillment of the
requirements for the degree
of Doctor of Philosophy

August 2015

St. Louis, Missouri

© 2015, Sophia Han

Contents

List of Figures

List of Tables

Acknowledgments

First of all, I would like to extend my deepest gratitude and appreciation to my advisor Prof. Mark Alford, for introducing me to the research field of compact stars and cold dense matter and guiding me through the phenomenologies and theoretical aspects of nuclear astrophysics. I thank him for years of support, encouragement and patience in mentoring me from initial ideas to final fulfillment throughout the work, and I feel very fortunate and privileged to be his student. The heartwarming and engaging atmosphere in his group have made the five years I spent here more than a nice memory and wonderful experience.

Furthermore, special thanks go out to Dr. Kai Schwenzer who has significantly contributed to my last project, where he steered me to understand loads of fundamental concepts and practical technics, and always volunteered to help me out with any queries. I also wish to convey my sincere thanks to Sanjay Reddy, Madappa Prakash, Fiorella Burgio, Gabriele Taranto and Dario Zappala for earnest collaboration; and to Kota Masuda, David Blaschke, Pawel Haensel, Jurgen Schaffner-Bielich and Mikhail Gusakov for enlightening communications.

I wish to thank Prof. Ogilvie, Prof. Ferrer, Prof. Dickhoff and Prof. Sobotka for serving on my dissertation committee, taking their time to review this manuscript and for their invaluable comments and suggestions.

I warmly thank all professors, post-doctorates, fellow graduate students and guest speakers attending our nuclear-particle joint group meetings, for their inspiring thoughts and conversations having exposed me to the plentifulness of physics. I am grateful to the adorable physics community at Washington University in St. Louis; there could not have been a more enjoyable stay here without your hospitality and kindness.

Finally many, many thanks to my beloved parents in China for their unwavering support of everything I do over the years, and thanks to every friend I have made through my Ph.D. adventure.

This work was supported in part by the Offices of Nuclear Physics and High Energy Physics of the Office of Science of the U.S. Department of Energy under contracts #DE-FG02-91ER40628, #DE-FG02-05ER41375, and by the DoE Topical Collaboration "Neutrinos and Nucleosynthesis in Hot and Dense Matter", contract #DE-SC0004955.

Sophia Han

Washington University in St. Louis
August 2015

ABSTRACT OF THE DISSERTATION

Effects of Quark Matter on the Structural and Observational Properties of Compact Stars

by

Sophia Han

Doctor of Philosophy in Physics

Washington University in St. Louis, August 2015

Professor Mark Alford, Chair

In the interior of a neutron star, matter is ultra-dense with its density as high as a few times the nuclear saturation density, and extremely cold compared to its chemical potential. As a result, it is the most likely place where the theoretically-predicted strange quark matter might exist. The aim of this thesis is to reveal how the strange quark matter could influence the static properties and dynamic behaviors of compact stars. This is of great importance because it allows us to draw conclusions about the phase diagram of matter at extreme density, by investigating observable properties of compact stars despite uncertainties in their detailed structures. By studying the microscopic physics of dense matter such as charge-separation phase, hadron-quark conversion and strangeness diffusion process, and applying a generic parametrization of high-density equation of states, we explore implications about mass-radius relationship, r-mode damping and spin evolution etc. of the star.

In the first part of this thesis we calculate the equation of state (EoS) of the mixed phase in strangelet dwarfs, and obtain the mass-radius relation by solving Tolman-Oppenheimer-Volkoff (TOV) equation. In the second and third parts, we first study the mass-radius

relation of hybrid stars with a sharp interface between nuclear and quark matter by using the generic "constant speed of sound" (CSS) parameterization, and obtain the phase diagram of possible forms of the mass-radius relation. We then apply the parametrization to the Field Correlator Method (FCM) model of quark matter and express observational constraints as constraints on the CSS parameters. In the fourth part, we propose a novel mechanism for the saturation of unstable oscillation modes in multi-component compact stars based on the periodic conversion between different phases, and study in detail the case of r-modes in a hybrid star with a sharp interface, giving the saturation amplitude and its range of validity to predict observational outcomes.

Chapter 1

Introduction

Cold, ultra-dense matter lies in the hadronic sector of phase diagram in quantum chromodynamics (QCD), and compact stars in the universe are the only available laboratories for exploring its underlying physics. There has been much work on a plausible form for the equation of state (EoS) of nuclear matter at densities above nuclear density, using models of the nuclear force that are constrained by existing scattering data (see, for example, [9, 10]). At asymptotically high densities we expect to find the color-flavor-locked (CFL) phase of color-superconducting quark matter [2], but the nature of matter at intermediate densities still remain unknown because terrestrial laboratories could not create cold dense matter, and numerical calculations using lattice QCD are stymied by the fermion sign problem (see, for example, [11, 12, 13, 14]). Strange quark matter consisting up, down and strange quarks is conjectured to form droplets (strangelets or quark stars), or occur in the interior of neutron stars which gives rise to hybrid stars, depending on the assumption that whether strange quark matter is stable at zero pressure (strange matter hypothesis) or only at high pressure[15, 16, 17, 18]. It is most promising to use observations of compact stars to find observable signatures of strange quark matter and test predictions from theoretical models. For example, measurements of the masses or radii of neutron stars can strongly constrain the

dense matter equation of state (EoS), i.e., the energy density as a function of the pressure, and consequently the interior composition of neutron stars. One such example is shown in Fig. 1.1, where the recent discovery of a 2 $M_\odot$ heavy neutron star [1] rules out all sets of EoSes that cannot support a maximum mass higher than the observed value. This single high mass value indicates that a transition to quark matter in neutron-star cores can occur at densities comparable to the nuclear saturation density only if the quarks are strongly interacting and are color superconducting [19]. Many aspects of neutron star structure depend on specific equation of state parameters in a model-independent fashion, which necessitate a generic description that can be more easily applied to convey observational constraints.

Among the dynamical properties of neutron stars, cooling rate and spin frequency are also sensitive to the characteristics of phase of matter in the interior. The cooling of a compact star is intrinsically connected to its microscopic composition, and therefore different microscopic models might lead to different thermal evolutions. The extremely accurate timing observations of neutron stars that are visible as millisecond radio pulsars come out as a puzzle for the existence of r-modes [20], which are gravitationally unstable unless there are enough damping that prevents it from growing and spinning down the star.

In the following sections of this chapter we first give an introduction to strange quark matter in the context of the QCD phase diagram, and then describe the compact star properties and at the end we explain the r-mode oscillations in neutron stars.

In Chap. 2 of this thesis, we studied pure quark matter in bulk and crystal phases and applied them to calculate the mass-radius relation of stars they form, in the context of the strange matter hypothesis [15, 16, 21], that the ground state of strong interaction at zero pressure might be the de-confined quark matter rather than nuclear matter. We used a model-independent parameterization of uniform quark matter equation of states (EoS)

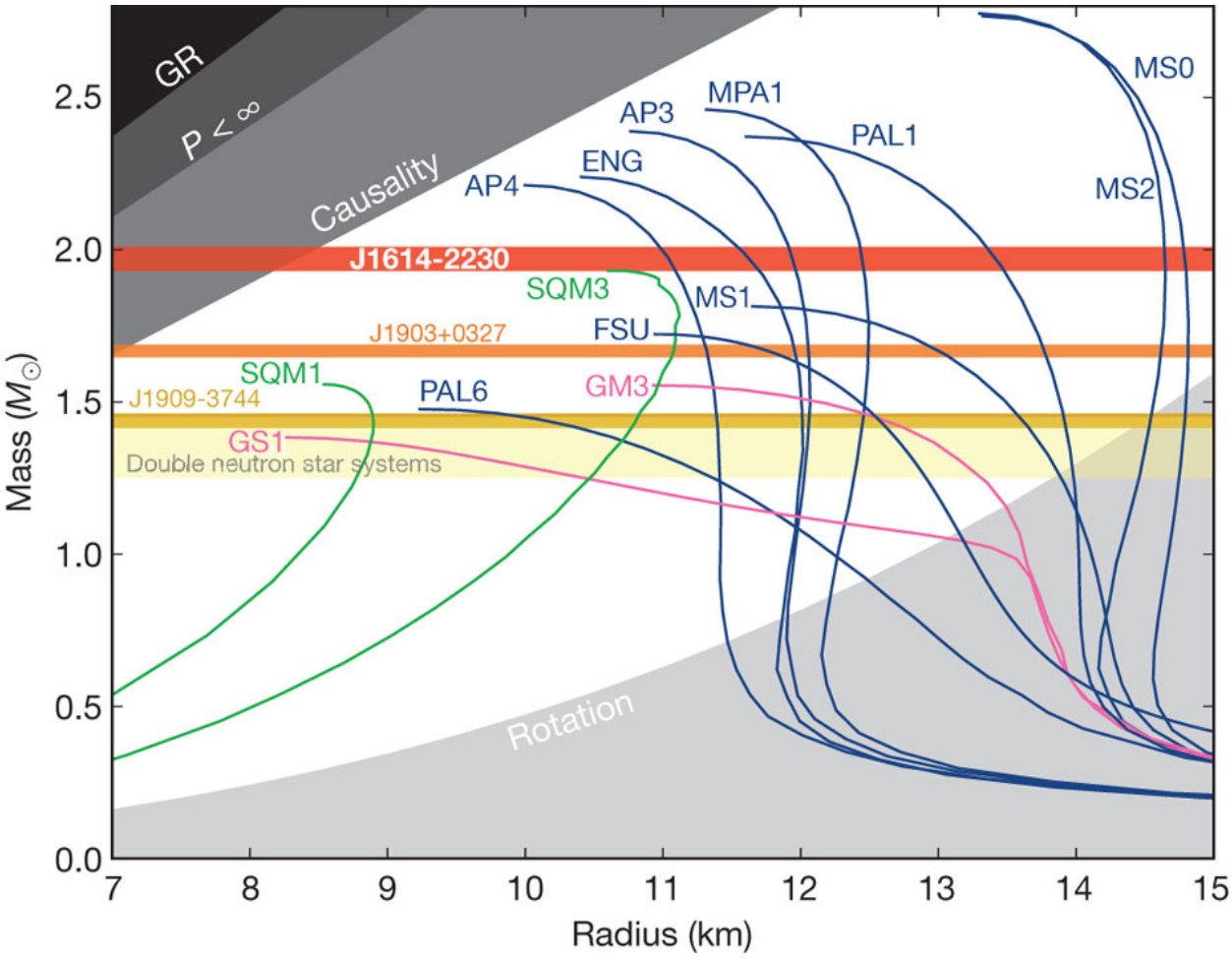

Figure 1.1: Plot showing non-rotating mass versus physical radius for several typical EoSes [1]. Any EoS line that does not intersect the J1614-2230 band is ruled out by this measurement.

based on the fact that the chemical potential for negative electric charge is much less than the quark chemical potential, and obtained crystal phase EoS by dividing the lattice into Wigner-Seitz cells and calculating the pressure at the edge of a cell and its energy density. Combining the results of both phases we produced the mass-radius relation of a "strange star-strangelet dwarf" sequence which is the strange matter equivalent of previously-studied "neutron star-white dwarf" sequence. Strangelet dwarfs are candidates for massive compact halo objects. Gravitational microlensing surveys [22] can impose a limit on the density and

distribution of such planetary mass objects in our universe, and along with our results it will help reveal information about both mass and radius.

In Chap. 3 and Chap. 4, we used a generic parametrization of constant-speed-of-sound quark matter EoS, assuming a first-order phase transition between nuclear and quark matter with a sharp interface. We obtain the phase diagram of possible stable/unstable branches of hybrid stars, and our parametrization gives rise to hybrid stars with above two solar masses which is compatible with recent observations [1, 23]. The most striking feature of this work is testing models of quark matter which can be characterized in terms of our parameters and their predictions for hybrid stars should follow their position on our phase diagram. We applied our method to the Field Corrrelator Method (FCM) model of quark matter, showing that the FCM EoS can be accurately represented by the CSS parametrization, and we display the mapping between the FCM and CSS parameters.

In Chap. 5, we calculate the dissipation of oscillations of hybrid stars due to growth and contraction of its quark matter core, which is novel in both mechanism and approach. Analysis of the energy dissipation due to periodic quark-hadron burning at the sharp interface is done in a steady-state approximation [24], that the interface moves at a speed constrained by applied oscillation of densities. In the damping of unstable r-mode oscillations we find that this phase-conversion mechanism can saturate r-mode at fairly low amplitude $O(10^{-12} - 10^{-10})$ for typical hybrid star models, much better than that required by current pulsar data $O(10^{-8} - 10^{-7})$, which cannot be explained by all other known mechanisms proposed so far. We hope that this prediction of r-mode saturation amplitude can help find a signature of the presence of quark cores in neutron stars, and along with measurements of or bounds on temperature of millisecond pulsars provide means to distinguish between ordinary neutron stars/strange quark stars and hybrid stars. One direct application of our

results is to any compact star models of different component phases, and our discussion on a sharp interface can also be extended to the pasta phase and the inner crust region which might further enhance the dissipation. Furthermore due to the extreme efficient damping in our mechanism, patterns of r-mode itself might be modified which worth studying in the future.

1.1 Physics of Strange Quark Matter

Quark matter was convinced of soon after the realization that quarks, the constituents of nucleons, are asymptotically free. At the extreme of asymptotic momentum transfer, density, or temperature, quarks are free of interaction. Under such circumstances the individuality of nucleons is lost, and the quarks of nuclear matter are free to explore a much large "colorless" region of space referred to quark matter. In this case, there is a critical pressure and an associated critical density, and when nuclear matter (made of protons and neutrons) is compressed beyond this density, the protons and neutrons dissociate into quarks, yielding quark matter (probably strange matter). The phase diagram of quark matter is not well known, either experimentally or theoretically. A commonly conjectured form of the phase diagram is shown in the Fig. 1.2, where different phases of quark matter are shown at different temperatures T, and quark chemical potentials μ [2].

Along the vertical axis the temperature rises, taking us through the crossover from the hadronic gas, in which quarks are confined into neutrons and protons, to the quark gluon plasma (QGP): thermal fluctuations break up the pions, and we find a gas of quarks, antiquarks, and gluons, as well as lighter particles such as photons, electrons, positrons, etc. Following this path corresponds to traveling far back in time, to the state of the universe

shortly after the big bang (where there was a very tiny preference for quarks over antiquarks). Heavy ion colliders at CERN and Brookhaven are probing the high temperature region of the QCD phase diagram by colliding heavy nuclei at ultra-relativistic energies. In these experiments one expect to create a quark-gluon plasma at least for a short period of time.

Increasing the quark chemical potential from zero keeping the temperature low, we move into a phase of more and more compressed nuclear matter and the density rises from the onset of nuclear matter through the transition to quark matter. Following this path corresponds to burrowing more and more deeply into a neutron star, although it is not known whether their cores are dense enough to reach the quark matter phase. At ultra-high densities we expect to find the color-flavor-locked (CFL) phase of color-superconducting quark matter. At intermediate densities we expect some other phases (labelled "non-CFL quark liquid" in the figure) whose nature is presently unknown, and they might be other forms of colorsuperconducting quark matter, or something different. The line that rises up from the nuclear/quark matter transition and then bends back towards the vertical axis, with its end marked by a star, is the conjectured boundary between confined and unconfined phases.

A different possibility, strange matter hypothesis, is also considered which states that the critical pressure for transition to quark matter is zero, and ordinary nuclei which are droplets of nuclear matter, are actually metastable, and given enough time (or the right external stimulus) would decay into droplets of quark matter consisting of an approximately equal proportion of up, down, and strange quarks, i.e. strangelets [15, 16]. Depending on the surface tension between bulk strange matter and vacuum, strangelets might form large, neutral phases as strange stars consisting of quark matter from their core to their surface, or a neutral mixed phase of positively charged strangelet surrounding by an electronic plasma that forms a strangelet crystal lattice, could result in a more diffuse branch of compact stars

without a core of uniform matter, which is analogous to white dwarfs. In Chap. 2 we will study how the stranglet crystalline phase constructs strangelet dwarf, and examine how the mass-radius relation depending on the EoS of quark matter.

1.2 Compact Stars in the Universe

1.2.1 Evolution

Compact stars are stellar remnants when the outward radiation pressure from the nuclear fusions in the interior of a massive star can no longer resist the ever present gravitational forces. Depending primarily on the mass of the star when it formed, the very dense and compact stellar remnant it creates can be white dwarfs, neutron stars or black holes.

If the mass of the progenitors are below $8M_{\odot}$, they end up with degenerate dwarfs or, more usually, white dwarfs that are made up mainly of degenerate matter, typically, carbon and oxygen nuclei in a sea of degenerate electrons. The material in a white dwarf no longer undergoes fusion reactions, so the star has no source of energy, nor is it supported by the heat generated by fusion against gravitational collapse. It is supported only by electron degeneracy pressure, causing it to be extremely dense: it has a size comparable to the size of the Earth but a mass similar to that of the Sun. The physics of degeneracy yields a maximum mass for a non-rotating white dwarf, the Chandrasekhar limit, about 1.4 $M_{\odot}$ beyond which it cannot be supported by electron degeneracy pressure. A carbon-oxygen white dwarf that approaches this mass limit, typically by mass transfer from a companion star, may explode as a Type Ia supernova.

In stars more massive than 8 $M_\odot$ carbon burning takes place in a non-degenerate carbon oxygen core. These stars subsequently go through the next burning stages, until an iron core is formed. At that moment the energy production stops and the core can no-longer withstand the gravitational force and collapses. The released energy is partly used to eject the outer envelope in a violent event which is observable as a so-called supernova. Depending on the mass of the (iron) core and possibly other conditions such as rotation and magnetic fields, either a neutron star is formed (an object consisting mainly of neutrons, in which the gravitational force is balanced by the Fermi pressure and nuclear forces between the nuclei) or the star collapses to a black hole (an object which is so compact that no light, and thus information, can escape), when no forces are strong enough to balance the gravitational force. The density of a neutron star is incredibly large: a neutron star is more massive than the Sun, but has a typical size of 10 kilometers.

1.2.2 Mass-Radius relation and the Equation of State

The general relativistic generalization of the Newtonian hydrostatic equation is the Tolman-Oppenheimer-Volkoff equation (TOV) equation [25]

$$\begin{aligned} \frac{dp}{dr} &= -g_{\rm eff}(r)\,\epsilon(r) \\ g_{\rm eff}(r) &= \frac{GM}{r^2}\left(1+\frac{p}{\epsilon}\right)\left(1+\frac{4\pi p r^3}{M}\right)\left(1-\frac{2M}{r}\right)^{-1} \end{aligned} \tag{1.1}$$

where p, ϵ and M, given by $(dM)/(dr) = 4\pi r^2 \epsilon$, are the pressure, energy density and included mass at distance r from the center. The effective gravitational acceleration $g_{\rm eff}$ contains general relativistic corrections to its Newtonian value GM/r^2. Given the central

pressure $p(r = 0)$ and the equation of state, $\epsilon(p)$ throughout the star, the TOV equation can be solved for the pressure and energy density profile completely.

Zero pressure defines the edge of the star because zero pressure can support no material against the gravitational attraction from within, and the stellar mass is determined by $M \equiv 4\pi \int_0^R \epsilon(r) r^2 dr$. For each possible EoS, there is a unique family of stars parametrized by the central pressure with mass $M(p_{cent})$ and radius $R(p_{cent})$. For a vast range of central pressures spanning many orders of magnitude, a neutron star-white dwarf sequence is shown in Fig. 1.3.

Stable white dwarfs are supported against gravitational collapse by the pressure of degenerate electrons. With increasing pressures the electron Fermi energy rises until at some point it becomes more favorable for electrons to be captured by protons via inverse beta decay. The supporting pressure of the relativistic electrons is replaced by the fermi pressure of degenerate neutrons, which stabilize light neutron stars against collapse. For more massive stars with higher densities, the repulsion of nuclear force at short range adds additional resistance to compression, before reaching the maximum mass on the neutron star branch beyond which stars collapse to black holes. As we can see from the TOV solutions, underlying microphysics determining the EoS is reflected on global properties such as mass and radius of the star, which accompanying observations put constraints on theoretical models of cold dense matter.

In contrast to the static properties of compact stars which only depend on the equation of state of matter, dynamic properties also depend on the low energy degrees of freedom and thereby might be able to discriminate more efficiently between different forms of strongly interacting matter. One of the dynamic properties of dense matter is viscosity, which determines the damping of mechanical perturbations, and a particularly important application is to the damping of r-mode oscillations of compact stars.

1.2.3 R-modes of neutron stars

Different oscillation modes penetrate to different depths inside the star. These oscillations provide information about the otherwise unobservable interiors of stars in a manner similar to how seismologists study the interior of Earth and other solid planets through the use of earthquake oscillations. R-mode oscillations are restored by the Coriolis force, due to the rotation of the star, are unstable at all rates of rotation without viscosity [4]. The fluid motion has no radial component, and is the same inside the star as the outside although smaller. In the limit of slow rotation it is well known that the r-mode frequency in the co-rotating frame is given by $\omega = 2m\Omega/l(l+1)$, where m and l are the spherical harmonic indices that describe the angular distribution of the dominant toroidal displacement vector, and Ω is the stellar spin frequency. The most unstable r-mode is that associated with $l = m = 2$, which has the familiar frequency $\omega = 2\Omega/3$ in the co-rotating frame. Fig. 1.4 depicts the most unstable $l = m = 2$ r-mode pattern in terms of the velocity flows.

The amplitude of the r-mode oscillations evolves with time dependence $e^{i\omega t - t/\tau}$, where ω is the real part of the frequency of the r-mode and $1/\tau$ is the imaginary part of the frequency. The latter describes both the exponential rise of the r-mode driven by the Friedman-Schutz mechanism [26, 27] and its decay due to viscous damping. $1/\tau$ can be determined by the balance between the gravitational radiation (driving force) and the viscosities (damping force) as $1/\tau = -|1/\tau_{grav}| + 1/\tau_{damp}$, and theoretical calculations of transport properties give predictions on the instability of r-modes as well as its saturation amplitude. Fig. 1.5 shows how different models of cold dense matter modify the instability window of r-modes, where $1/\tau = 0$. Current observation of fast rotating neutron stars indicates that r-mode oscillations in these extremely stable systems must be either damped away completely, or saturated at such low amplitudes $O(10^{-8} - 10^{-7})$ that it has tiny effects on the spin evolution

of the stars, which suggests that exotic matter such as strange quark matter to be a good candidate explaining the data. One situation studied in this thesis is a hybrid star with a sharp interface between the quark matter core and the nuclear matter mantle, and detailed theoretical calculations and observational predictions will be given in Chap. 5.

1.3 Observations and Theory

One major area of activity in neutron star physics is the attempt to find observable signatures by which we could tell, from earth based observations of neutron stars, whether they have quark matter (probably strange matter) in their core.

1.3.1 Mass and radius

A measurement of a neutron star mass, even without a simultaneous measurement of its radius, constrains the EoS if it exceeds the maximum mass predicted by a given model. Current knowledge of hadronic physics suggests that at densities relevant to the core region of neutron stars (roughly $6 - 10n_0$, where n_0 is the nuclear saturation density) a softening of the EoS would occur, lowering the maximum mass unless the interaction of the new constituents provides the necessary repulsion to counter-balance the strong gravitational force.

The two most constraining systems are PSRs J1614-2230 [1] and J0348+0432 [23], with masses of 1.97 ± 0.04 and $2.01 \pm 0.03 M_\odot$ respectively. PSR J1614-2230 is a 3.1 ms millisecond pulsar orbiting an intermediate-mass white dwarf every 8.7 days. The system has a very high inclination resulting in a strong Shapiro delay signal. PSR J0348+0432 is a 39 ms pulsar in a

relativistic, 2.46 h orbit with a low-mass white dwarf. For this binary the masses have been measured through phase-resolved optical spectroscopy of the bright white dwarf companion.

While a $2M_{\odot}$ do not directly exclude any components in the neutron star interior they do put very stringent constraints on the respective interactions. In particular there have been various conjectures about the hyperon interaction [28, 29, 30, 31] but for most of the hyperonic models the maximum mass cannot reach $2M_{\odot}$. Possible solutions include a transition to quark matter [19, 32], or Bose-Einstein condensates of mesons (pions or kaons, the latter containing a strange quark) and Λ baryons (resonant states), however the densities at which such phases would appear, and the degree to which they might co-exist with other phases, are highly uncertain.

Measurements of neutron star radii and compactness have been achieved through observations and modeling of several different classes of sources. The number of independent observables, the uncertainties associated with each observable, and those in the theoretical models all play a role in determining the overall accuracy of the radii determinations.

For neutron stars that show thermonuclear bursts or are in quiescence, the measurements of the radii rely on the detection of thermal emission from their surfaces. The first constraints on high-density EoS from radius measurements are obtained from thermonuclear bursters that found that the relatively small observed radii point to lower pressures at and above $2n_0$ than those predicted by purely nucleonic EoS [33]. Similarly in the analysis of quiescent neutron stars small radii were found [34], which also point to softer equations of state than expected for nucleonic compositions. Recently Ref. [35] employes Bayesian statistical frameworks to obtain neutron star radii from the spectroscopic measurements as well as to infer the equation of state from the radius measurements, finding that around $1.5M_{\odot}$, the preferred equation of state predicts a radius of $10.8^{+0.5}_{-0.4}$km.

Although an accurate, simultaneous mass and radius measurement from even one neutron star would be ideal to provide a significant constraint on dense matter EoS, it is also striking that by expressing various models in a reasonably generic model-independent way we show that in Chaps. 3 and 4 observations of mass and radius of hybrid stars have already strongly constrained the dense matter parameter values, assuming a sharp transition from nuclear matter to a high-density phase such as quark matter, and that the speed of sound in that phase is independent of the pressure.

1.3.2 Spin rates

It has been shown that [36] a detailed analysis of pulsar evolution based on precise pulsar timing data can constrain the star's composition, through unstable global oscillations (r-modes) whose damping is determined by microscopic properties of the interior. If not efficiently damped, these modes emit gravitational waves that quickly spin down a millisecond pulsar. There are two scenarios to explain the observed timing data. It might be that the ordinary nuclear matter model of neutron stars is incomplete, and there is additional damping (e.g. from exotic forms of matter or currently overlooked physical processes) that stops r-modes from growing in these stars. In this case there will be no r-mode gravitational radiation from old neutron stars. The other possibility is the conventional scenario where only standard damping mechanisms are present in neutron stars. In this scenario most old millisecond pulsars will be undergoing r-mode oscillations, since for expected r-mode saturation amplitudes the dissipative heating ensures that fast spinning sources can neither cool nor spin out of the parameter region were r-modes are unstable.

Besides, glitches (the sudden spin-up in the rotational frequency of a neutron star) provide information on the dynamics of the internal superfluid and its interaction with the other neutron star constituents, and the size of the largest glitches has already constrained the amount and location of the participating superfluid [37, 38].

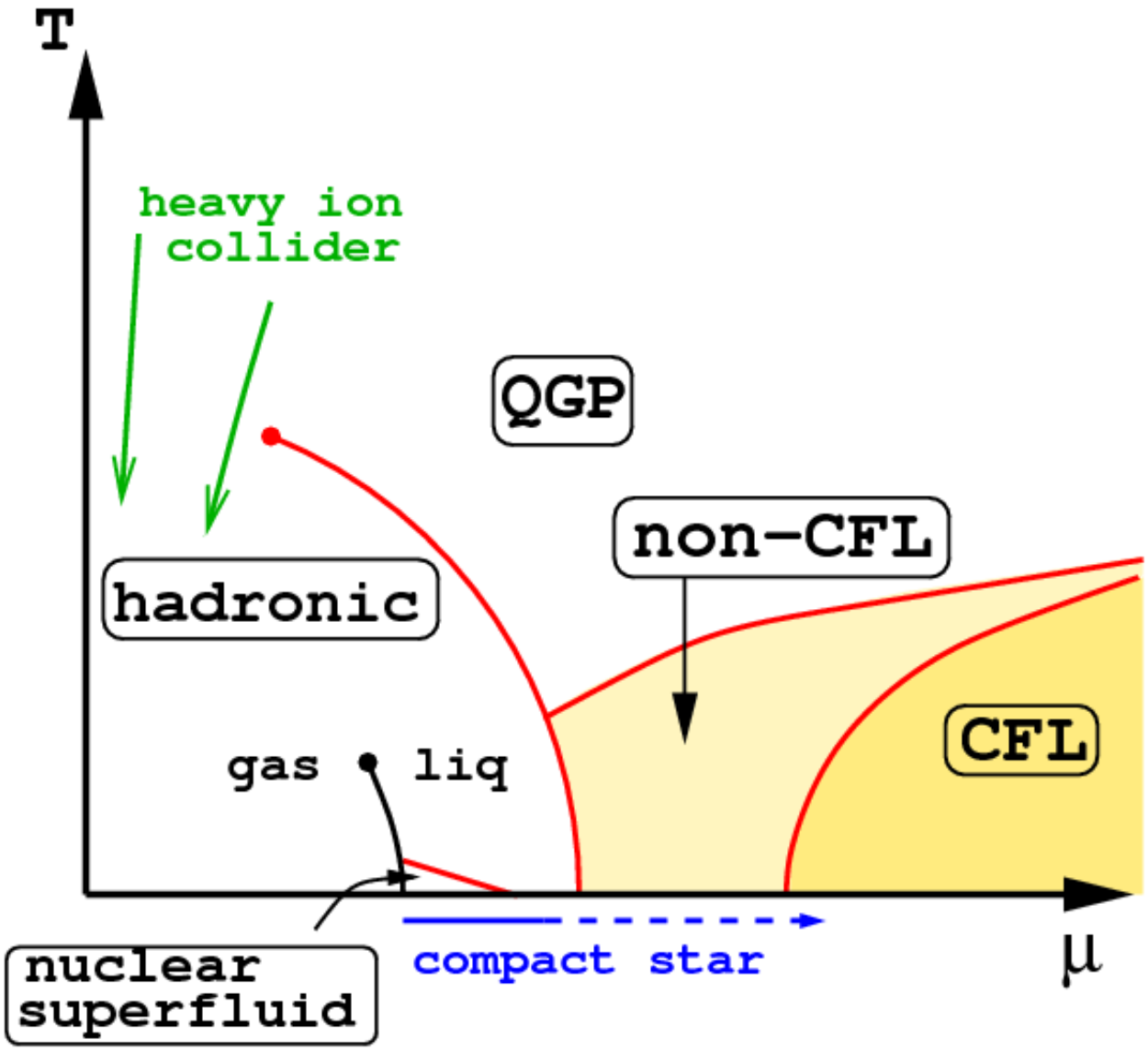

Figure 1.2: A schematic outline for the phase diagram of matter at ultrahigh density and temperature. The CFL phase is a superfluid (like cold nuclear matter) and has broken chiral symmetry (like the hadronic phase) [2].

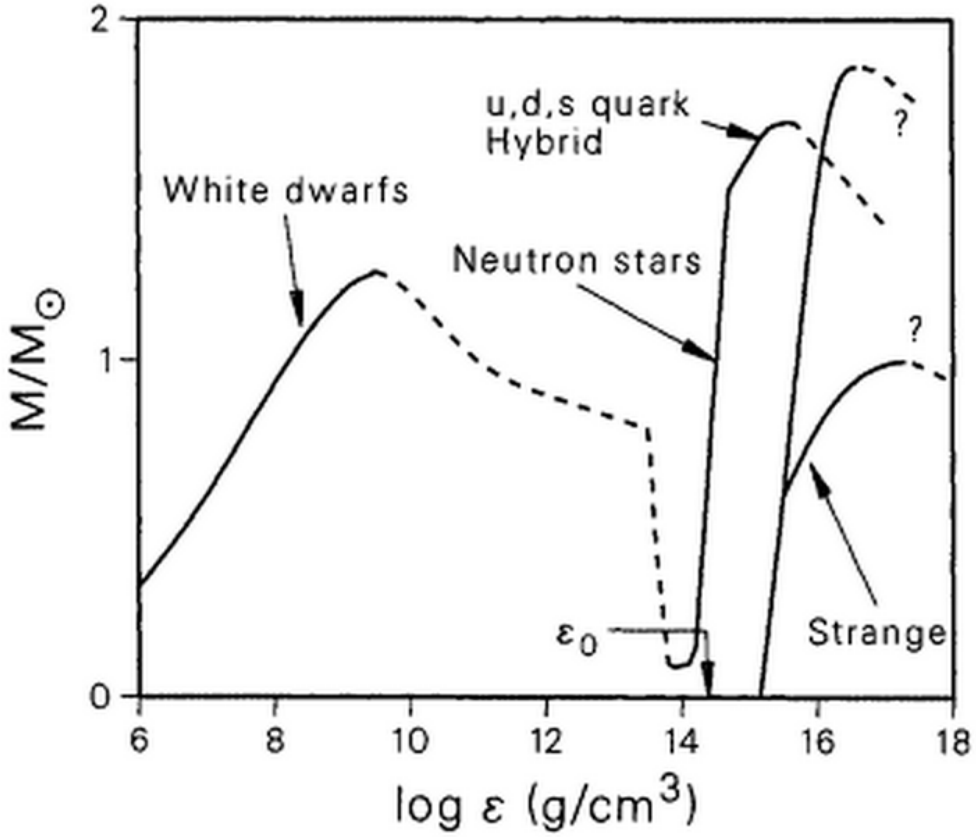

Figure 1.3: Schematic illustration of the solution to TOV equations over a broad range of central pressures; hypothetical strange stars are also shown [3].

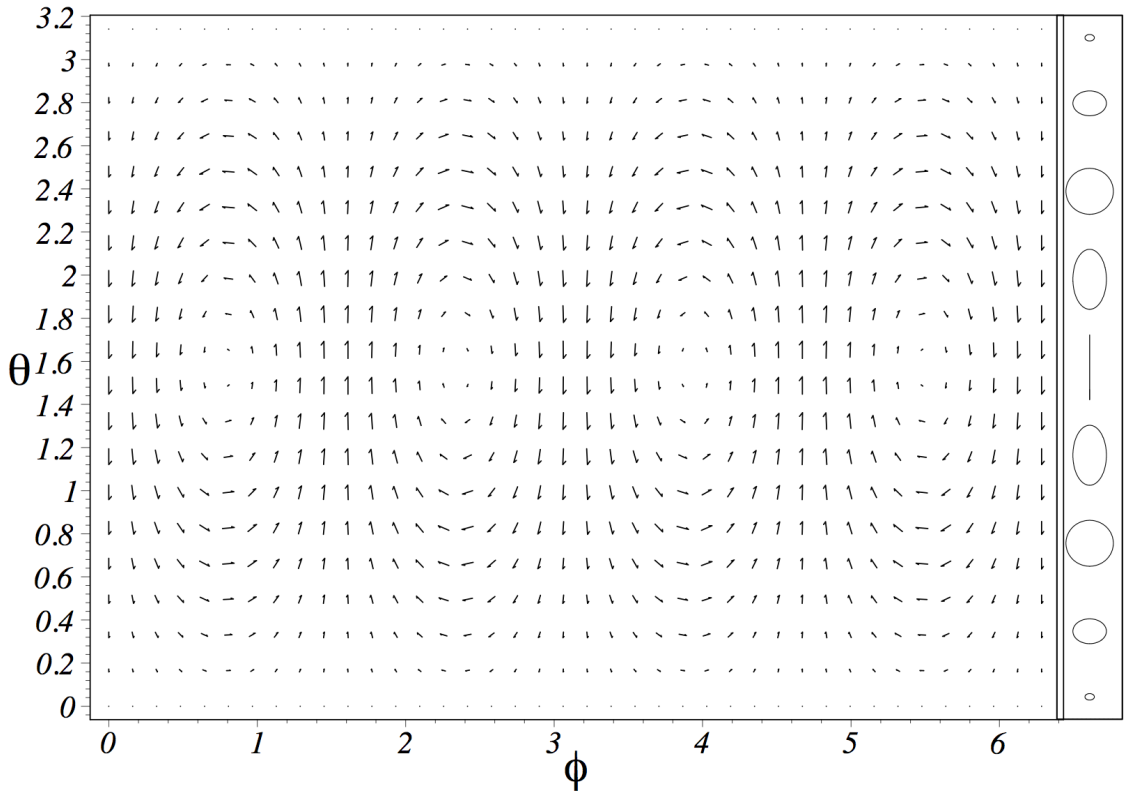

Figure 1.4: The large left frame shows the velocity field of the $l = m = 2$ r-mode at an instant in time. The narrow frame on the right is a qualitative picture of the actual motion of individual fluid elements (to leading order in the slow-rotation expansion). [4].

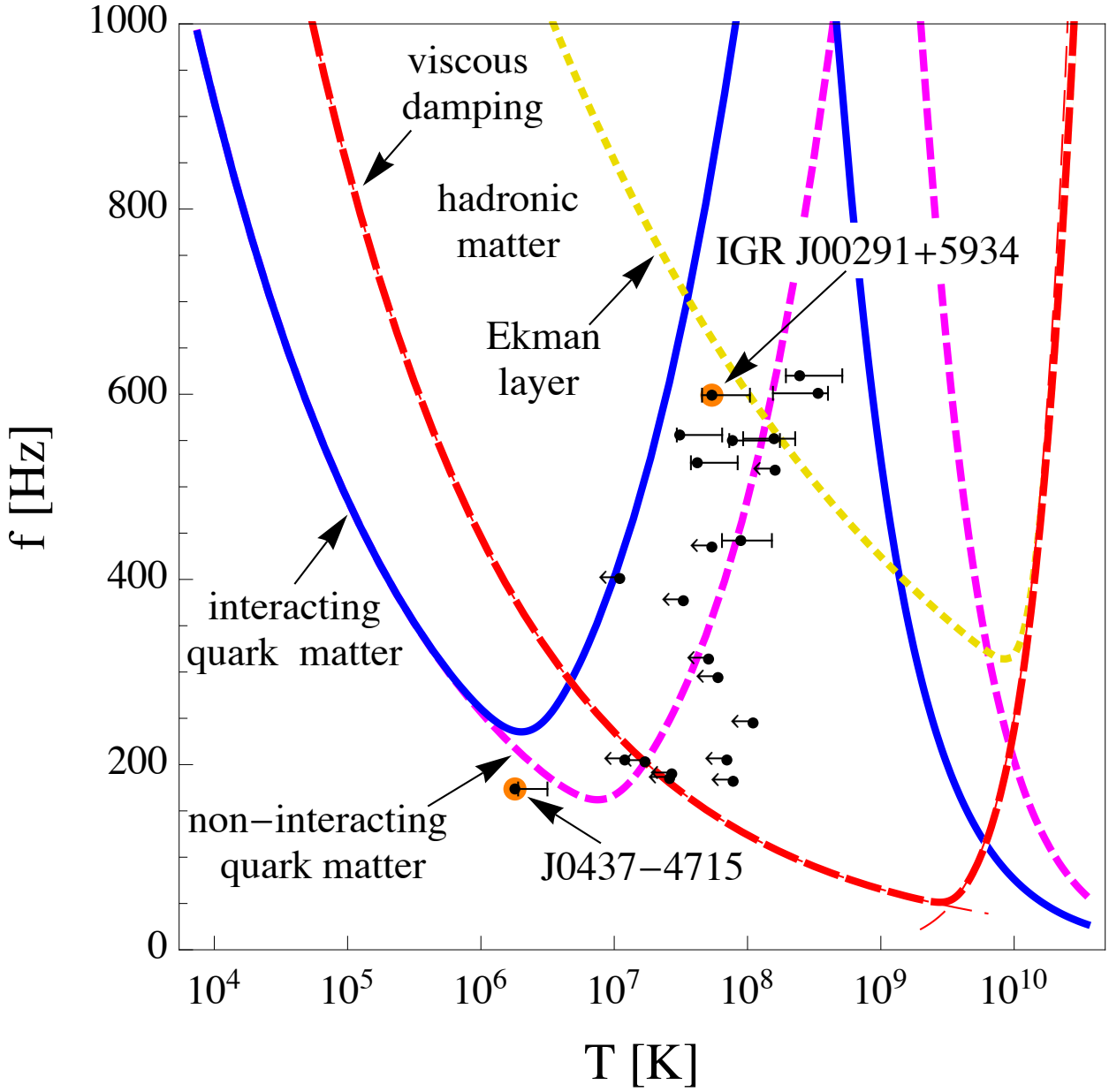

Figure 1.5: Predictions of the r-mode instability window from various dense matter models. Measurement of temperatures are given as upper-bounds.

Chapter 2

Strangelet dwarfs

It is generally assumed that strange stars are compact objects, with sizes in the 10 kilometer range [18], ending at a sharp surface of thickness $\sim$ 1 Fermi, perhaps with a very thin electrostatically suspended nuclear matter crust [39, 40, 41]. However, if the surface tension σ of the interface between quark matter and the vacuum is less than a critical value $\sigma_{\rm crit}$ (of order a few MeV/fm^2 in typical models of quark matter) then large strangelets are unstable against fission into smaller ones [42, 43, 44], and the energetically preferred state is a crystal of strangelets: a mixed phase consisting of nuggets of positively-charged strange matter in a neutralizing background of electrons. In this "low surface tension" scenario, the compact branch contains strange stars with a crust that consists of strangelets in a background of electrons; this "strangelet crystal crust" was studied in Ref. [44]. In this chapter we study the diffuse branch, which has no core of uniform quark matter: these stars consist entirely of strangelets in a background of degenerate electrons, so by analogy with white dwarfs we call them strangelet dwarfs.

2.1 Introduction

The strangelet-crystal phase is a charge-separated phase. Charge separation is favored by the internal energy of the phases involved, because a neutral phase is always at a maximum of the free energy with respect to the electrostatic potential (see [45, 46]; for a pedagogical discussion see [47]). The domain structure is determined by competition between surface tension (which favors large domains) and electric field energy (which favors small domains). Debye screening plays a role in determining the domain structure, because it redistributes the electric charge, concentrating it in the outer part of the quark matter domains and the inner part of the surrounding electron gas, and thereby modifying the internal energy and electrostatic energy contributions. In this chapter, we solve the Tolman Oppenheimer Volkoff equation [48, 25], using the equation of state of the mixed phase to obtain the $M(R)$ relation of strangelet dwarfs.

In Sec. 2.2 we introduce a phenomenological parametrization of uniform quark matter, and explore ranges of reasonable parameter values. In Sec. 2.3 we obtain the equation of state in the strangelet lattice, by assuming that the strangelet lattice can be divided into unit cells ("Wigner-Seitz cells") and calculating the pressure of a cell as a function of its energy density. Our approach is similar to that used in previous studies of the strangelet crystal [43, 44] (except that in this paper we include electron mass effects) and in studies of mixed phases of quark matter and nuclear matter in the interior of neutron stars [49]. In Sec. 2.4 we show the numerical results and analytical approximations of EoS and the consequential mass-radius relation of strangelet dwarfs. Finally in Sec. 2.5 we give the conclusion and future applications of this work.

The main assumptions that we make are:

1) We assume that the strangelets in the plasma form a regular lattice of Wigner-Seitz cells, which we treat as rotationally invariant (spherical). In reality the cells will be unit cells of some regular lattice. We do not consider lower-dimensional structures (rods or slabs) because in Ref. [44] we found that such structures were never energetically favored.

2) Within each Wigner-Seitz cell we use a Thomas-Fermi approach, solving the Poisson equation to obtain the charge distribution, energy density, and pressure. This is incorrect for very small strangelets, where the energy level structure of the quarks becomes important [50, 51].

3) We treat the interface between quark matter and the vacuum as a sharp interface which is characterized by a surface tension. We assume there is no charge localized on the surface. (Thus we neglect any surface charge that might arise from the reduction of the density of states of strange quarks at the surface [52, 53, 54, 55].)

4) We neglect the curvature energy of a quark matter surface [56, 57], so we do not allow for "Swiss-cheese" mixed phases, in which the outer part of the Wigner-Seitz cell is filled with quark matter, with a cavity in the center, for which the curvature energy is crucial.

5) We work at zero temperature.

In our calculations we use units $\hbar = c = \epsilon_0 = 1$, so $\alpha = e^2/(4\pi) \approx 1/137$.

2.2 Phenomenological Description of Quark Matter

We use the fact that in most phases of quark matter the chemical potential for negative electric charge μ_e is much less than the chemical potential for quark number μ. This allows us to write down a model-independent parameterization of the quark matter equation of

state, expanded in powers of μ_e/μ [43],

$$p_{\rm QM}(\mu,\mu_e) \approx p_0(\mu) - n_Q(\mu)\mu_e + \tfrac{1}{2}\chi_Q(\mu)\mu_e^2 + \ldots \tag{2.1}$$

Note that the contribution of electrons to the pressure of quark matter is $\mathcal{O}(\mu_e^4)$, and is neglected. This is a very good approximation for small strange quark mass, which corresponds to small n_Q. (For the largest value of n_Q that we study, μ_e in neutral quark matter is close to 100 MeV, and the assumption is still reasonable.) Also although Eq. (2.1) of the electrostatic properties of quark matter is generic, it is not appropriate for strangelets in the color-flavor locked (CFL) phase [58], which is a degenerate case requiring separate treatment (see Sec. 2.4.1).

As noted in Sec. 2.1, we assume that the interface between quark matter and vacuum has a surface tension σ, and we neglect any curvature energy.

The quark density n and the electric charge density $q_{\rm QM}$ (in units of the positron charge) are

$$n = \frac{\partial p_{\rm QM}}{\partial \mu}, \qquad q_{\rm QM} = -\frac{\partial p_{\rm QM}}{\partial \mu_e} = n_Q - \chi_Q \mu_e \ . \tag{2.2}$$

So in uniform neutral quark matter the electron chemical potential is $\mu_e^{\rm neutral} = n_Q/\chi_Q$. Eq. (2.1) is a generic parametrization if $\mu_e^{\rm neutral} \ll \mu$, which is typically the case in three-flavor quark matter.

The bag constant enters in $p_0(\mu)$, and we will fix it by requiring that the first-order transition between neutral quark matter and the vacuum occur at quark chemical potential $\mu_{\rm crit}$, i.e. $p(\mu_{\rm crit}, \mu_e^{\rm neutral}) = 0$. Because we are assuming that the strange matter hypothesis is valid, we require $\mu_{\rm crit} \lesssim 310$ MeV, since at $\mu \approx 310$ MeV there is a transition from vacuum

to neutral nuclear matter. In this article we will typically use $\mu_{\rm crit} = 300$ MeV. The value of μ inside our quark matter lumps will always be very close to $\mu_{\rm crit}$, so we can also expand in powers of $\mu - \mu_{\rm crit}$, and write

$$\begin{aligned} p_{\rm QM}(\mu, \mu_e) &\approx n\,(\mu - \mu_{\rm crit}) + \tfrac{1}{2}\chi\,(\mu - \mu_{\rm crit})^2 \\ &\quad + \tfrac{n_Q^2}{2\chi_Q} - n_Q \mu_e + \tfrac{1}{2}\chi_Q \mu_e^2 \ . \end{aligned} \tag{2.3}$$

A quark matter equation of state can then be expressed in terms of 6 numbers: $\mu_{\rm crit}$, the charge density n_Q and charge susceptibility χ_Q evaluated at $\mu = \mu_{\rm crit}$, the quark number density n and susceptibility χ evaluated at $\mu = \mu_{\rm crit}$, and the surface tension σ.

We will restrict ourselves to values of the surface tension that are below the critical value [43]

$$\sigma_{\rm crit} = 0.1325\,\frac{n_Q^2 \lambda_D}{\chi_Q} = 0.1325\,\frac{n_Q^2}{\sqrt{4\pi\alpha}\chi_Q^{3/2}}, \tag{2.4}$$

where λ_D is the Debye screening length in quark matter

$$\lambda_D = \frac{1}{\sqrt{4\pi\alpha\chi_Q}} \ . \tag{2.5}$$

If the surface tension is larger than $\sigma_{\rm crit}$ then the energetically favored structure at low pressure will not be a strangelet crystal, and there will be no strangelet dwarfs.

Rough estimates of surface tension from the bag model are in the range 4 to 10 MeV/fm^2 [59, 60], and for typical models of quark matter, $\sigma_{\rm crit}$ is of order 1 to 10 MeV/fm^2 [43], so it is reasonable to explore the possibility that strange quark matter could have a surface tension below $\sigma_{\rm crit}$.

2.2.1 Specific equations of state

When we show numerical results we will need to vary n_Q and χ_Q over a range of physically reasonable values. To give a rough idea of what values are appropriate, we consider the example of non-interacting three-flavor quark matter, for which n_Q and χ_Q become functions of μ and the strange quark mass m_s, while p_0 is in addition a function of the bag constant B. Expanding to lowest non-trivial order in m_s,

$$\begin{aligned} p_0(\mu) &= \frac{9\mu^4}{12\pi^2} - B \ , \\ n_Q(\mu, m_s) &= \frac{m_s^2 \mu}{2\pi^2} \ , \\ \chi_Q(\mu, m_s) &= \frac{2\mu^2}{\pi^2}. \end{aligned} \tag{2.6}$$

We emphasize that these expressions are simply meant to give a rough idea of reasonable physical values for n_Q and χ_Q. Our treatment does not depend on an expansion in powers of m_s. To tune the transition between neutral quark matter and the vacuum so it occurs at $\mu = \mu_{\rm crit}$ (see previous subsection), we set B so that $p_0(\mu_{\rm crit}) = \frac{1}{2} n_Q^2(\mu_{\rm crit})/\chi_Q(\mu_{\rm crit})$.

In the regions between lumps of strange matter, we will assume that there is a degenerate electron gas, whose pressure, and charge density in units of e, are

$$\begin{aligned} p_{e^-}(\mu_e) &= \frac{1}{24\pi^2}\Big((2k_{Fe}^2 - 3m^2) k_{Fe} \mu_e \\ &\quad + 3m^4 \ln\Big(\frac{k_{Fe} + \mu_e}{m}\Big)\Big) \ , \\ q_{e^-}(\mu_e) &= -\frac{1}{3\pi^2} k_{Fe}^3 \ . \end{aligned} \tag{2.7}$$

where $\mu_e^2 = k_{Fe}^2 + m_e^2$. Note that at low pressures this is more accurate than the electron gas equation of state used in Ref. [44], where the electron mass was set to zero.

2.3 Equation of State of Strangelet Crystal

2.3.1 Wigner-Seitz cell

Following the approach of [44], we analyze a spherical Wigner-Seitz cell of radius $R_{\rm cell}$, with a sphere of quark matter at the center of radius R. We use the Thomas-Fermi approximation to calculate $\mu_e(r)$,

$$\nabla^2 \mu_e(r) = -4\pi\alpha q(r) \ , \tag{2.8}$$

where $q(r)$ is the electric charge density in units of the positron charge e, and μ_e is the electrostatic potential divided by e.

The boundary conditions are that there is no electric field in the center of the cell (no δ-function charge there), and no electric field at the edge of the cell (the cell is electrically neutral),

$$\frac{d\mu_e}{dr}(0) = 0 \ , \qquad \frac{d\mu_e}{dr}(R_{\rm cell}) = 0 \ . \tag{2.9}$$

We also need a matching condition at the edge of the quark matter. Since we assume that no charge is localized on the surface, we require continuity of μ_e and its first derivative (the electric field) at $r = R$.

The value of μ inside the strange matter will be slightly different from $\mu_{\rm crit}$ because the surface tension compresses the droplet. To determine the value of μ, we require the pressure discontinuity across the surface of the strangelet to be balanced by the surface tension:

$$p_{\rm QM}(\mu, \mu_e(R)) - p_{e^-}(\mu_e(R)) = \frac{2\sigma}{R} \ . \tag{2.10}$$

Once these equations are solved, we can obtain the equation of state of matter made of such cells. The total energy of a cell is

$$\begin{aligned} E &= 4\pi \int_0^R r^2 dr \left(\mu n(\mu_e) - \tfrac{1}{2}\mu_e q_{\rm QM}(\mu_e) - p_{\rm QM}(\mu, \mu_e) \right) \\ &+ 4\pi \int_R^{R_{\rm cell}} r^2 dr \left(-\tfrac{1}{2}\mu_e q_{e^-}(\mu_e) - p_{e^-}(\mu_e) \right) \\ &+ 4\pi R^2 \, \sigma \ , \end{aligned} \tag{2.11}$$

The $-\frac{1}{2}\mu_e q$ terms in (2.11) come from combining $-\mu_e q$ (from the relationship between energy density and pressure) with the electric field energy density $+\frac{1}{2}\mu_e q$. The pressure of the cell is simply the pressure of the electrons at the edge of the cell,

$$p_{\rm cell} = p_{e^-}\left(\mu_e(R_{\rm cell})\right) \ . \tag{2.12}$$

The total number of quarks is

$$N = 4\pi \int_0^R r^2 dr \, n(\mu, \mu_e) \ . \tag{2.13}$$

The volume of the cell is $V = (4/3)\pi {R_{\rm cell}}^3$.

By varying R and $R_{\rm cell}$ we generate a two-parameter family of strangelets. However, there is really only a single-parameter family of physical configurations, parameterized by the external pressure $p_{\rm cell}$. On each line of constant $p_{\rm cell}$ in the $(R, R_{\rm cell})$ parameter space, we must minimize the enthalpy per quark,

$$h = \frac{E + p_{\rm cell} V}{N} \ , \tag{2.14}$$

to find the favored value of R and $R_{\rm cell}$. We assume zero temperature so h is also the Gibbs free energy per quark.

We now have a well-defined way to obtain the equation of state of the mixed phase of quark matter, namely the energy density $\varepsilon = E/V$ as a function of the pressure $p_{\rm cell}$.

2.3.2 Numerical solution

Inside the quark matter, the solution to the Poisson equation (2.8) that obeys the boundary condition at the origin is

$$\mu_e(r) = \frac{n_Q}{\chi_Q} + \frac{A}{r\lambda_D}\sinh(\frac{r}{\lambda_D}) \ , \tag{2.15}$$

where A will be determined by matching conditions.

In the degenerate electron gas region outside the strange matter, from (2.7) and (2.8) the Poisson equation becomes

$$\nabla^2\mu_e(r) = \frac{4\alpha}{3\pi}(\mu_e^2 - m_e^2)^{3/2} \ , \tag{2.16}$$

which must be solved numerically. For a given value of A we find from (2.15) the value and slope of $\mu_e(r)$ at $r = R$, and use these as initial values to propagate $\mu_e(r)$ out to $r = R_{\rm cell}$ using (2.16). We vary A until we obtain a solution that obeys the boundary condition of no electric field at the edge of the cell.

2.3.3 Low-pressure approximations

If the pressure is not too high, the strangelet crystal consists of large Wigner-Seitz cells ($R_{\rm cell} \gg R$). In this regime one can obtain approximate analytic expressions for the

equation of state of the crystal by assuming that the electrons have a roughly constant density outside the strangelet. We give these expressions below, and in later sections we use them to calculate mass radius relations for large strangelet dwarf stars. However, we expect these approximations break down at ultra-low pressures, when the cell size becomes so large that screening cannot be ignored, and the electrons are clumped around the strangelets, forming atoms, rather then being roughly uniformly distributed between the strangelets. This will happen when $R_{\rm cell}$ approaches the Bohr radius $a_0 = 1/(\alpha m_e)$, i.e. when $p_{\rm cell} \lesssim \alpha^5 Z^{5/3} m_e^4 \approx (10^{-12}{\rm MeV}^4) Z^{5/3}$. At these ultra-low pressures one should use an atomic matter equation of state: we do not do this, since we expect it will only affect a very small surface layer of the star, without any appreciable effect on the mass-radius relationship.

The equation of state $\varepsilon(p_{\rm cell})$ is found by writing the energy density ε of the cell and its pressure as a function of the size of the cell. For now we will treat the size R and charge Z of the central strangelet as unknowns; later we will estimate their values.

Since the pressure inside a large cell is very low the energy density of the quark matter is approximately $n\mu_{\rm crit}$, so

$$\varepsilon \approx n\mu_{\rm crit} \frac{R^3}{{R_{\rm cell}}^3} \ . \tag{2.17}$$

To obtain the pressure at the edge of the cell we need to estimate the density distribution of the electrons outside the strangelet.

Constant potential approximation The simplest approximation is to ignore screening, taking the electron Fermi momentum k_{Fe} to be independent of r outside the strangelet (Sec. I

of Ref. [61]). Imposing neutrality of the cell fixes the Fermi momentum of the electrons,

$$k_{Fe}^3 = \frac{9\pi Z}{4{R_{\rm cell}}^3} \ . \tag{2.18}$$

Using (2.17), we obtain the equation of state $\varepsilon(p_{\rm cell})$ of the strangelet crystal

$$\varepsilon \approx \mu_{\rm crit} n \frac{4(k_{Fe}R)^3}{9\pi Z} \tag{2.19}$$

where we use (2.7) to relate the electron Fermi momentum to $p_{\rm cell}$.

Because the constant potential approximation gives a fairly simple expression we can use it to understand how the strangelet crystal EoS depends on the parameters of the quark matter EoS, and hence how the $M(R)$ curve for strangelet dwarf stars depends on those parameters. Note that in (2.19) the dependence of the energy density on the pressure is via a universal and monotonically increasing function $k_{Fe}(p)$; dependence on the quark matter parameters enters via the factor that multiplies this function. To make the dependence on quark matter parameters explicit we use results for R and Z from Sec. 2.3.3 below, and rewrite (2.19) for the EoS of the strangelet crystal as

$$\begin{aligned} \varepsilon(p_{\rm cell}) &\sim S\left(k_{Fe}(p_{\rm cell})\right)^3 \ , \\ S &= \frac{\mu_{\rm crit} n}{3\pi^2 n_Q \xi(x_0(\bar{\sigma}))} \ , \end{aligned} \tag{2.20}$$

where all dependence on the quark matter parameters comes through the prefactor S, which has units of energy. S can be explicitly obtained using (2.25), (2.27), and (2.28) for the ξ function. One could informally think of S as a "softness" parameter of the strangelet crystal EoS: as S increases, the pressure becomes a more slowly-rising function of energy density. We expect that softer equations of state will yield smaller stars with lower maximum masses.

In Table 2.1 we give the value of S for a range of values of the parameters of the underlying quark matter EoS.

At low enough pressures, the electrons become nonrelativistic. Then $p_{\rm cell} \approx k_{Fe}^5/(15\pi^2 m_e)$, and (2.19) simplifies to an analytic expression for the equation of state,

$$\varepsilon_{NR} \approx \frac{4R^3}{3Z}\Big(\frac{125\pi}{9}m_e^3\Big)^{1/5} n\mu_{\rm crit} p_{\rm cell}^{3/5} \tag{2.21}$$

This is a reasonable approximation when $k_{Fe} \lesssim m_e$, i.e. when $p_{\rm cell} \lesssim m_e^4/(24\pi^2) \approx 0.0003\,{\rm MeV}^4$. However, as we will see below, at the very lowest pressures the constant potential approximation becomes inaccurate.

Coulomb potential approximation We can improve on the constant potential approximation by including the Coulomb energy of the electrons in the calculation of the pressure. The equation of state is still given by (2.19), but now the relationship between $p_{\rm cell}$ and k_{Fe} is modified by the addition of a Coulomb energy term (Ref. [61], (5)), yielding

$$p_{\rm cell} = p_{e^-} - \frac{\alpha}{5}\Big(\frac{Z^2}{18\pi^7}\Big)^{1/3} k_{Fe}^4 \ . \tag{2.22}$$

Unlike the constant potential approximation, the Coulomb potential approximation gives an energy density that goes to a non-zero value at zero pressure,

$$\varepsilon_{\rm Coul}(0) = \mu_{\rm crit}\, n \frac{2Z(\alpha m_e R)^3}{3\pi^2} \ . \tag{2.23}$$

Comparing with (2.17) we see that this corresponds to the energy of cells with size of order $1/(\alpha m_e) \sim 10^{-10}\,{\rm m}$. This is the energy density of a lattice of zero-pressure atomic matter

with strangelets in place of nuclei, which is a reasonable guess for the low-pressure configuration of strangelets. We will therefore use the Coulomb approximation as the low-pressure extension of our equation of state. As we will see, this leads to a "planet" branch in the mass-radius relation for configurations of strange matter.

Radius and charge of strangelet at low pressure The low-pressure approximation expressions given above depend on the size R and charge Z of the strangelet at the center of a large cell. This is approximately an isolated strangelet, whose radius can be calculated by minimizing the isolated strangelet free energy given in eqn (25) of Ref. [43],

$$\overline{\Delta g}(x) = -\frac{3}{2}\frac{x - \tanh x}{x^3} + \frac{3\bar{\sigma}}{x} \ , \tag{2.24}$$

where x is the radius of the strangelet in units of λ_D, and

$$\bar{\sigma} = \frac{\sigma}{4\pi\alpha n_Q^2 \lambda_D^3} \ . \tag{2.25}$$

So the strangelet radius R as a function of the parameters of the quark matter equation of state is

$$R = x_0 \lambda_D, \quad \text{where} \quad \frac{d\overline{\Delta g}}{dx}(x_0) = 0 \ . \tag{2.26}$$

We are interested in values of $\bar{\sigma}$ up to 0.13, since for higher surface tension the strangelet crystal is no longer stable [43]. An approximate expression for the solution to (2.26), accurate to about 0.2% for $\bar{\sigma} \lesssim 0.13$, is

$$x_0^{\text{approx}} = \left(\frac{15\bar{\sigma}}{2}\right)^{1/3} + \frac{2.174\,\bar{\sigma}}{1 - 3.982\,\bar{\sigma}} \ , \tag{2.27}$$

where the first term is the leading-order analytic expression for x_0 in the limit of small $\bar{\sigma}$.

The charge Z of the central strangelet is given by eqn. (17) of Ref. [43], which can be written

$$\begin{aligned} Z &\approx \frac{4}{3}\pi R^3 n_Q \, \xi(R/\lambda_D) \ , \\ \xi(x) &\equiv \frac{3}{x^3}(x - \tanh x) \ , \end{aligned} \tag{2.28}$$

where ξ is a correction for the effects of screening inside the quark matter; it is an even function with $\xi(0) = 1$.

2.4 Numerical Results

2.4.1 Range of parameters studied

Our assumption that the strange matter hypothesis is valid requires that $\mu_{\rm crit}$ must be less than the quark chemical potential of nuclear matter, about 310 MeV, so we fix $\mu_{\rm crit} =$ 300 MeV. The value of μ inside our strange matter lumps will always be within a few MeV of $\mu_{\rm crit}$, because if the surface tension is small enough to favor the strangelet crystal it will not cause significant compression.

We will perform calculations for $\lambda_D = 4.82$ fm and $\lambda_D = 6.82$ fm, corresponding to $\chi_Q \approx 0.2\mu_{\rm crit}^2$ (appropriate for unpaired quark matter (2.6)) and $\chi_Q \approx 0.1\mu_{\rm crit}^2$ (appropriate for 2SC quark matter [43]).

Typical values of n_Q will be around $0.05\mu_{\rm crit}m_s^2$ (2.6), and a reasonable range would correspond to varying m_s over its physically plausible range, from about 100 to 300 MeV. (To have strange matter in the star, m_s must be less than $\mu_{\rm crit}$.) Here we use $n_Q = 0.0445$, 0.0791, and 0.124 fm^{-3}, which would correspond to $m_s = 150$, 200, and 250 MeV in (2.6).

There is another widely-discussed phase of quark matter, the color-flavor locked (CFL) phase, but it is a degenerate case where $n_Q = \chi_Q = 0$. CFL strangelets have a surface charge, but it does not arise from the mechanism studied here, Debye screening, and has a different dependence on the size of the strangelet [53]. We hope to study CFL strangelet matter in a separate work.

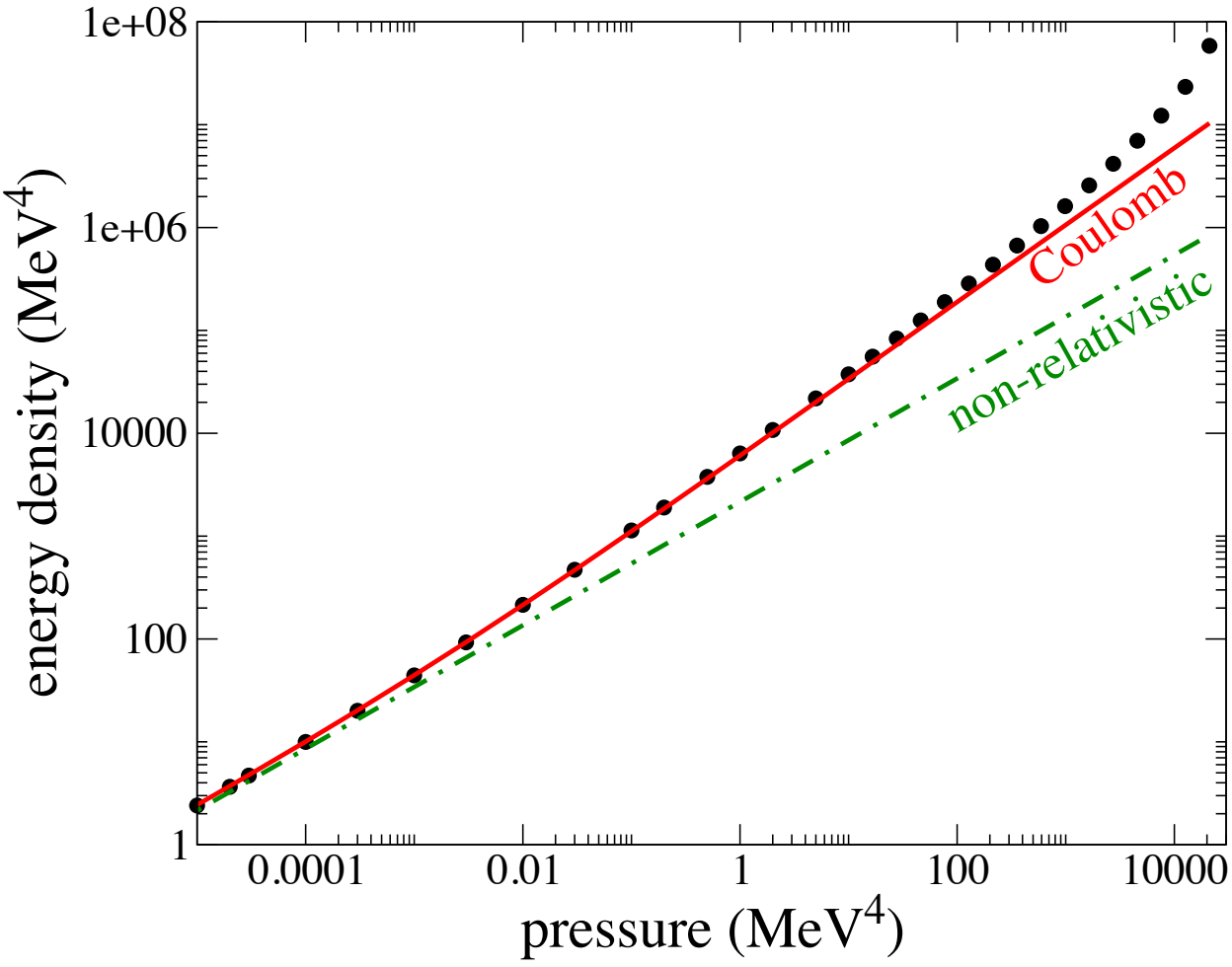

Figure 2.1: Equation of state of the mixed phase (strangelet crystal) for strange matter with $\mu_{\rm crit} = 300\,{\rm MeV}$, $\lambda_D = 6.82\,{\rm fm}$, $n_Q = 0.0791\,{\rm fm}^{-3}$, $\sigma = 1.0\,{\rm MeV fm}^{-2}$. The dots were obtained numerically following the procedure of Sec. 2.3.2. The solid line is the Coulomb-potential approximation (Sec. 2.3.3). The dashed line is the non-relativistic electron (ultra-low pressure) limit (2.21). Above $p \approx 20000\,{\rm MeV}^4$, uniform quark matter becomes favored over the mixed phase.

λ_D (fm)	n_Q (fm^{-3})	$\sigma_{\rm crit}$ (MeV fm^{-2})	Softness prefactor S (MeV) at $\sigma=0.3$	$\sigma=1.0$	$\sigma=3.0$	$\sigma=10.0$
4.82	0.0445	0.533	345	–	–	–
4.82	0.0791	1.69	158	202	–	–
4.82	0.124	4.12	94	104	140	–
6.82	0.0445	1.51	280	367	–	–
6.82	0.0791	4.8	146	161	206	–
6.82	0.124	11.6	90	95	105	155

Table 2.1: Softness prefactor (2.20) of the strangelet crystal for various quark matter equation of state. The first two columns, λ_D and n_Q, specify the quark matter equation of state (2.3) (via (2.5)). The third column gives the maximum surface tension for which a strangelet crystal will occur (2.4). The last four columns give the softness prefactor S for different values of the surface tension σ (given in MeV fm^{-2}) of the interface between quark matter and vacuum.

2.4.2 Testing approximations to the equation of state

In Fig. 2.1 we show the equation of state for the strangelet crystal, for critical quark chemical potential $\mu_{\rm crit} = 300\,\text{MeV}$, quark matter screening distance $\lambda_D = 6.82\,\text{fm}$, quark charge density parameter $n_Q = 0.0791\,\text{fm}^{-3}$, and quark matter surface tension $\sigma = 1.0\,\text{MeVfm}^{-2}$. The dots were obtained numerically following the procedure of Sec. 2.3.2. The solid line is the Coulomb-potential approximation (Sec. 2.3.3). On this plot the constant potential approximation (Sec. 2.3.3) line would be indistinguishable from the Coulomb-potential line, so we do not show it. The dot-dashed line is the non-relativistic electron (ultra-low pressure) limit (2.21) of the constant potential approximation. Above $p \approx 20000\,\text{MeV}^4$, uniform quark matter becomes favored over the mixed phase. On this very expanded logarithmic scale, the Coulomb approximation appears reasonably accurate up to pressures of order 1 MeV.

To achieve more discrimination between the different approximations, we show in Fig. 2.2 a magnified version of the low-pressure end of the plot in Fig. 2.1, where we have divided out the non-relativistic scaling of the energy density, $\varepsilon \sim p^{3/5}$. We can see that, down to

the lowest pressures for which we can perform the numerical Wigner-Seitz calculation of the equation of state, the Coulomb approximation gives the most accurate semi-analytic approximation, although the constant potential approximation is accurate to within about 10%.

We then have to decide which approximation to use for lower pressures, where numerical calculations are not available. In the low-pressure limit, the Coulomb approximation to $\varepsilon(p)$ tends to a fixed value, while the constant and nonrelativistic approximations to $\varepsilon(p)$ tend to zero as $p^{3/5}$. So in Fig. 2.2 the Coulomb approximation will diverge at $p \ll 10^{-5}\,\mathrm{MeV}^4$, while the constant and nonrelativistic approximations will tend to the same constant value. As discussed in Sec. 2.3.3, it seems reasonable to expect that at the lowest pressures there will be a crystal of "strange atoms", each consisting of electrons bound to a strangelet, and the Coulomb approximation gives a reasonable estimate of the energy density of such matter, so at low pressure we will use the Coulomb approximation.

2.4.3 Mass-radius relation of strange stars

In Fig. 2.3 we show the full mass-radius curve for stars made of quark matter with the equation of state plotted in Fig. 2.1. The compact branch contains strange stars with a strangelet crystal crust. The diffuse branch contains stars consisting entirely of strangelet crystal matter. It includes two segments: the lighter one is planets of dilute strange matter whose the mass increases with radius. This joins to the strangelet dwarf branch where the mass decreases with radius as the strangelet crystal is compressed by the pressure due to gravity. We use the numerically calculated equation of state (Sec. 2.3) except that at very low pressure (the planetary branch) the Wigner-Seitz cells become so large that our numerical

methods break down, so as discussed in Sec. 2.3.3 we use the Coulomb approximation (2.22) to extrapolate down to zero pressure.

Fig. 2.3 shows the whole $M(R)$ curve, not all of which corresponds to stable configurations. The usual stability criterion for stars [62] is that one radial mode becomes either stable or unstable at each extremum in the $M(R)$ function. A stable mode becomes unstable at each extremum where the curve bends counterclockwise as the central density increases; a stable mode becomes unstable at each extremum where the curve bends clockwise as the central density increases. However, Glendenning et.al. [63] report that at some extrema there is no change in stability: the squared frequency of one of the fundamental radial modes may touch zero, but not change sign. We defer a detailed study of the stability of radial modes of strange stars to future work, and in Fig. 2.3 we show as "stable" (solid curves) the parts of the $M(R)$ curve that both Ref. [62] and Ref. [63] agree are stable. We note that Ref. [63] is a study of stars that have a core of uniform strange matter surrounded by a crust of nuclear matter: these are similar to the configurations along the dashed part of the mass-radius curve in Fig. 2.3, where we have a core of uniform strange matter surrounded by a crust of strangelets, with a density discontinuity at the boundary. If Ref. [63]'s stability argument is correct and applicable to our stars, then some of these configurations may also be stable. In the remainder of this chapter we will focus on the strangelet dwarf branch, which consists of a simple crystal of stranglets with no uniform core, so there is no controversy about the appropriate stability criterion.

2.4.4 Mass-radius relation of strangelet dwarfs

To investigate the sensitivity of the masses and radii of strangelet dwarfs to the parameters of the quark matter equation of state, we show in Fig. 2.4 and 2.5 the strangelet dwarf part of the mass-radius curve, excluding the compact and planetary branches, for various values of the quark matter parameters.

In Fig. 2.4 we explore the effects of varying the surface tension, and we compare the different approximations to the equation of state. The upper curves are for the same equation of state as was shown in Fig. 2.1 and 2.2; the lower curves use a larger surface tension, $\sigma = 3\,\mathrm{MeVfm}^{-2}$. In both cases the solid curves are obtained from the Coulomb-potential approximation to the equation of state, and the dashed lines are obtained from the constant-potential approximation. The dots use the equation of state that is obtained numerically following the procedure of Sec. 2.3.2, except that at very low pressures, where the numerical calculation becomes too difficult, the Coulomb approximation is used.

We see that, as one might have expected from Fig. 2.1, using the Coulomb approximation over the entire pressure range of the mixed phase yields reasonably accurate results. However, as noted in Sec. 2.3.3, the constant potential approximation is still useful for gaining an understanding of how the $M(R)$ curve for strangelet dwarfs depends on the parameters of the EoS, because in the range of pressures that is important for strangelet dwarfs it gives a good indication of the $M(R)$ curve. (At ultra-low pressures, relevant for the strange planet branch, this is no longer the case: one has to use the Coulomb approximation instead.) As discussed in Sec. 2.3.3, the constant potential approximation to the EoS can be written in terms of a "softness prefactor" S (2.20). To understand how the $M(R)$ curve in Fig. 2.4 changes with σ, note that $x_0(\bar{\sigma})$ is a monotonically increasing function and $\xi(x_0)$ is a monotonically decreasing

function, so as the surface tension σ increases at fixed values of the other parameters, the softness prefactor S of the strangelet crystal EoS increases (one can see this in Table 2.1). Since the EoS is becoming softer, the $M(R)$ curve moves down and to the left, giving smaller stars with a lower maximum mass.

In Fig. 2.5 we explore the effects of varying the charge density parameter n_Q in (2.3) while keeping the other parameters constant. As in Fig. 2.4, solid lines are for the Coulomb approximation to the equation of state, dots are for the numerically calculated equation of state using the Coulomb approximation to extrapolate to the lowest pressures. We see that increasing n_Q yields heavier, larger strangelet dwarf stars. Again, this can be understood in terms of the constant potential approximation and its softness prefactor S (2.20). As n_Q increases, it causes S to decrease through two effects. Firstly via the explicit factor of n_Q in the denominator of (2.20), and secondly via the relationship (2.25) between σ and $\bar{\sigma}$. The sensitivity of S to changes in n_Q can be seen in Table 2.1: for the two values of n_Q used in Fig. 2.5 the values of S are near the extremes of its range in the parameter set we studied: $S \approx 345$ and $S \approx 94$ for $n_Q = 0.0445$ and $n_Q = 0.124$ respectively. Consequently, the $M(R)$ curve for $n_Q = 0.0445$ is characteristic of a soft equation of state, with low radius at a given mass and a low maximum mass, whereas the $M(R)$ curve for $n_Q = 0.124$ is characteristic of a hard equation of state, with large radius at a given mass and a high maximum mass.

2.5 Conclusions

In this chapter we have shown that, if the strange matter hypothesis is correct and the surface tension of the interface between strange matter and the vacuum is less than a critical value (2.4), there is at least one additional stable branch in the mass-radius relation for strange

stars, corresponding to large diffuse objects that we call "strangelet dwarfs", consisting of a crystal of strangelets in a sea of electrons. This is easily understood, since if $\sigma < \sigma_{\rm crit}$ then uniform strange matter is unstable at zero pressure, and undergoes charge separation to a crystal of positively-charged strangelets surrounded by electrons, just as normal matter at zero pressure is a mixed phase consisting of droplets of nuclear matter surrounded by electrons. Strangelet dwarfs are then the strange matter equivalent of white dwarfs.

We emphasize that in this low-surface-tension scenario, strange matter is *not* self bound. Like nuclear matter, it is only bound by gravitational forces. Every strange star will have a strangelet crystal crust, and strangelet dwarfs are those strange stars that are "all crust".

The natural production mechanism by which strangelet dwarfs might be produced is a collision between a strange star and another compact object. In such collisions, up to $0.03\,M_\odot$ may be ejected [64], which is in the mass range we are predicting for strangelet dwarfs. There are two ways a collision could produce strangelet dwarfs. Firstly, part of the crust of the strange star might be ejected to become a isolated object, which would be a strangelet dwarf. Secondly, if a sufficiently light piece of the uniform quark matter core were ejected in the collision, it would be unable to exist on the compact branch, and would evaporate into a configuration on the diffuse branch. For example, for the equation of state studied in Fig. 2.3, the lightest compact configuration of strange matter is $0.0055\,M_\odot$. A lighter piece of strange matter could only exist on the diffuse branch, and would spontaneously evaporate to become a strangelet dwarf. Strangelet dwarfs produced by these mechanisms could then bind gravitationally, to form heavier strangelet dwarfs.

It should be noted that our proposed mechanism for the production of strangelet dwarfs is also a mechanism for creating a diffuse cosmic flux of strangelets ("strangelet pollution"),

which might be expected to convert all neutron stars to strange stars [65]. Although observations of glitches and magnetar oscillations [66] seem consistent with some compact stars having nuclear matter crusts, there remains some uncertainty. Crystalline phases of quark matter could allow strange stars to glitch [67], and in our low-surface-tension scenario strange stars have crusts that could be hundreds of meters thick [44]. A cosmic flux of strangelets may seem unlikely but until it is ruled out experimentally (as may happen soon from the AMS experiment [68]) it remains useful to analyze the full observational consequences of the strange matter hypothesis.

Our analysis assumes that at any given pressure the strangelet crystal consists of the most energetically favorable strangelet configuration (in terms of strangelet size and charge and cell size). However, other configurations will in general be metastable with long lifetimes. If one compresses a piece of strangelet crystal then the charge of the strangelets can readily change via absorption or emission of electrons, but it is very difficult for the quark matter to rearrange itself in to strangelets of the now-energetically-favored size: it is more likely that the strangelets will stay the same size and the radial density profile of the electrons will change. The sizes of the strangelets will be determined more by the history of the object than by the pressure. Taking this point further, it is quite possible to have a crystal consisting of a mixture of strangelets and ordinary nuclei, held apart by their electrostatic repulsion but also bound together in to a crystal by the degenerate electron gas that neutralizes them, forming a hybrid strangelet/white dwarf star.

Detection of strangelet dwarfs requires an observation method that can find non-luminous objects with typical masses of 10^{-5} to $10^{-1}\,M_{\odot}$ and radii in the range 500 to 5000 km. An example is gravitational microlensing surveys, such as those conducted by the Microlensing Observations in Astrophysics (MOA) and the Optical Gravitational Lensing Experiments

(OGLE) groups, which look for lensing events in the galactic bulge, and are capable of detecting Jupiter-mass objects. It is intriguing that such surveys now report the existence of an abundant population of unbound distant planetary masses, suggesting that such objects may be twice as common as main sequence stars [22]. Although models of planet formation indicate that mechanisms exist for unbinding planets through disk instabilities and planet interactions [69], we suggest that a possible alternative is formation of strange dwarfs from matter ejected in strange star mergers. One would expect that sometimes a strangelet dwarf produced in a merger might be unable to escape the gravitational field of the remaining compact object, and this would explain the presence of dense planet-mass objects in the vicinity of compact stars. An example is the millisecond pulsar PSR J1719-1438, which has a Jupiter-mass companion whose inferred central density ($\rho > 23\,\mathrm{g\,cm^{-3}}$) is far in excess of what is expected in a planet [70]. We expect that in the near future further light will be cast on this question, as microlensing surveys help us better understand the distribution of planetary mass compact objects and as strategies are devised to provide information about both mass and radius.

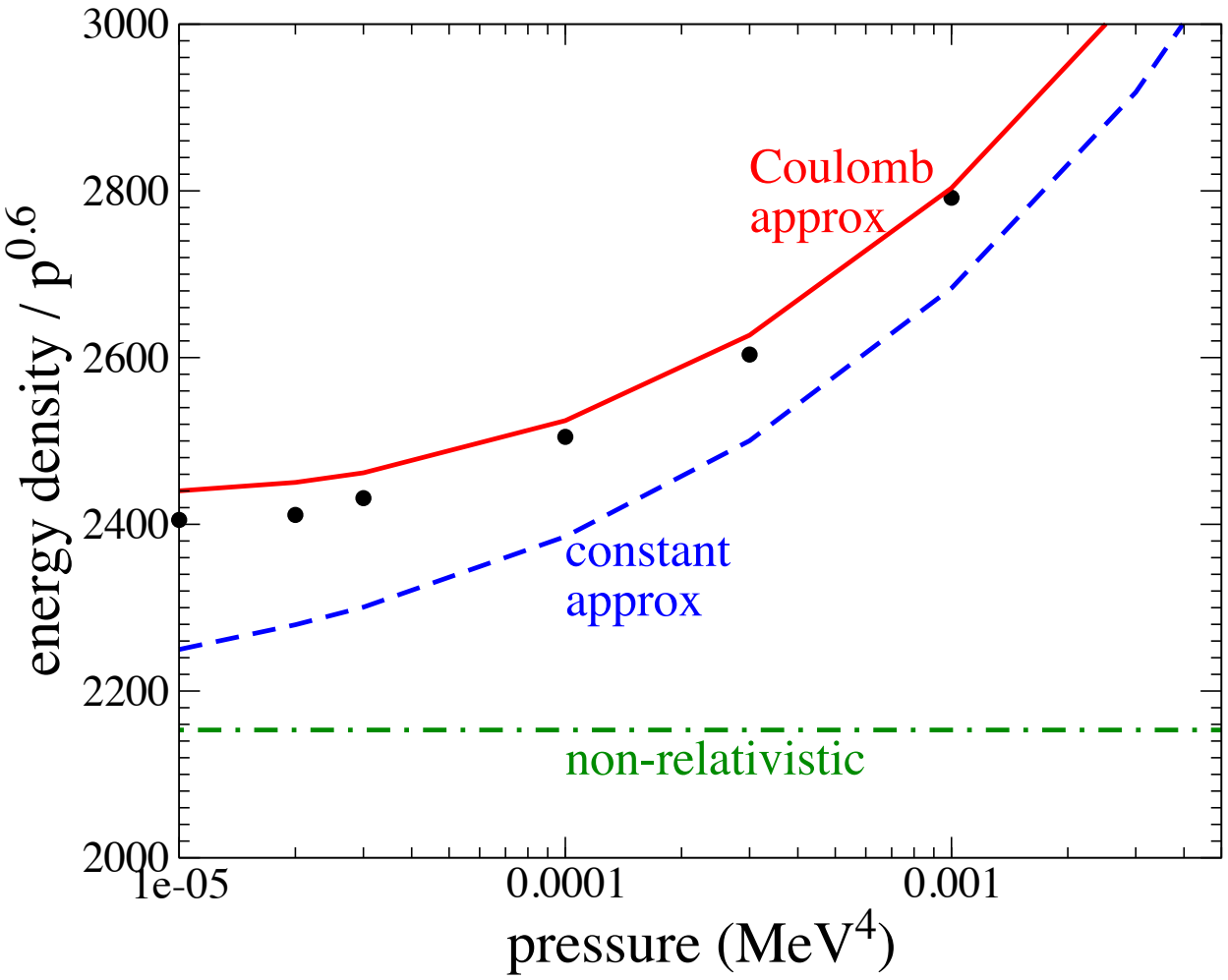

Figure 2.2: Equation of state of the mixed phase for the same parameters as in Fig. 2.1, zoomed in on the low pressure region, and with the energy density divided by $p^{0.6}$. The dots were obtained numerically following the procedure of Sec. 2.3.2. The Coulomb-potential approximation (Sec. 2.3.3) is the most accurate, followed by the constant-potential approximation (Sec. 2.3.3), and then the non-relativistic electron approximation (2.21).

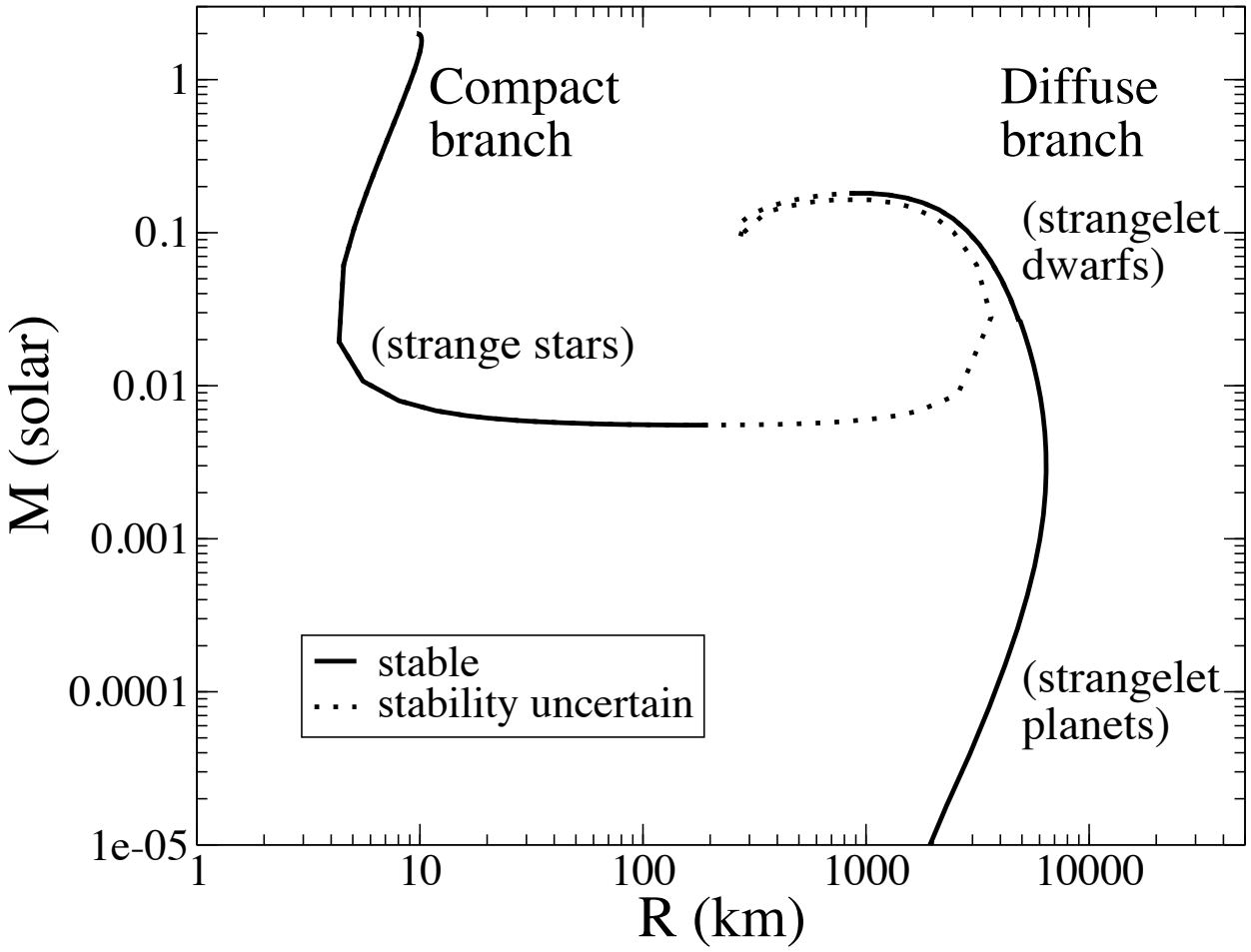

Figure 2.3: The full mass-radius curve for stars made of quark matter with the equation of state plotted in Fig. 2.1, using the Coulomb approximation (2.22) to extrapolate to lower pressures. The compact branch contains strange stars with a strangelet crystal crust. The diffuse branch contains stars consisting entirely of strangelet crystal matter. Solid lines represent configurations that are stable; stability of the other branches is discussed in the text.

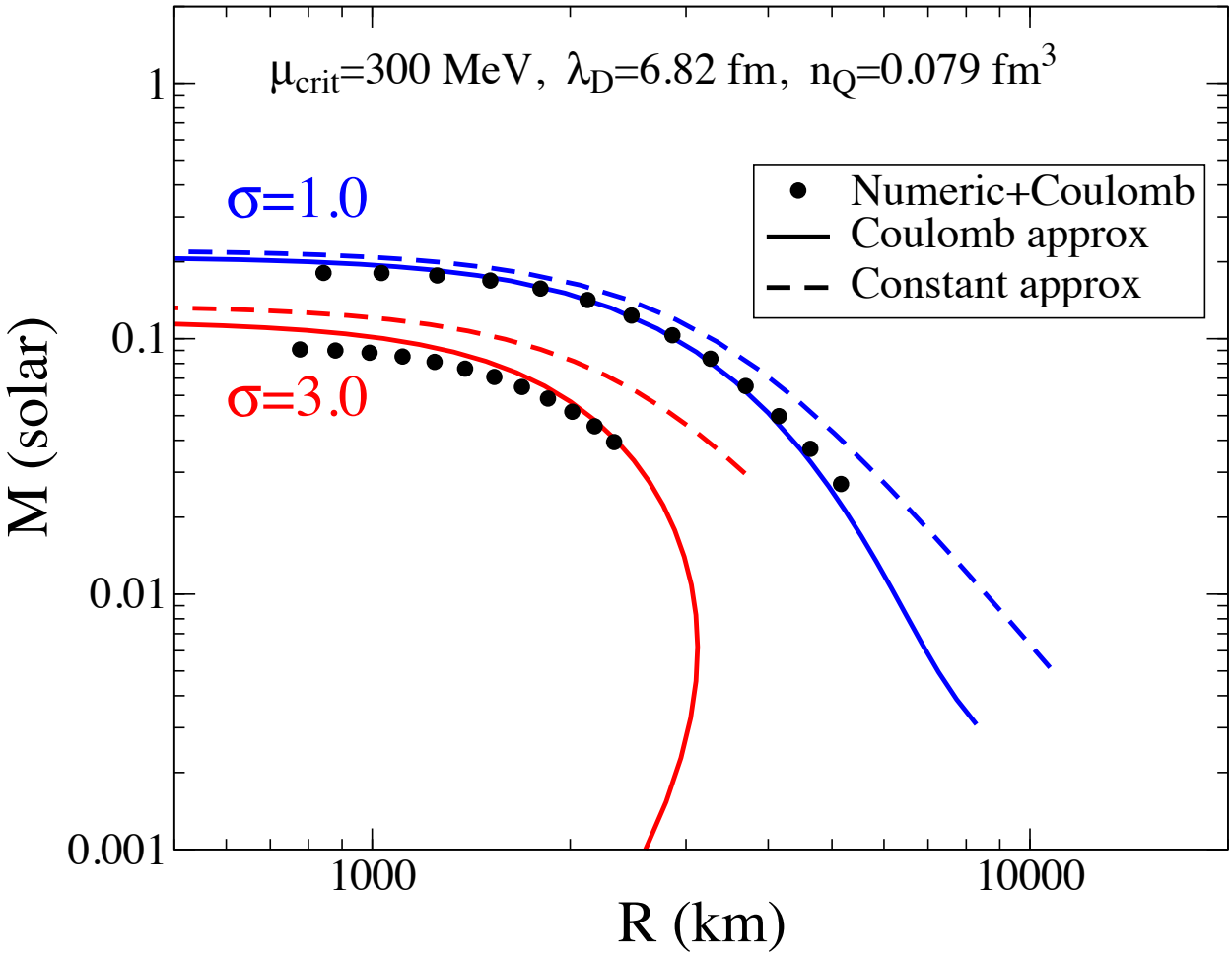

Figure 2.4: Mass-radius relation for strangelet dwarfs made of strangelet crystal matter, comparing different approximations to the equation of state. Upper (blue) curves are for the same parameters as in Figs. 2.1 and 2.2. Lower (red) curves are for a larger surface tension, $\sigma = 3\,\mathrm{MeVfm}^{-2}$. The dots were obtained using the full numerical equation of state (Sec. 2.3.2). The solid lines use the Coulomb-potential approximation (Sec. 2.3.3), and the dashed lines use the constant-potential approximation (2.19).

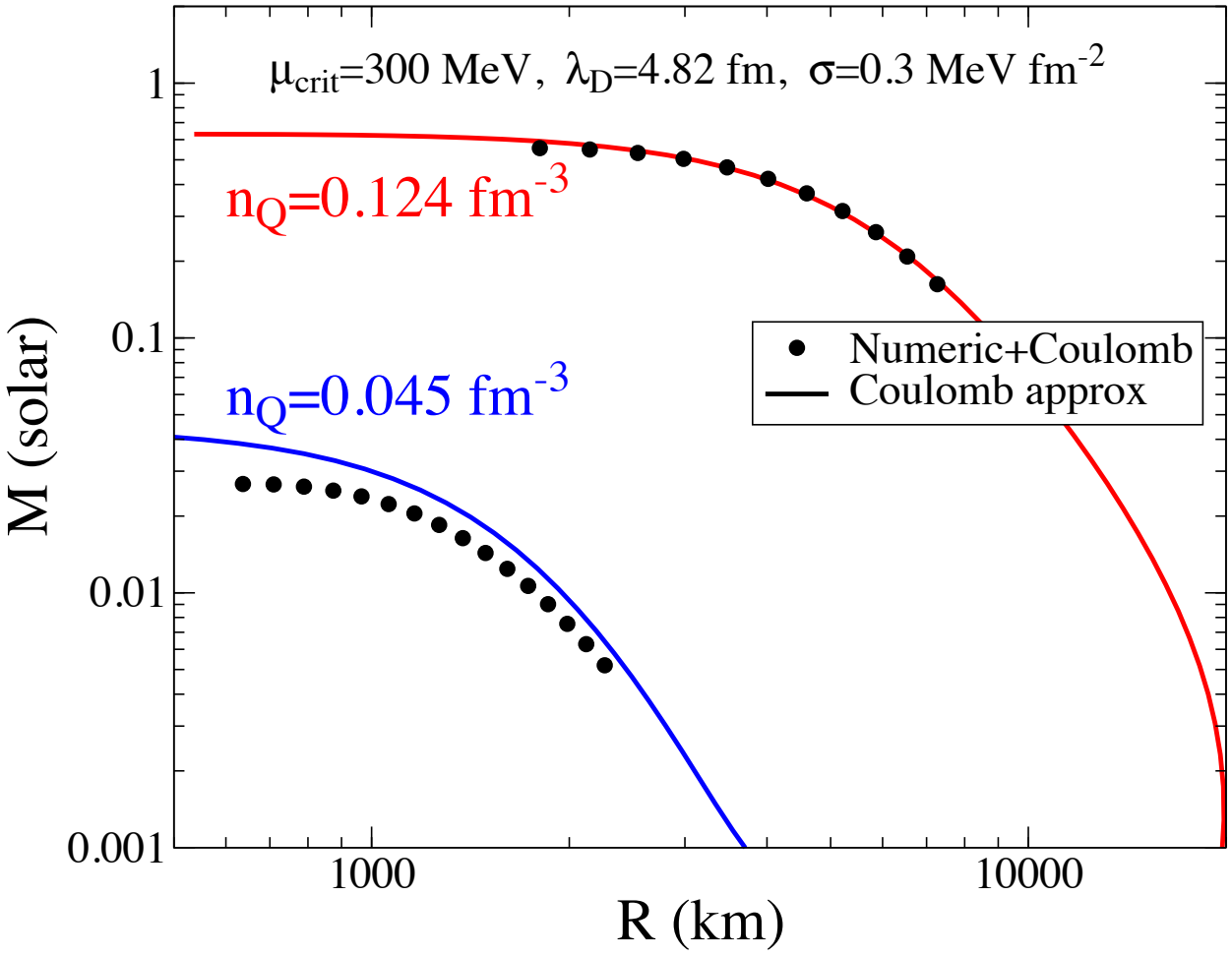

Figure 2.5: Mass-radius relation for strangelet dwarfs made of strangelet crystal matter, comparing different approximations to the equation of state.

Chapter 3

Generic conditions for stable hybrid stars

It is already known [71, 5, 6] that there is a simple criterion, in terms of the discontinuity in the energy density at the transition, that specifies when hybrid stars with an arbitrarily small core (i.e. with central pressure just above the transition) will be stable. In this chapter we look at the properties of the hybrid star branch from the transition up to higher central pressures, assuming that the quark matter EoS has a density-independent speed of sound like a classical ideal gas[1]. We obtain the phase diagram of the possible topological forms of the hybrid star branches, and find that it is fairly insensitive to details of the nuclear matter equation of state. We also investigate the observability of the hybrid star branches, and the maximum mass as a function of the parameters of the quark matter EoS.

[1]For a classical ideal gas, the squared speed of sound $c_s^2 \propto T/m$, where T is the temperature and m is the mass, and is independent of density. For a quantum ideal gas, $c_s^2 = (1/3)\ (1 - (m/\mu)^2)$, where μ is the chemical potential inclusive of mass, and varies between 1/3 (ultra-relativistic case) and $\sim (2/3)\ n^{2/3}$ (the non-relativistic case), where n is the number density.

3.1 Introduction

We assume a generic quark matter equation of state, and see in what ways it might be constrained by measurements of the mass and radii of compact stars. We assume that there is a first-order phase transition between nuclear and quark matter, and that the surface tension of the interface is high enough to ensure that the transition occurs at a sharp interface (Maxwell construction) not via a mixed phase (Gibbs construction). This is a possible scenario, given the uncertainties in the value of the surface tension [72, 73, 74]. (For analysis of generic equations of state that continuously interpolate between the phases to model mixing or percolation, see Refs. [75, 76].)

To address these questions we parameterize the quark matter EoS in terms of three quantities: the pressure $p_{\rm trans}$ of the transition from nuclear matter to quark matter, the discontinuity in energy density $\Delta\varepsilon$ at the transition, and the speed of sound $c_{\rm QM}$ in the quark matter, which we assume remains constant as the pressure varies from $p_{\rm trans}$ up to the central pressure of the maximum mass star. This "CSS" parameterization can be viewed as the lowest-order terms of a Taylor expansion of the quark matter EoS about the transition pressure (see Fig. 3.1),

$$\varepsilon(p) = \begin{cases} \varepsilon_{\rm NM}(p) & p < p_{\rm trans} \\ \varepsilon_{\rm NM}(p_{\rm trans}) + \Delta\varepsilon + c_{\rm QM}^{-2}(p - p_{\rm trans}) & p > p_{\rm trans} \end{cases} , \tag{3.1}$$

where $\varepsilon_{\rm NM}(p)$ is the nuclear matter equation of state. In Appendix A we describe the thermodynamically consistent parameterization of the EoS that we used for quark matter. A similar generic parameterization was proposed in Ref. [77], which also considered the possibility of two first-order transitions involving two different phases of quark matter. See also Ref. [78], which set the speed of sound to 1.

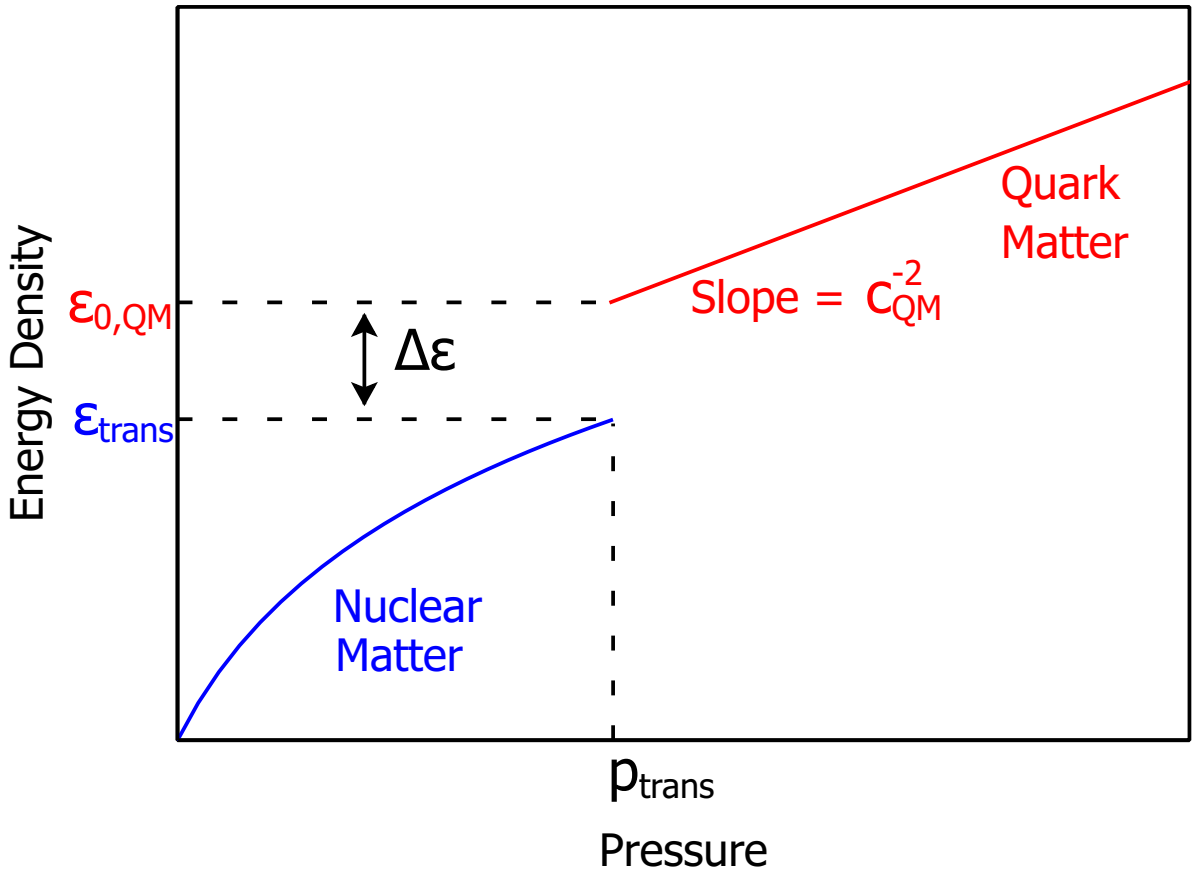

Figure 3.1: Equation of state $\varepsilon(p)$ for dense matter. The quark matter EoS is specified by the transition pressure $p_{\rm trans}$, the energy density discontinuity $\Delta\varepsilon$, and the speed of sound in quark matter $c_{\rm QM}$ (assumed density-independent).

Quark Matter EoS .

The assumption that quark matter has a density-independent speed of sound is reasonably consistent with some well-known quark matter equations of state. For some Nambu–Jona-Lasinio models, the CSS EoS fits Eq. (3.1) almost exactly [77, 79, 80, 81]. In addition, the perturbative quark matter EoS [82] has roughly density-independent $c^2_{\rm QM}$, with a value around 0.2 to 0.3, above the transition from nuclear matter (see Fig. 9 of Ref. [83]). In the quartic polynomial parameterization [84], varying the coefficient a_2 between $\pm(150\text{MeV})^2$,

EoS	max mass	radius at $M = 1.4\,M_\odot$	L
NL3	$2.77\,M_\odot$	14.92 km	118 MeV
HLPS	$2.15\,M_\odot$	10.88 km	33 MeV

Table 3.1: Properties of the NL3 and HLPS equations of state. L characterizes the density-dependence of the symmetry energy (see text). NL3 is an example of a stiff EoS, HLPS is an example of a softer one at density $n \lesssim 4n_0$.

and the coefficient a_4 between 0.6 and 1, and keeping $n_{\rm trans}/n_0$ above 1.5 ($n_0 \equiv 0.16\,{\rm fm}^{-3}$ is the nuclear saturation density), one finds that $c^2_{\rm QM}$ is always between 0.3 and 0.36.

We study hybrid stars for a range of values of $c^2_{\rm QM}$, from 1/3 (characteristic of very weakly interacting massless quarks) to 1 (the maximum value consistent with causality). We expect that this will give us a reasonable idea of the likely range of outcomes for realistic quark matter.

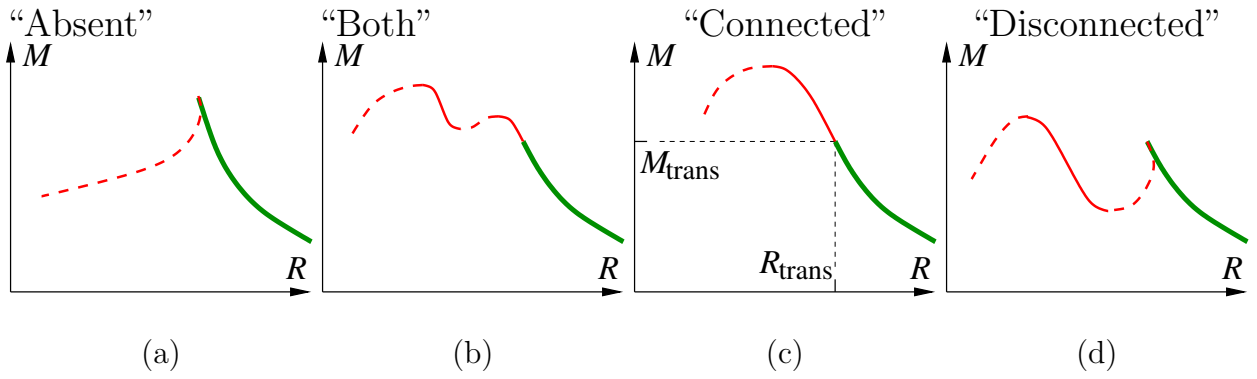

Figure 3.2: Four possible topologies of the mass-radius relation for hybrid stars. The thick (green) line is the hadronic branch. Thin solid (red) lines are stable hybrid stars; thin dashed (red) lines are unstable hybrid stars. In (a) the hybrid branch is absent. In (c) there is a connected branch. In (d) there is a disconnected branch. In (b) there are both types of branch. In realistic neutron star $M(R)$ curves, the cusp that occurs in cases (a) and (d) is much smaller and harder to see [5, 6]

Nuclear Matter EoS Up to densities around nuclear saturation density n_0, the nuclear matter EoS can be experimentally constrained. If one wants to extrapolate it to densities

above n_0, there are many proposals in the literature. For illustrative purposes, we use two examples: a relativistic mean field model, labelled NL3, [85] and a non-relativistic potential model with phenomenological extrapolation to high density, corresponding to "EoS1" in Ref. [86], labelled HLPS. Since HLPS is only defined at $n > 0.5n_0$, we continued it to lower density by switching to NL3 for $n < 0.5n_0$. Some of the properties of HLPS and NL3 are summarized in Table 3.1, where L is related to the derivative of the symmetry energy S_2 with respect to density at the nuclear saturation density, $L = 3n_0(\partial S_2/\partial n)|_{n_0}$.

HLPS is a softer equation of state, with a lower value of L and lower pressure at a given energy density (up to $p \approx 3 \times 10^9\,\mathrm{MeV}^4$, $n \approx 5.5\,n_0$ where its speed of sound rises above 1 and becomes unphysical). NL3 is a stiffer EoS, with higher pressure at a given energy density (also, its speed of sound is less than 1 at all pressures). It yields neutron stars that are larger, and can reach a higher maximum mass.

There is some evidence favoring a soft EoS for nuclear matter: in Ref. [87], values in the range $L = 40$ to 60 MeV were favored from an analysis of constraints imposed by available laboratory and neutron star data. Using data from X-ray bursts, Ref. [88] finds the surface to volume symmetry energy ratio $S_s/S_v \approx 1.5 \pm 0.3$ (See after their Eq. (43) and Table 4), which corresponds to L in the range 22 ± 4 MeV (using Eq. (7) in Ref. [87]).

Nuclear/Quark transition The nuclear matter to quark matter transition occurs at pressure p_{trans}. We will sometimes specify its position in terms of the energy density $\varepsilon_{\mathrm{trans}}$ of nuclear matter at the transition, or the ratio $p_{\mathrm{trans}}/\varepsilon_{\mathrm{trans}}$. Since the nuclear matter EoS has $d^2\varepsilon/dp^2 < 0$ at high densities (Fig. 3.1), p/ε increases monotonically with p, ε, and n, so it is a proxy for the transition pressure or density.

In Sec. 3.2 we discuss the criteria for stable hybrid stars to exist, as a function of the nuclear matter equation of state and the parameters of our generic quark matter equation of state. Sec. 3.3 presents the phase diagram for hybrid star branches as a function of the parameters of the CSS EoS for quark matter. In Sec. 4.2.1 we discuss the maximum mass that such hybrid stars can achieve. Sec. 3.5 gives a summary and conclusions.

3.2 Criterion for Stable Hybrid Stars

3.2.1 Connected hybrid branch

A compact star will be stable as long as the mass M of the star is an increasing function of the central pressure $p_{\rm cent}$ [62]. There will therefore be a stable hybrid star branch in the $M(R)$ relation, connected to the neutron star branch, if the mass of the star continues to increase with $p_{\rm cent}$ when the quark matter core first appears, at $p_{\rm cent} = p_{\rm trans}$.

When the quark matter core is sufficiently small, its effect on the star, and hence the existence of a connected hybrid star branch, is determined entirely by the energy density discontinuity $\Delta\varepsilon$ at its surface, since the quark core is not large enough for the slope ($c_{\rm QM}^{-2}$) of $\varepsilon(p)$ to have much influence on the mass and radius of the hybrid star. This fact was pointed out in Ref. [71] where the dependence on $\Delta\varepsilon$ was expressed in terms of the parameter $q \equiv 1 + \Delta\varepsilon/\varepsilon_{\rm trans}$. A more detailed treatment in Ref. [5, 89] (see also [90, 91]) used a parameter λ with the same definition, and calculated the linear response to a small quark matter core in terms of λ. Ref. [6] used the parameter $\Delta \equiv \Delta\varepsilon/(\varepsilon_{\rm trans}+p_{\rm trans})$ and highlighted the occurrence of a cusp in the $M(R)$ relation (see below).

If $\Delta\varepsilon$ is small then quark matter has a similar energy density to that of nuclear matter, and we expect a connected hybrid branch that looks roughly like a continuation of the nuclear matter branch. If $\Delta\varepsilon$ is too large, then the star becomes unstable as soon as the quark matter core appears, because the pressure of the quark matter is unable to counteract the additional downward force from the gravitational attraction that the additional energy in the core exerts on the rest of the star. By performing an expansion in powers of the size of the quark matter core, one can show [71, 5, 6] that there is a stable hybrid star branch connected to the neutron star branch if $\Delta\varepsilon$ is less than a threshold value $\Delta\varepsilon_{\rm crit}$ given by

$$\frac{\Delta\varepsilon_{\rm crit}}{\varepsilon_{\rm trans}} = \frac{1}{2} + \frac{3}{2}\frac{p_{\rm trans}}{\varepsilon_{\rm trans}} \ . \tag{3.2}$$

(This is $\lambda_{\rm crit} - 1$ in the notation of Ref. [5].) As $\Delta\varepsilon$ approaches the threshold value $\Delta\varepsilon_{\rm crit}$ from below, both $dM/dp_{\rm cent}$ and $dR/dp_{\rm cent}$ approach zero linearly as $p - p_{\rm cent}$, with the result that the slope dM/dR of the mass radius curve is independent of $\Delta\varepsilon$. For $\Delta\varepsilon < \Delta\varepsilon_{\rm crit}$, the hybrid star branch continues with the same slope as the neutron star mass-radius relation at the transition to quark matter. When $\Delta\varepsilon$ exceeds $\Delta\varepsilon_{\rm crit}$, dM/dR is unchanged, but flips around so that there is a cusp when the central pressure reaches $p_{\rm trans}$ [6], at $(M, R) = (M_{\rm trans}, R_{\rm trans})$. This is shown in schematic form in Fig. 3.2, where panels (b) and (c) show possible forms of $M(R)$ for $\Delta\varepsilon < \Delta\varepsilon_{\rm crit}$, and panels (a) and (d) show possible forms for $\Delta\varepsilon > \Delta\varepsilon_{\rm crit}$. In $M(R)$ curves for realistic neutron star equations of state, the cusp at high $\Delta\varepsilon$ is much less clearly visible: the region where the slopes of hybrid and neutron stars match is very small, covering a range in M of less than one part in a thousand near the transition point $(R_{\rm trans}, M_{\rm trans})$ [6].

3.2.2 Disconnected hybrid branch

In Figs. 3.2(b) and (d), we illustrate the occurrence of a second, disconnected, branch of stable hybrid stars at $\Delta\varepsilon > \Delta\varepsilon_{\rm crit}$. This possibility was noted in Ref. [5]. The disconnected branch is a "third family" [92, 93] of compact stars besides neutron stars and white dwarfs. Third families have been found in $M(R)$ calculations for specific quark matter models, for example kaon condensed stars [94], quark matter cores from perturbative QCD [95], and color superconducting quark matter cores [96]. Next we will study the generic features of a quark matter EoS that give rise to this phenomenon. In principle one could imagine that additional disconnected stable branches might occur, but we do not find any with the CSS parameterization of the quark matter EoS.

3.3 "Phase Diagram" for Hybrid Stars

3.3.1 Phase diagram at fixed $c_{\rm QM}$

In Fig. 3.3 we plot a "phase diagram" for hybrid stars, where the control parameters are two of the parameters of the CSS quark matter EoS: $p_{\rm trans}/\varepsilon_{\rm trans}$ (the ratio of pressure to energy density in nuclear matter at the transition pressure) and $\Delta\varepsilon$ (the discontinuity in the energy density at the transition). The quark matter speed of sound is held constant. As noted in Sec. 2.1, $p_{\rm trans}/\varepsilon_{\rm trans}$ increases monotonically with pressure, so it is a proxy for the transition pressure or density. Our phase diagram covers a range in $p_{\rm trans}/\varepsilon_{\rm trans}$ from 0.02 up to about 0.5. Below 0.02 the NL3 EoS has a baryon density far below n_0, and the HLPS EoS has a discontinuity in c^2 that is not physical.

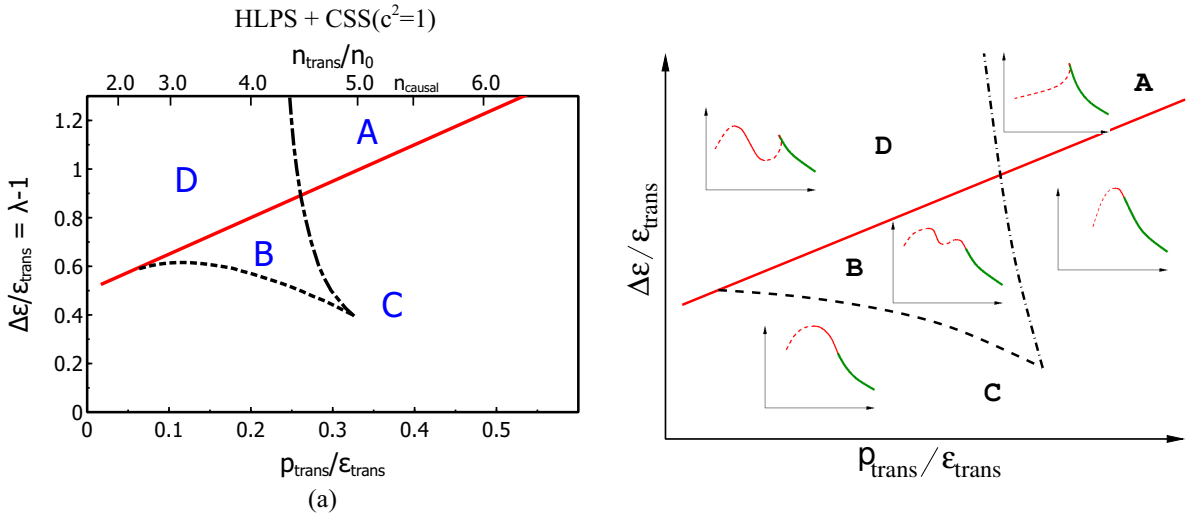

Figure 3.3: Phase diagram for hybrid star branches in the mass-radius relation of compact stars. The control parameters are the pressure $p_{\rm trans}$ and energy density discontinuity $\Delta\varepsilon$ at the transition, each expressed in units of the nuclear energy density at the transition $\varepsilon_{\rm trans}$. The y-axis is therefore just a shifted version of the parameter λ of Ref. [5]. The solid straight line is $\Delta\varepsilon_{\rm crit}$ (Eq. (3.2)). The left panel is the result of calculations for a softer nuclear matter EoS (HLPS) and CSS quark matter with $c^2_{\rm QM} = 1$. The right panel is a schematic showing the topological form of the mass-radius relation in each region of the diagram: regions A,B,C,D correspond to Fig. 3.2(a),(b),(c),(d).

The left panel of Fig. 3.3 is the result of calculations for the HLPS nuclear matter EoS and quark matter with $c^2_{\rm QM} = 1$. The lower x-axis shows $p_{\rm trans}/\varepsilon_{\rm trans}$, which is the natural way to characterize the transition. The upper x-axis shows the corresponding transition baryon density of nuclear matter for the HLPS EoS. HLPS becomes acausal at $n = 5.458\, n_0$, but all the interesting structure in the plot is below this density. The right panel is a schematic showing the form of the mass-radius relation in each region of the diagram. The regions correspond to different topologies of the hybrid branch displayed in Fig. 3.2: A="Absent", C="Connected", D="Disconnected", B="Both" (connected and disconnected).

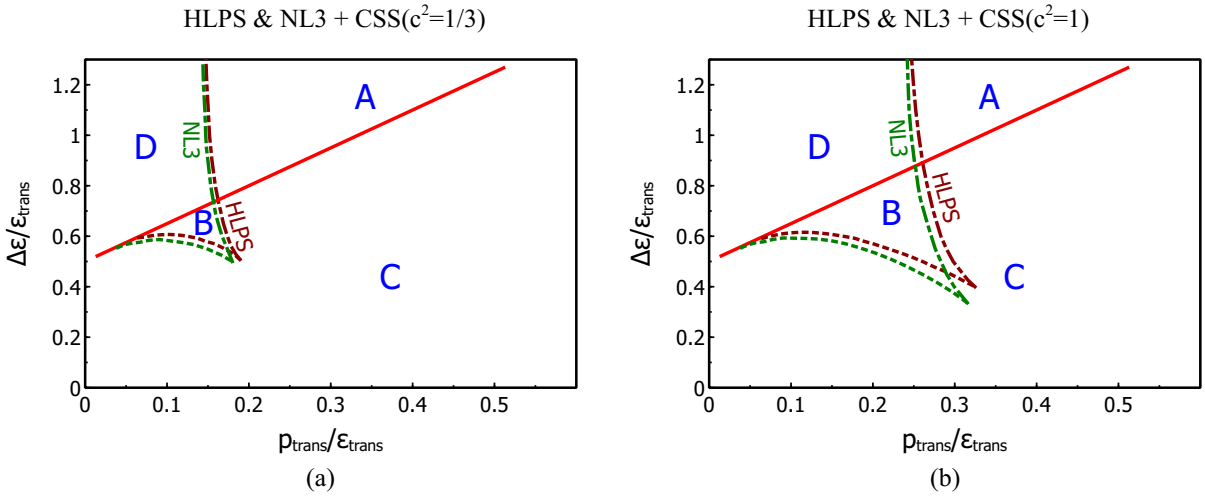

Figure 3.4: Phase diagram like Fig. 3.3, showing that the phase boundaries are not very sensitive to changes in the nuclear matter EoS, but they are affected by varying the quark matter speed of sound.

The solid straight (red) line is $\Delta\varepsilon_{\rm crit}$ from Eq. (3.2). On crossing this line $M'(p_{\rm cent})$ and $R'(p_{\rm cent})$ both change sign when quark matter first appears, causing the $M(R)$ curve to undergo a discontinuous change, flipping around from being "upward-pointing" (mass increases with central pressure) and continuous, to being "downward-pointing" (mass decreases with central pressure) with a cusp. Below the line ($\Delta\varepsilon < \Delta\varepsilon_{\rm crit}$), in regions B and C, there is a hybrid star branch connected to the nuclear star branch. Above the line ($\Delta\varepsilon > \Delta\varepsilon_{\rm crit}$), in regions A and D, there is no connected hybrid star branch. In regions B and D there is a disconnected hybrid star branch.

The roughly vertical dash-dotted curve in Fig. 3.3 marks a transition where an additional disconnected branch of hybrid stars appears/disappears. When one crosses this line from the right, going from region A to D by decreasing the nuclear/quark transition density, a stationary point of inflection appears in $M(p_{\rm cent})$ at $p_{\rm cent} > p_{\rm trans}$. If one crosses from C to B then this point of inflection is at lower central pressure than the existing maximum in

$M(p_{\rm cent})$. This produces a stationary point of inflection in the $M(R)$ relation to the left of the existing maximum (if any). After crossing the dash-dotted line the point of inflection becomes a new maximum-minimum pair (the maximum being further from the transition point), producing a disconnected branch of stable hybrid stars in regions B and D. Crossing the other way, by increasing the transition pressure, the maximum and minimum that delimit the disconnected branch merge and the branch disappears.

The roughly horizontal dashed curve in Fig. 3.3 which separates region B and C marks a transition between mass-radius relations with one connected hybrid star branch, and those with two hybrid star branches, one connected and one disconnected. In the notation of Ref. [97] (sec. (4.2)), this line corresponds to $\Delta\varepsilon/\varepsilon_{\rm trans} = \lambda_{\rm max} - 1$. Crossing this line from below, by increasing the energy density discontinuity, a stationary point of inflection in $M(p_{\rm cent})$ (or equivalently in $M(R)$) appears in the existing connected hybrid branch. Crossing in to region B, this point of inflection becomes a new maximum-minimum pair, so the connected hybrid branch is broken in to a smaller connected branch and a new disconnected branch. The maximum of the old connected branch smoothly becomes the maximum of the new disconnected branch. If one crossed the dashed line in the opposite direction, from B to C, the maximum closest to the transition point would approach the minimum and they would annihilate, leaving only the more distant maximum.

Where the horizontal and vertical curves meet, the two maxima and the minimum that are present in region B all merge to form a single flat maximum where the first three derivatives of $M(R)$ are all zero.

Along the critical line Eq. (3.2), which is the straight line in Fig. 3.3, $dM/dp_{\rm cent} = 0$ at $p_{\rm cent} = p_{\rm trans}$. We now discuss the curvature $M'' \equiv d^2M/dp_{\rm cent}^2$ at $p_{\rm cent} = p_{\rm trans}$ on that line. On the A/C boundary, $M'' < 0$. In region C there is a maximum in $M(p_{\rm cent})$ at

$p_{\rm cent} > p_{\rm trans}$, but on the A/C boundary that maximum has shifted to $p_{\rm cent} = p_{\rm trans}$. As we move down the A/C boundary, M'' becomes less negative. This continues along the B/D boundary, until at the point where the B/C boundary (dashed line) merges with the B/D boundary, $M'' = 0$. This is because the stationary point of inflection in $M(p_{\rm cent})$ (where the disconnected branch first appears) has now arrived at $p_{\rm cent} = p_{\rm trans}$. Continuing down the critical line, M'' becomes positive, making it possible for there to be a direct transition between C and D.

3.3.2 Varying $c_{\rm QM}$ and the nuclear EoS

Up to now we have discussed the effects of varying two of the parameters of the quark matter EoS, namely $p_{\rm trans}$ and $\Delta\varepsilon$. In Fig. 3.4 we show the effects of varying the third parameter, the speed of sound, and the effect of varying the nuclear matter EoS. Fig. 3.4(a) is the phase diagram for CSS quark matter with $c^2_{\rm QM} = 1/3$, and Fig. 3.4(b) is for $c^2_{\rm QM} = 1$. In both panels we show the phase diagram for a softer (HLPS) nuclear matter EoS and a harder (NL3) nuclear matter EoS. As expected from Eq. (3.2) the straight line where the connected hybrid branch disappears is independent of $c^2_{\rm QM}$ and the detailed form of the nuclear matter EoS. The other phase boundaries, outlining the region where there is a disconnected hybrid branch, are remarkably insensitive to the details of the nuclear matter EoS. However, they depend strongly on the quark matter speed of sound. For a given nuclear matter EoS the hybrid branch structure is determined by $p_{\rm trans}/\varepsilon_{\rm trans}$, $\Delta\varepsilon/\varepsilon_{\rm trans}$, and $c^2_{\rm QM}$, so one could make a three-dimensional plot with $c^2_{\rm QM}$ as the third axis, but this figure adequately illustrates the dependence on $c^2_{\rm QM}$. We will now discuss the physics behind the shape of the phase boundaries.

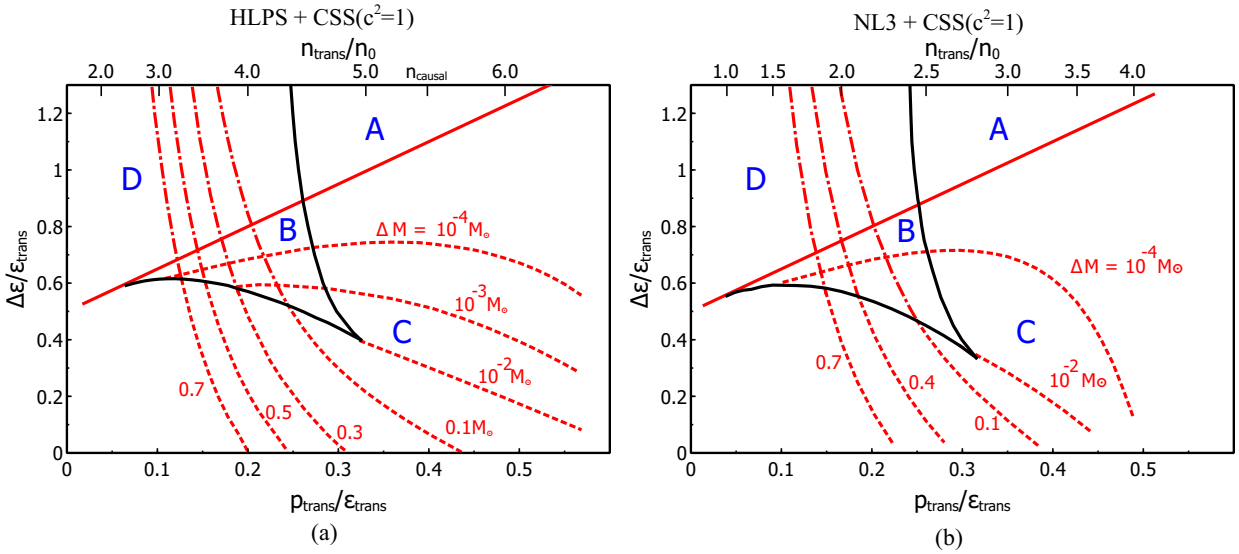

Figure 3.5: Contour plot of a measure of the observability of hybrid branches: ΔM, the mass difference between the heaviest hybrid star and the hadronic star when quark matter first appears. We show results for HLPS and NL3 nuclear matter, with $c^2_{\rm QM} = 1$ CSS quark matter. The contours are not very sensitive to details of the nuclear matter EoS. If the transition density is high, or if a disconnected branch is present, the connected branch may be very small and hard to observe.

3.3.3 Physical understanding of the phase diagram

The main feature of the phase diagram is that a disconnected branch is present when the transition density is sufficiently low, and the energy density discontinuity is sufficiently high, namely in regions B and D. It occurs more readily (i.e. those regions are larger) if the speed of sound in quark matter is high. Such features were noticed in the context of stars with mixed phases in Ref. [75], which pointed out that they can be understood as follows.

When a very small quark matter core is present, its greater density creates an additional gravitational pull on the nuclear mantle. If the pressure of the core can counteract the extra pull, the star is stable and there is a connected hybrid branch (regions C and B). If the energy

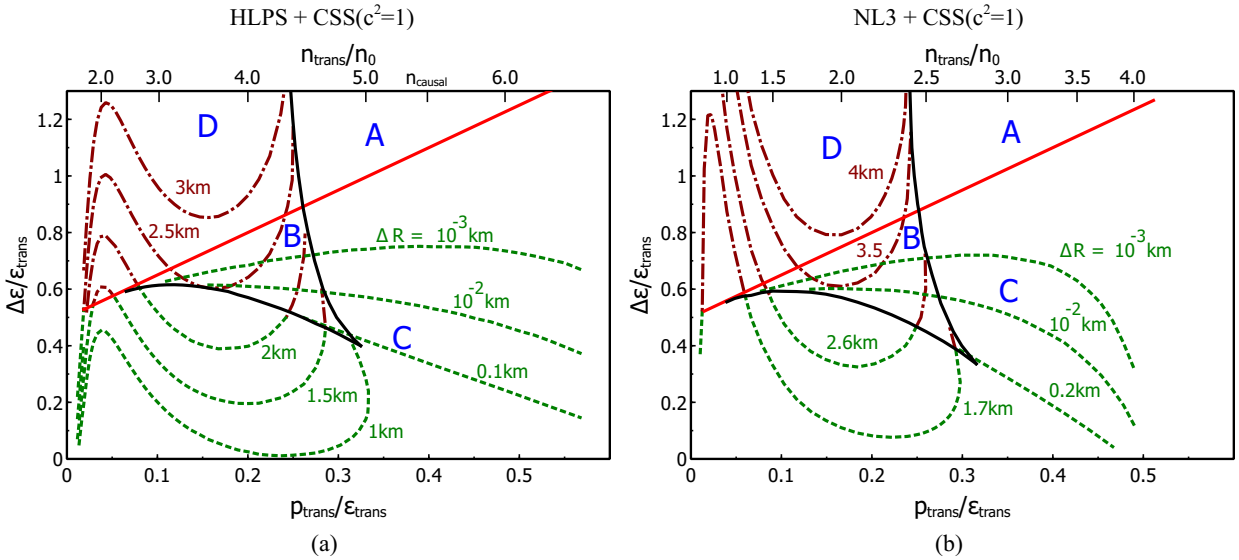

Figure 3.6: Contour plot of a measure of the observability of hybrid branches: ΔR, the difference between the radius of the hadronic star when quark matter first appears and the radius of the heaviest hybrid star. We show results for HLPS and NL3 nuclear matter, with $c^2_{\rm QM} = 1$ CSS quark matter. The contours are not very sensitive to details of the nuclear matter EoS. If the transition density is high, or if a disconnected branch is present, the connected branch may be very small and hard to observe.

density jump is too great, the extra gravitational pull is too strong, and the star becomes unstable when quark matter first appears (regions A and D). However, if the energy density of the core rises slowly enough with increasing pressure (i.e. if $c^2 = dp/d\varepsilon$ is large enough), a larger core with a higher central pressure may be able to sustain the weight of the nuclear mantle above it (region D). Region B, with connected and disconnected branches, is more complicated and we do not have an intuitive explanation for it.

We can now understand why the vertical line marking the B/C and D/A boundaries moves to the right as $c^2_{\rm QM}$ increases. Since $c^2 = dp/d\varepsilon$, if $c^2_{\rm QM}$ is larger then the energy density of the core rises more slowly with increasing pressure, which minimizes the tendency for a large core to destabilize the star via its gravitational attraction. Finally, we can see why that line

has a slight negative slope: larger $\Delta\varepsilon$ makes the quark core heavier, increasing its pull on the nuclear mantle, and making the hybrid star more unstable against collapse.

Ref. [75], assuming a mixed phase, conjectured that the third family (disconnected branch) exists when the speed of sound in quark matter is higher than that in the mixed phase. However, our results do not support that conjecture. In the case we study, with no mixed phase, the relevant quantity would be the difference between $c_{\rm QM}$ (the speed of sound in quark matter) and $c_{\rm NM}$ (the speed of sound in nuclear matter at the phase transition). If the conjecture were correct, our phase diagram (which is for fixed $c_{\rm QM}$) would show the disconnected branch appearing at a vertical phase boundary located at the transition pressure where $c_{\rm NM} = c_{\rm QM}$. In fact, as seen in Fig. 3.4, we find one horizontal phase boundary, and a near-vertical boundary. For $c^2_{\rm QM} = 1$ quark matter the vertical boundary occurs at $p_{\rm trans}/\varepsilon_{\rm trans} \approx 0.3$ where $c^2_{\rm NM} \approx 0.75$ for HLPS and $c^2_{\rm NM} \approx 0.65$ for NL3. For $c^2_{\rm QM} = 1/3$ quark matter the vertical boundary occurs at $p_{\rm trans}/\varepsilon_{\rm trans} \approx 0.15$ where $c^2_{\rm NM} \approx 0.5$ for HLPS and NL3. We conclude that the appearance of a disconnected branch is not determined by whether $c_{\rm QM} > c_{\rm NM}$.

3.3.4 Observability of hybrid branches

The phase diagrams of the previous subsection show us when connected and disconnected branches are present, but for astrophysical observations it is important to know how easily these branches could be detected via measurements of the mass and radius of compact stars. In Figs. 3.5 and 3.6 we show the phase diagram for HLPS and NL3 nuclear matter, with $c^2_{\rm QM} = 1$ quark matter, with contours showing two measures, ΔM and ΔR, of the length of the hybrid branch. ΔM is the difference in mass between the heaviest hybrid

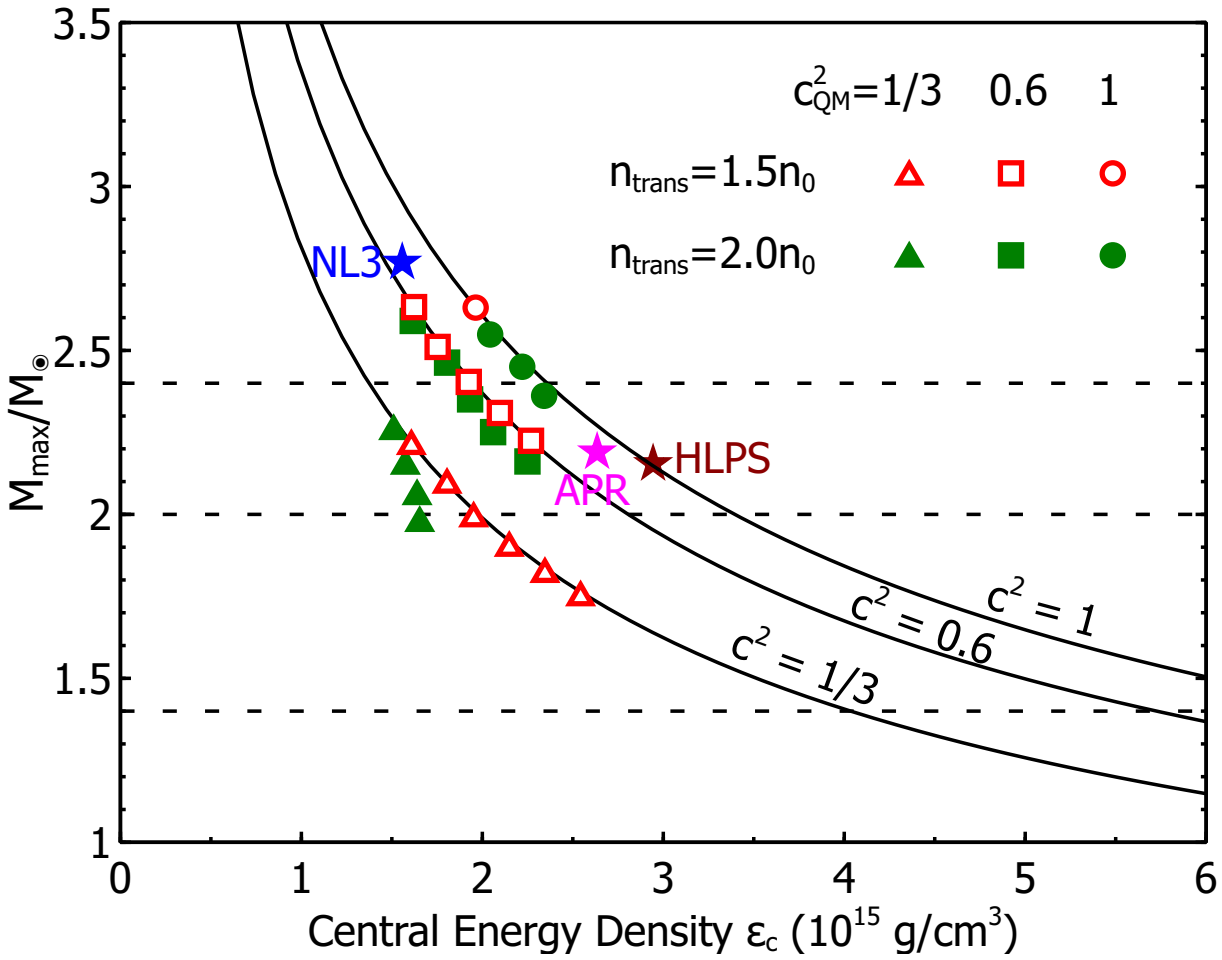

Figure 3.7: Mass of the heaviest hybrid star as a function of its central energy density, for various quark matter equations of state (3.1). The curves are predictions of Ref. [7] for stars whose core-region speed of sound squared is 1, 0.6, and 1/3. Pure nuclear matter stars for the NL3 and APR equations of state are also plotted.

star and the hadronic star just before quark matter appears (whose mass is $M_{\rm trans}$). ΔR is the difference in radius between the hadronic star just before quark matter appears (whose radius is $R_{\rm trans}$) and the heaviest hybrid star. At the horizontal boundary between region C and B, the maximum of the connected branch smoothly becomes the maximum of the disconnected branch (see Fig. 3.3) so the dashed contours (for the connected branch) connect smoothly to the dot-dashed contours (for the disconnected branch). We see that the ΔM and ΔR contours are roughly independent of details of the nuclear matter EoS, except at high transition pressure where the transition to quark matter is happening close to the maximum of the nuclear EoS, which greatly suppresses the length of the connected branch. Note that although we only show contours for positive ΔM and ΔR, contours that end on the A/D or near-vertical B/C boundary can have negative ΔM.

From Figs. 3.5 and 3.6 we conclude that Eq. (3.2) is not a good guide to the presence of *observable* hybrid branches. The connected branch may be very small and hard to detect, even at values of $\Delta\varepsilon/\varepsilon_{\rm trans}$ well below the critical value of Eq. (3.2). For the $c^2_{\rm QM} = 1$ case, only in the parts of region C that lie approximately below region B (i.e. for $p_{\rm trans}/\varepsilon_{\rm trans} \lesssim 0.3$) is the connected hybrid branch large enough to be detectable via observations of mass that have an experimental uncertainty of around $0.01 M_\odot$ or observations of radius that have an uncertainty of around 0.2 km. When a disconnected branch is present, the connected branch is either absent (region D) or too small to observe (region B).

The disconnected branch itself, whose presence has nothing to do with Eq. (3.2), is in principle easily observable except perhaps at the far right edge of regions B and D. The natural way for the disconnected branch to be populated would be via accretion, taking a star to the top of the connected branch, after which it would have to collapse to the disconnected branch, with dramatic emission of neutrinos and gamma rays [98] and gravitational waves

[99]. It is not clear how one would populate the parts of the disconnected branch that lie below that mass threshold, so one might end up with a gap in the observed radii of neutron stars, where the populated sequence jumps from one branch to the other.

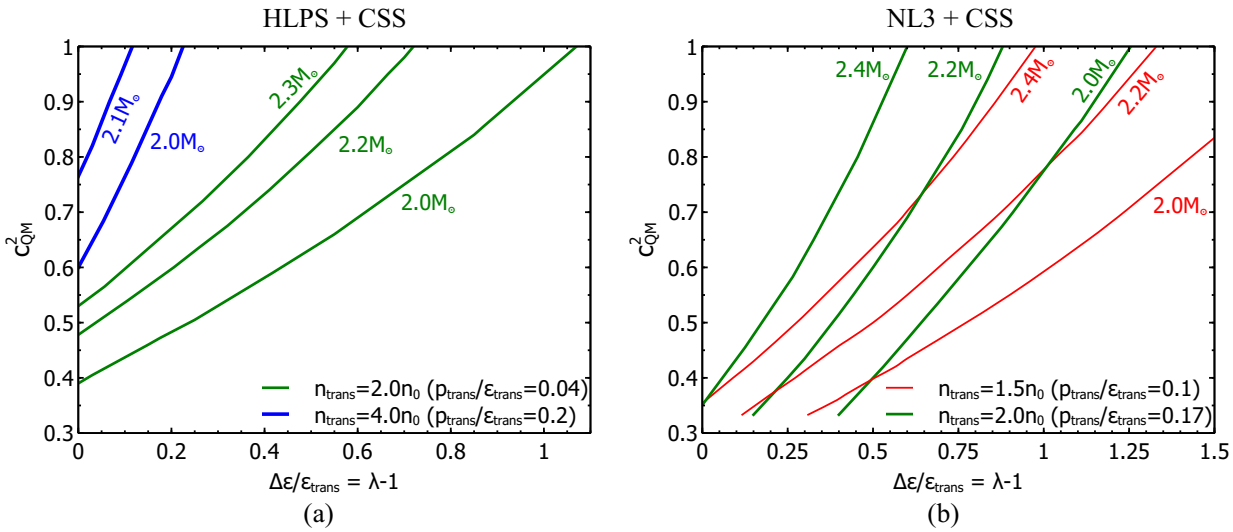

Figure 3.8: Contour plot of the mass of the heaviest hybrid star as a function of quark matter EoS parameters $p_{\rm trans}/\varepsilon_{\rm trans}$, $c^2_{\rm QM}$, and $\Delta\varepsilon/\varepsilon_{\rm trans}$ (a shifted version of λ in Ref. [5]) for HLPS and NL3 nuclear matter. The thin (red), medium (green) and thick (blue) lines are for a nuclear to quark transition at $n_{\rm trans} = 1.5n_0$, $2n_0$, and $4n_0$, respectively.

3.4 Maximum Mass of Hybrid Stars

3.4.1 Maximum mass and central energy density

The CSS quark matter EoS (3.1) involves three parameters, $p_{\rm trans}$ (or equivalently $n_{\rm trans}$), $\Delta\varepsilon$, and $c_{\rm QM}$. The results of Ref. [100, 7] lead us to expect that, for a given nuclear matter EoS, the maximum mass $M_{\rm max}$ is mostly determined by the central energy density of the

heaviest star and the speed of sound in the central regions of that star. Specifically,

$$M_{\rm max} \stackrel{?}{=} y(c_{\rm cent})\varepsilon_{\rm cent}^{-1/2} \ . \tag{3.3}$$

The function $y(c_{\rm cent})$ can be obtained from Ref. [7] (their Eq. (24) and the associated table). To test Eq. (3.3), we follow Ref. [100, 7] and plot the maximum mass $M_{\rm max}$ that a stable star can have, as a function of the central energy density in that star $\varepsilon_{\rm cent}$. We use the NL3 nuclear matter EoS and repeat the calculation for a range of quark matter equations of state, varying the transition density $n_{\rm trans}$ for the transition to quark matter, the quark matter speed of sound $c_{\rm QM}$, and the energy density discontinuity $\Delta\varepsilon$ at the transition. The range of allowed values of $\Delta\varepsilon$, giving stable hybrid stars is from zero to $\Delta\varepsilon_{\rm crit}(n_{\rm trans})$.

The results are shown in Fig. 3.7, where we use the NL3 nuclear matter EoS and CSS Quark Matter. The solid curves show $M_{\rm max}(\varepsilon_{\rm cent})$ according to Eq. (3.3) for $c^2_{\rm cent} = 1$, 0.6, and 1/3. Nuclear matter equations of state at high density have c^2 close to 1, hence the maximum masses for pure nuclear matter stars (we show the result for APR [9] nuclear matter as well as NL3 and HLPS) lie close to the $c^2_{\rm cent} = 1$ line.

The triangles, squares, and circles show the masses of hybrid stars for a quark matter EoS with relatively low transition densities: $n_{\rm trans} = 1.5\, n_0$ (open symbols) or $n_{\rm trans} = 2\, n_0$ (solid symbols), and for each of these we vary $c_{\rm QM}$ and $\Delta\varepsilon$. The low transition density means that these hybrid stars have large quark matter cores, so the the speed of sound in the central part of the star is $c_{\rm QM}$, so the maximum masses should fall on the lines given by Eq. (3.3) with $c_{\rm cent} = c_{\rm QM}$. We see that on the whole this is the case. However, for $n_{\rm trans} = 2.0\, n_0$ and $c^2_{\rm QM} = 1/3$ (solid triangles) the points fall slightly below the predicted $c^2_{\rm QM} = 1/3$ line. This implies that in these stars the effective speed of sound in the core is even lower than $1/\sqrt{3}$.

However, the speed of sound in the NL3 nuclear matter mantle at $n \sim 2n_0$ is greater than $1/\sqrt{3}$. It seems reasonable to argue that the first-order phase transition, at which $dp/d\varepsilon = c^2$ vanishes, acts like a "soft" region where c is small [77], and drags down the average value of $c_{\rm cent}$. All hybrid stars have such a transition region, but in these stars the quark matter cores are smaller than in the other cases, so the nuclear-quark matter boundary is closer to the center of the star, and by the conjecture of Ref. [100] it is expected to play a more important role in determining the maximum mass.

3.4.2 How heavy can a hybrid star be?

Using the CSS parameterization (3.1) of the quark matter EoS, it is possible to get hybrid stars that are heavy enough to be consistent with recent measurements of stars of mass $2\,M_\odot$ [1, 23]. In Fig. 3.8 we show contour plots for the maximum masses of hybrid stars as a function of the parameters of the quark matter EoS, for both the HLPS and NL3 nuclear equations of state. Fig. 3.8 is a generalization of Fig. 10 of Ref. [77], showing the effect of different nuclear matter EoSs and different transition densities.

We see that, as expected from Fig. 3.3, hybrid stars will be heavier if the energy density discontinuity $\Delta\varepsilon$ is smaller (so the gravitational pull of the core does not destabilize the star) and the speed of sound in quark matter is higher (so the core is stiffer and can support a heavy star).

For the softer HLPS EoS, whose pure nuclear matter star has a maximum mass of $2.15\,M_\odot$ (Table 3.1), hybrid stars can be heavier than the pure nuclear star. This occurs when the transition density is low, and the quark core is a large fraction of the star. In the $M(R)$ relation, the hybrid branch can have a positive dM/dR, so its $M(R)$ curve looks similar to

that of a pure quark matter star, rising to a maximum mass star which is heavier and larger than the heaviest pure HLPS star. For the harder NL3 EoS, whose pure nuclear matter star has a maximum mass of $2.77\,M_\odot$, hybrid stars are always lighter than the heaviest nuclear matter star.

3.4.3 The quark matter mass fraction

For hybrid stars, it is natural to ask how much of the mass of the star consists of quark matter. We define the quark matter mass fraction $f_q \equiv M_{\rm core}/M_{\rm star}$. In Fig. 3.8(a), along the thick (blue, $n_{\rm trans} = 4n_0$) contours of constant $M_{\rm star}$, f_q varies from about 60% at low $c^2_{\rm QM}$ and $\Delta\varepsilon$ to about 70% at high $c^2_{\rm QM}$ and $\Delta\varepsilon$. If the transition pressure is lower then we expect the quark fraction to be larger: along the medium-thickness (green) mass contours for $n_{\rm trans} = 2n_0$, f_q varies from about 90% at low $c^2_{\rm QM}$ and $\Delta\varepsilon$ to about 96% at high $c^2_{\rm QM}$ and $\Delta\varepsilon$.

In Fig. 3.8(b), along the medium-thickness (green) mass contours for $n_{\rm trans} = 2n_0$, f_q varies from about 50% at low $c^2_{\rm QM}$ and $\Delta\varepsilon$ to about 80% at high $c^2_{\rm QM}$ and $\Delta\varepsilon$. Again, if the transition pressure is lower then the quark fraction is larger: along the thin (red) mass contours for $n_{\rm trans} = 1.5n_0$, f_q varies from about 80% at low $c^2_{\rm QM}$ and $\Delta\varepsilon$ to over 90% at high $c^2_{\rm QM}$ and $\Delta\varepsilon$.

3.5 Conclusions

In this chapter we studied hybrid stars where there is a sharp interface between two phases with different equations of state. We called the two phases "nuclear matter" and "quark

matter", but our conclusions are valid for any first-order phase transition between two phases with different energy densities.

It is already known that in the presence of such a first-order phase boundary there will be a stable connected branch of hybrid stars if the energy density discontinuity $\Delta\varepsilon$ at the transition is less than a critical value $\Delta\varepsilon_{\rm crit}$ (Eq. (3.2)) which depends only on the ratio of pressure to nuclear matter energy density at the transition. We confirmed this result and investigated the conditions for the occurrence of a disconnected hybrid branch, and the visibility of the hybrid branches. To study these properties of hybrid stars we used a fairly generic parameterization (CSS) of the quark matter EoS at densities beyond the transition, and came to the following conclusions.

1) Even if there is no connected hybrid star branch, there may be a disconnected one if the transition density is low enough and the speed of sound is high enough so that the nuclear mantle can be supported by a large enough quark matter core, and the energy density discontinuity is large enough so that a medium-sized core has insufficient pressure to support the nuclear mantle (see Fig. 3.3).

2) The phase diagram for disconnected hybrid star branches is largely determined by the parameters of the QM EoS, $p_{\rm trans}/\varepsilon_{\rm trans}$, $\Delta\varepsilon/\varepsilon_{\rm trans}$, and $c^2_{\rm QM}$. It is not very sensitive to the detailed form of the nuclear matter EoS.

3) Even if, according to the standard criterion (3.2), a connected hybrid branch is present, it may be so short as to be very hard to detect by measurements of the mass and radius of the star (see Fig. 3.5). When a disconnected branch is present, the connected branch is either absent or very small.

4) We confirmed that the relationship (3.3) between the maximum mass of a star and its central energy density, which was proposed in Ref. [7], holds for hybrid stars (see Fig. 3.7).

5) We found that it is possible to get heavy hybrid stars (more than $2\,M_\odot$) for reasonable

parameters of the quark matter EoS. It requires a not-too-high transition density ($n_{\rm trans} \sim 2n_0$), low enough energy density discontinuity $\Delta\varepsilon \lesssim 0.5\varepsilon_{\rm trans}$, and high enough speed of sound $c^2_{\rm QM} \gtrsim 0.4$). It is interesting to note that free quark matter would have $c^2_{\rm QM} = 1/3$, and a value of $c^2_{\rm QM}$ that is well above 1/3 is an indication that the quark matter is strongly coupled. For a stiff nuclear matter EoS such as NL3 it was somewhat easier to make heavy hybrid stars. Details are presented in Fig. 3.8. Our findings provide a generic formulation of the results found in previous calculations for specific models of quark matter, e.g., [84, 76], which found that in the absence of theoretical or experimental constraints on the quark matter EoS, one can fairly easily vary the unknown parameters of that EoS to obtain heavy hybrid stars. For now, it seems clear that without theoretical advances that constrain the form of the quark matter EoS, measurements of gross features of the $M(R)$ curve such as the maximum mass will not be able to rule out the presence of quark matter in neutron stars.

Our overarching message is that the generic CSS parameterization of the quark matter EoS (also used in Ref. [77]) provides a general framework for comparison and empirical testing of models of the quark matter EoS. Any particular model can be characterized, at least at densities that are not too far from the transition, in terms of its values of the parameters $p_{\rm trans}/\varepsilon_{\rm trans}$, $\Delta\varepsilon/\varepsilon_{\rm trans}$, and $c^2_{\rm QM}$, and its predictions for hybrid stars will follow from these values, which determine its position in the phase diagram (Fig. 3.3). If the form of the nuclear matter EoS were established then measurements of the $M(R)$ relation of neutron stars could be directly expressed as constraints on the values of our quark matter EoS parameters.

The CSS parameterization relies on the assumption of a density-independent speed of sound, which is a useful starting point for general comparisons between quark matter models, as well as providing specific examples of quark matter equations of state that can yield heavy hybrid stars (Fig. 3.8). If observations of $M(R)$ for heavy stars turned out to be inconsistent

with this parameterization, or if theorists were able to show that the speed of sound in quark matter has significant density dependence, then this approach could be further generalized (at the penalty of introducing more parameters) to allow for that, and to allow for mixed or percolated phases as noted in Refs. [75, 76].

Finally, it would be valuable to extend the work reported here by studying rotating hybrid stars using the CSS parameterization. It is interesting to note that a study of a wide range of quark matter EoSs [97] found that the topology of the hybrid branch was not affected by rotation.

Chapter 4

Constraining and applying a generic high-density equation of state

There are many models of matter at density significantly above nuclear saturation density, each with their own parameters. In studying the equation of state (EoS) of matter in this regime it is therefore useful to have a general parameterization of the EoS which can be used as a generic language for relating different models to each other and for expressing experimental constraints in model-independent terms. In this chapter we use the "Constant Speed of Sound" (CSS) parameterization proposed in the previous chapter and show how mass and radius observations can be expressed as constraints on the CSS parameters. Here we analyze a specific example, where the high-density matter is quark matter described by a model based on the Field Correlator Method (Sec. 4.3), showing how its parameters can be mapped on to the CSS parameter space, and how it is constrained by currently available observations of neutron stars.

4.1 Introduction

The CSS parameterization is applicable to high-density equations of state for which: (a) there is a sharp interface between nuclear matter and a high-density phase which we will call "quark matter", even when (as in Sec. 4.2) we do not make any assumptions about its physical nature; (b) the speed of sound in the high-density matter is pressure-independent for pressures ranging from the first-order transition pressure up to the maximum central pressure of neutron stars. One can then write the high-density EoS in terms of three parameters: the pressure $p_{\rm trans}$ of the transition, the discontinuity in energy density $\Delta\varepsilon$ at the transition, and the speed of sound $c_{\rm QM}$ in the high-density phase (See Eq. 3.1). As in the previous chapter, we express the three parameters in dimensionless form, as $p_{\rm trans}/\varepsilon_{\rm trans}$, $\Delta\varepsilon/\varepsilon_{\rm trans}$ (equal to $\lambda - 1$ in the notation of Ref. [5]) and $c^2_{\rm QM}$, with $\varepsilon_{\rm trans} = \varepsilon_{\rm NM}(p_{\rm trans})$.

In Sec. 4.2 we show how the CSS parameterization is constrained by observables such as the maximum mass $M_{\rm max}$, the radius of a maximum-mass star, and the radius $R_{1.4}$ of a star of mass $1.4\,M_\odot$. In Sec. 4.3 we describe a specific model, based on a Brueckner-Hartree-Fock (BHF) calculation of the nuclear matter EoS and the Field Correlator Method (FCM) for the quark matter EoS. We show how the parameters of this model map on to part of the CSS parameter space, and how the observational constraints apply to the FCM model parameters. Sec. 4.4 gives our conclusions.

4.2 Constraining the CSS Parameters

Once a nuclear matter EoS has been chosen, any high-density EoS that is well-approximated by the CSS parameterization can be summarized by giving the values of the three CSS

parameters, corresponding to a point in the phase diagram. We then know what sort of hybrid branches will be present (Sec. 3.3).

4.2.1 Maximum mass of hybrid stars

property	BHF, Av_{18} + UVIX TBF	DBHF, Bonn A
saturation baryon density $n_0(\mathrm{fm}^{-3})$	0.16	0.18
binding energy/baryon E/A (MeV)	-15.98	-16.15
compressibility K_0 (MeV)	212.4	230
symmetry energy S_0 (MeV)	31.9	34.4
$L = 3n_0\,[dS/n]_{n_0}$ (MeV)	52.9	69.4
max mass of star ($M_\odot$)	2.03	2.31
radius of the heaviest star (km)	9.92	11.26
radius of $M = 1.4\,M_\odot$ star (km)	11.77	13.41

Table 4.1: Calculated properties of symmetric nuclear matter for the BHF and DBHF nuclear equations of state used here. BHF is softer, DBHF is stiffer.

In Fig. 4.1 we show how mass measurements of neutron stars can be expressed as constraints on the CSS parameters. Each panel shows dependence on $p_{\mathrm{trans}}/\varepsilon_{\mathrm{trans}}$ and $\Delta\varepsilon/\varepsilon_{\mathrm{trans}}$ for fixed c^2_{QM}, as in the left panel of Fig. 3.3. The region in which the transition to quark matter would occur below nuclear saturation density ($n_{\mathrm{trans}} < n_0$) is excluded (hatched band at left end) because in that region bulk nuclear matter would be metastable. There is also an upper limit on the transition pressure, which is the central pressure of the heaviest stable nuclear matter star. This depends on the hadronic EoS that had been assumed.

The contours show the maximum mass of a hybrid star as a function of the EoS parameters. The region inside the $M = 2\,M_\odot$ contour corresponds to EoSes for which the maximum mass is less than $2\,M_\odot$ so it is shaded to signify that this region of parameter space for

the high-density EoS is excluded by the observation of a star with mass $2\,M_\odot$ [8]. For high-density EoSes with $c^2_{\rm QM} = 1$ (right hand plots), this region is not too large, and leaves a good range of transition pressures and energy density discontinuities that are compatible with the observation. However, for high-density matter with $c^2_{\rm QM} = 1/3$ (left hand plots), which is the typical value in many models (See Sec. 2.1), the $M_{\rm max} > 2\,M_\odot$ constraint eliminates a large region of the CSS parameter space [101, 102]. We discuss this in more detail below.

The upper plots in Fig. 4.1 are for a stiffer nuclear matter EoS, Dirac-Brueckner-Hartree-Fock (DBHF)[103], and the lower plots are for a softer nuclear matter EoS, Brueckner-Hartree-Fock (BHF) [104]. Properties of these nuclear matter EoSes are given in table 4.1. As one would expect, the stiffer EoS gives rise to heavier (and larger) stars, and therefore allows a wider range of CSS parameters to be compatible with the $2\,M_\odot$ measurement.

In Fig. 4.1 the dot-dashed (red) contours are for hybrid stars on a connected branch, while the dashed (blue) contours are for disconnected branches. As discussed in Sec. 3.3, when crossing the near-horizontal boundary from region C to B the connected hybrid branch splits into a smaller connected branch and a disconnected branch, so the maximum mass of the connected branch smoothly becomes the maximum mass of the disconnected branch. Therefore the red contour in the C region smoothly becomes a blue contour in the B and D regions. When crossing the near-vertical boundary from region C to B a new disconnected branch forms, so the connected branch (red dot-dashed) contour crosses this boundary smoothly.

In each panel of Fig. 4.1, the physically relevant allowed region is the white unshaded region. If, as predicted by many models, $c^2_{\rm QM} \lesssim 1/3$, then the existence of a $2\,M_\odot$ star constrains the other CSS parameters to two regions of parameter space (unshaded regions on the left and right sides of the two left panels of Fig. 4.1). In the left-hand region the transition occurs at a fairly low density $n_{\rm trans} \lesssim 2n_0$. The region B, where connected and disconnected

hybrid star branches can coexist, is excluded for $c^2_{\rm QM} \leqslant 1/3$, and even for larger $c^2_{\rm QM}$ it is only allowed if the nuclear matter EoS is sufficiently stiff. In the right-hand allowed region the transition pressure is high, and the connected branch (red dot-dashed) contours are, except at very low $\Delta\varepsilon$, almost vertical, corresponding to EoSes that give rise to a very small connected hybrid branch which exists in a very small range of central pressures $p_{\rm cent}$ just above $p_{\rm trans}$. The maximum mass on this branch is therefore very close to the mass of the purely-hadronic matter star with $p_{\rm cent} = p_{\rm trans}$. The mass of such a purely hadronic star is naturally independent of parameters that only affect the quark matter EoS, such as $\Delta\varepsilon$ and $c^2_{\rm QM}$, so the contour is vertical. These hybrid stars have a tiny core of the high density phase and cover a tiny range of masses, of order $10^{-3}\,M_\odot$ or less, and so would be very rare.

4.2.2 Minimum radius of hybrid stars

In Fig. 4.2 we show contour plots of the radius of the maximum-mass star (on either a connected or disconnected hybrid branch) as a function of the CSS quark matter EoS parameters. Since the smallest hybrid star is typically the heaviest one, this allows us to infer the smallest radius that arises from a given EoS.

The layout is as in Fig. 4.1: each panel shows dependence on $p_{\rm trans}/\varepsilon_{\rm trans}$ and $\Delta\varepsilon/\varepsilon_{\rm trans}$ for fixed $c^2_{\rm QM}$; the plots on the left are for $c^2_{\rm QM} = 1/3$ and the plots on the right are for $c^2_{\rm QM} = 1$; the plots on the top are for the stiffer DBHF nuclear matter EoS, while the lower plots are for the softer BHF nuclear matter EoS. As in Fig. 4.1, the region that is eliminated by the observation of a $2\,M_\odot$ star is shaded in grey.

The smallest stars, with radii as small as 9 km, occur when the high-density phase has the largest possible speed of sound $c^2_{\rm QM} = 1$. They are disconnected branch stars arising from

EoSes having a low transition pressure ($n_{\rm trans} \lesssim 2n_0$) with a fairly large energy density discontinuity ($\Delta\varepsilon/\varepsilon_{\rm trans} \gtrsim 1$).

As in Fig. 4.1, the contours in the high-transition-pressure region are almost vertical because the hybrid branch is then a very short extension to the nuclear mass-radius relation, and its radius is close to that of the heaviest purely hadronic star, which is independent of $\Delta\varepsilon/\varepsilon_{\rm trans}$ and $c^2_{\rm QM}$. The radius of the hybrid stars decreases with $p_{\rm trans}$ in this region, because the radius of hadronic stars decreases with central pressure.

For $c^2_{\rm QM} = 1/3$, the allowed low-transition-pressure region is disconnected from the high-transition pressure region and is so small that it is hard to see on this plot. By magnifying it (left hand plots of Fig. 4.4) we see that in this region the radius contours closely track the border of the allowed region (the $M_{\rm max} = 2\,M_\odot$ line) so we can say that the radius must be greater than 11.5 km almost independent of the transition pressure and hadronic EoS. For a stiff hadronic EoS this minimum is raised to 11.7 km. These values are comparable to the minimum mass of about 11.8 km found in Ref. [102], which explored a larger set of hadronic EoSes but did not explore the full CSS parameter space for the high-density EoS. If a star with radius smaller than this minimum value were to be observed, we would have to conclude that $c^2_{\rm QM}$ is greater than 1/3. In the magnified figure we also show how the excluded region would grow if a $2.1\,M_\odot$ star were to be observed (long-dashed line for connected branch stars and short-dashed line for disconnected branch stars). This would increase the minimum radius to about 12.1 km for the soft hadronic EoS and 12.2 km for the stiff hadronic EoS.

4.2.3 Typical radius of hybrid stars

In Fig. 4.3 we show contours (the U-shaped lines) of typical radius of a hybrid star, defined as $R_{1.4}$, the radius of a star of mass $1.4\,M_\odot$, as a function of the CSS quark matter EoS parameters. The contours only fill the part of the CSS parameter space where there are hybrid stars with that mass. The dashed (magenta) lines delimit that region which extends only up to moderate transition pressure.

The overall behavior is that, at fixed $\Delta\varepsilon/\varepsilon_{\rm trans}$, the typical radius is large when the transition density is at its lowest. As the transition density rises the radius of a $1.4\,M_\odot$ star decreases at first, but then increases again. This is related to the previously noted fact [105] that when one fixes the speed of sound of quark matter and increases the bag constant (which increases $p_{\rm trans}/\varepsilon_{\rm trans}$ and also varies $\Delta\varepsilon/\varepsilon_{\rm trans}$ in a correlated way) the resultant family of mass-radius curves all pass through the same small region in the M-R plane: the $M(R)$ curves "rotate" counter-clockwise around this hub (see Fig. 2 of Ref. [105]). In our case we are varying $p_{\rm trans}/\varepsilon_{\rm trans}$ at fixed $\Delta\varepsilon/\varepsilon_{\rm trans}$, so the hub itself also moves. At low transition density the hub is below $1.4\,M_\odot$, so $R_{1.4}$ decreases with $p_{\rm trans}/\varepsilon_{\rm trans}$. At high transition density the hub is at a mass above $1.4\,M_\odot$ so $R_{1.4}$ will increase with $p_{\rm trans}/\varepsilon_{\rm trans}$.

The smallest stars occur for $c^2_{\rm QM} = 1$ (right hand plots), where $R_{1.4} \gtrsim 9.5\,{\rm km}$ at large values of the energy density discontinuity, and the radius rises as the discontinuity is decreased. This is consistent with the absolute lower bound of about 8.5 km [106] for the maximally compact $c^2_{\rm QM} = 1$ star obeying $M_{\rm max} > 2\,M_\odot$.

For $c^2_{\rm QM} = 1/3$ the allowed region at low transition pressure is small, so in the right panels of Fig. 4.4 we show a magnification of this region. We see that in the allowed ($M_{\rm max} > 2\,M_\odot$ and $n_{\rm trans} > n_0$) region there is a minimum radius 12.2 km for the BHF (soft) hadronic EoS, and

about 12.5 km for the DBHF (stiff) hadronic EoS. This minimum is attained at the lowest possible transition density, $n_{\rm trans} \approx n_0$. As the transition density rises to values around $2\,n_0$, the minimum radius rises to 12.5 km (BHF) or 13.3 km (DBHF). This is comparable to the minimum radius of about 13 km found in Ref. [102], which explored a wider range of hadronic EoSes but assumed $n_{\rm trans} = 2n_0$. These results are consistent with the lower bound on $R_{1.4}$ for $c^2_{\rm QM} = 1/3$ of about 11 km established in Ref. [106] (Fig. 5) using the EoS that yields maximally compact stars (corresponding to CSS with $p_{\rm trans} = 0$ and $c^2_{\rm QM} = 1/3$) obeying $M_{\rm max} > 2\,M_\odot$.

The dashed line shows how the excluded region would grow if a star of mass $2.1\,M_\odot$ were to be observed. This would increase the minimum radius to about 12.7 km (BHF) or 13 km (DBHF). If a $1.4\,M_\odot$ star were observed to have radius below the minimum value, one would have to conclude, similarly to [102], that $c^2_{\rm QM} > 1/3$.

4.2.4 Maximum mass vs. typical radius

Following Ref. [107], in Fig. 4.5 we characterize each CSS EoS by the maximum mass $M_{\rm max}$ and the radius $R_{1.4}$ of a $1.4\,M_\odot$ star on its mass-radius relation. We can then see which areas of the $R_{1.4}$-$M_{\rm max}$ plane can be populated by hybrid stars arising from typical nuclear EoS combined with the CSS family of quark matter EoSes. Along each curve the transition density is fixed and we vary $\Delta\varepsilon/\varepsilon_{\rm trans}$.

Each of the monotonic curves in Fig. 4.5 represents a family of CSS EoSes with fixed transition density, and varying $\Delta\varepsilon/\varepsilon_{\rm trans}$. As we increase $\Delta\varepsilon/\varepsilon_{\rm trans}$, the maximum mass on a connected branch (solid curve) decreases until it smoothly becomes the maximum mass on a disconnected branch (dashed curve) at the long-dashed (green) line, which corresponds to

the nearly-horizontal phase boundary between region B and region C in the phase diagram Fig. 3.3. For higher transition densities the whole curve is dashed, because in that case any mass-radius curve that includes a $1.4\,M_\odot$ hybrid star will always have its heaviest star on the disconnected branch.

The thin vertical (red) line is where the transition pressure has risen so high that it is equal to the central pressure of a nuclear matter star with a mass of $1.4\,M_\odot$ (at $n_{\rm trans} = 2.365\,n_0$). Note that at higher transition pressures, although on the connected branch hybrid stars are always above $1.4\,M_\odot$, a $1.4\,M_\odot$ hybrid star on the disconnected branch can still exist (see contours in upper panels of Fig. 4.5, where the whole curve is dashed for $n_{\rm trans} > 2.365\,n_0$).

On the lower panels we show contours for EoSes that can give hybrid stars on both connected branch (solid curves on the right) and disconnected branch (dashed curves on the left), at transition densities very close to but below the central density of a nuclear matter star with a mass of $1.4\,M_\odot$ ($n_{\rm trans} < 2.365\,n_0$). From these plots we can see that with the same maximum mass, radii for $1.4\,M_\odot$ hybrid stars on connected/disconnected branches can differ by from 0.1 to 0.4 km.

Each plot in Fig. 4.5 contains a black horizontal line at $M_{\rm max} = 2\,M_\odot$, so all EoSes that lie below that line are observationally ruled out. If $c^2_{\rm QM} \lesssim 1/3$ (see left plots), the range of radii for $1.4\,M_\odot$ hybrid stars is limited to the vicinity of the purely-hadronic star with mass $1.4\,M_\odot$. This is another way of illustrating the lower limit $R > 12.5\,$km found in Sec. 4.2.3 for the DBHF nuclear EoS. If $c^2_{\rm QM} = 1$ (right hand plots) the range of possible radii is somewhat bigger, $R > 9.5\,$km, compatible with the radius value tracking along the $M_{\rm max} = 2\,M_\odot$ boundary in Fig. 4.3, upper-right panel.

4.3 Quark Matter via the Field Correlator Method

4.3.1 The FCM EoS

The approach based on the Field Correlator Method (FCM) provides a natural treatment of the dynamics of confinement in terms of the Color Electric (D^E and D_1^E) and Color Magnetic (D^H and D_1^H) Gaussian correlators, the former being directly related to confinement, so that its vanishing above the critical temperature implies deconfinement [108]. The extension of the FCM to finite temperature T at chemical potential $\mu_q = 0$ gives analytical results in reasonable agreement with lattice data, giving us some confidence that it correctly describes the deconfinement phase transition [109, 110]. In order to derive an EoS of the quark-gluon matter in the range of baryon density typical of the neutron star interiors, we have to extend the FCM to non-zero chemical potential [109, 110]. In this case, the quark pressure for a single flavor is simply given by

$$P_q/T^4 = \frac{1}{\pi^2}\left[\phi_\nu\left(\frac{\mu_q - V_1/2}{T}\right) + \phi_\nu\left(-\frac{\mu_q + V_1/2}{T}\right)\right] \tag{4.1}$$

where

$$\phi_\nu(a) = \int_0^\infty du\left(u^4/\sqrt{u^2+\nu^2}\right)\left(\exp\left[\sqrt{u^2+\nu^2} - a\right] + 1\right)^{-1} \tag{4.2}$$

with $\nu = m_q/T$, and V_1 is the large distance static $\bar{q}q$ potential whose value at zero chemical potential and temperature is $V_1(T = \mu_B = 0) = 0.8$ to $0.9\,\mathrm{GeV}$ [111, 112]. The gluon contribution to the pressure is

$$P_g/T^4 = \frac{8}{3\pi^2}\int_0^\infty d\chi\chi^3\frac{1}{\exp\left(\chi + \frac{9V_1}{8T}\right) - 1} \tag{4.3}$$

and the total pressure is

$$P_{qg} = \sum_{j=u,d,s} P_q^j + P_g - \frac{(11 - \frac{2}{3}N_f)}{32}\frac{G_2}{2} \tag{4.4}$$

where P_q^j and P_g are given in Eq. (4.1) and (4.3), and N_f is the number of flavors. The last term in Eq. (4.4) corresponds to the difference of the vacuum energy density in the two phases, G_2 being the gluon condensate whose numerical value, determined by the QCD sum rules at zero temperature and chemical potential, is known with large uncertainty, $G_2 = 0.012 \pm 0.006$ GeV^4. At finite temperature and vanishing baryon density, a comparison with the recent available lattice calculations provides clear indications about the specific values of these two parameters, and in particular their values at the critical temperature T_c. Some lattice simulations suggest no dependence of V_1 on μ_B, at least for very small μ_B, while different analyses suggest a linear decreasing of G_2 with the baryon density ρ_B [113], in nuclear matter. However, for simplicity, in the following we treat both V_1 and G_2 as numerical parameters with no dependence on μ_B.

4.3.2 The FCM EoS and the CSS parameterization

The CSS parameterization will be applicable to the FCM EoS if the speed of sound in the FCM EoS depends only weakly on the density or pressure. In Fig. 4.6 we show that this is indeed the case. The upper panel shows the speed of sound vs. pressure in the FCM quark matter EoS for different values of the FCM parameters, displayed in the lower panel. We see that the speed of sound varies by less than 5% over the considered range of pressures along each curve, and lies in the interval $0.28 < c^2_{\rm QM} < 1/3$. The value of $c^2_{\rm QM}$ shows a weak dependence on V_1 and extremely weak on G_2, which appears as an additive constant in the

quark matter EoS according to Eq. (4.4). The transition pressure is more sensitive to the FCM parameters, increasing rapidly with V_1 and with G_2. The energy density at a given pressure increases slightly with an increase in V_1 or G_2.

To illustrate how well the CSS parameterization fits the FCM EoS, we show in the lower panel of Fig. 4.6 that, for the same FCM parameter choices, we can always find suitable values of the CSS parameters which fit the FCM calculation extremely well. This means that there exists a well-defined mapping between the FCM parameters (V_1, G_2) and the CSS parameters ($p_{\rm trans}/\varepsilon_{\rm trans}$, $\Delta\varepsilon/\varepsilon_{\rm trans}$, $c^2_{\rm QM}$). Note that the mapping depends on the EoS of the hadronic matter.

The mapping is displayed in Fig. 4.7, which shows the region of the CSS parameter space where FCM equations of state are found. As in the phase diagrams in Sec. 4.2, we show the plane whose co-ordinates are the CSS parameters $\Delta\varepsilon/\varepsilon_{\rm trans}$ and $p_{\rm trans}/\varepsilon_{\rm trans}$. For the hadronic EoS we use BHF (left panel) and DBHF (right panel). The lines without points represent the phase boundaries, as for the figures in Sec. 4.2, for connected and disconnected branches. Whether a given FCM EoS yields stable hybrid stars depends on which of those phase regions it is in. The solid (green) phase boundary with a cusp at $p_{\rm trans}/\varepsilon_{\rm trans} \approx 0.17$ delimits the region with a disconnected branch for $c^2_{\rm QM} = 1/3$, while the nearby dashed (green) line is for $c^2_{\rm QM} = 0.28$, so these span the range of $c^2_{\rm QM}$ relevant for the FCM, as discussed in Fig. 4.6. It is evident that the dependence on $c^2_{\rm QM}$ is tiny and negligible for practical purposes.

The thin dashed (black) line and the solid (black) line studded with circles delimit the equations of state yielded by the FCM calculation. Within that region, the lines studded with points show the CSS parameterization of the FCM quark matter EoS, where along each line we keep V_1 constant and vary G_2. Above that region, V_1 would be negative which would

correspond to a repulsive quark-quark interaction, and in any case could not give $2\,M_\odot$ stars (Fig. 4.8). Below that region, there would be no transition from hadronic to quark matter, as explained below.

In Fig. 4.7, V_1 varies from 0 up to the maximum value at which hybrid star configurations occur, which is indicated by an (orange) cross. For the BHF case that value is $V_1 = 240$ MeV, $G_2 = 0.0024$ GeV^4 and for the DBHF case it is $V_1 = 255$ MeV, $G_2 = 0.0019$ GeV^4. Along each FCM curve in Fig. 4.7 the parameter G_2 starts at the minimum value at which there is a phase transition from hadronic to FCM quark matter; at lower G_2 the quark and the hadronic pressures $p(\mu)$ do not cross at any μ. On each curve one point is labelled with its value of $G_2/(10^{-3}\,\mathrm{GeV}^4)$, and subsequent points are at intervals where G_2 increases in increments of 1 in the same units.

We observe that along each line of constant V_1, $p_{\rm trans}/\varepsilon_{\rm trans}$ grows with G_2. This can be explained by recalling the linear dependence of the quark pressure on G_2 in Eq. (4.4), so that, at fixed chemical potential, an increase of G_2 lowers the quark pressure, making quark matter less favorable, and shifting the transition point to higher chemical potential or pressure. This was already discussed in Ref. [114] for BHF nuclear matter, and is equally applicable to DBHF nuclear matter. Obviously if G_2 becomes too small, the phase transition takes place in a region of low densities where finite nuclei are present, and the homogeneous nuclear matter approach becomes invalid.

The qualitative behavior of the curves of constant V_1 can be understood in terms of the Maxwell construction between the purely hadronic phase and the quark phase. The fact that $\Delta\epsilon/\varepsilon_{\rm trans}$ goes through a minimum (which is always at $p_{\rm trans}/\varepsilon_{\rm trans} \approx 0.1$) as G_2 is increased at constant V_1 can be understood from Fig. 2 of Ref. [114], which shows pressure p as a function of baryon density n and the location of the hadron (BHF EoS) to quark

(FCM EoS) transition when G_2 is varied. The hadronic EoS is strongly curved, especially at low pressure, while the FCM EoS is closer to a straight line. Consequently, the baryon density difference between the two phases at a given pressure has a minimum at densities around $2\,n_0$, which corresponds to $p_{\rm trans}/\varepsilon_{\rm trans} \approx 0.1$. As G_2 increases, the transition pressure rises, scanning through this minimum. It follows that the energy density difference also goes through a minimum, because $\epsilon = \mu n - p$, and p and μ are continuous at the transition, so $\Delta\varepsilon = \mu\Delta n$. The DBHF hadronic EoS is very similar to BHF at low pressure, so the curves have their minima at the same value of $p_{\rm trans}/\varepsilon_{\rm trans}$ in both panels of Fig. 4.7.

We also see in Fig. 4.7 that an increase of V_1 moves the curves slightly downward and to the right. This is expected since V_1 is a measure of the attractive interparticle strength, and therefore it is inversely proportional to the pressure of the system, so the pressure decreases as V_1 is increased at fixed μ, and, as already discussed for the parameter G_2, a decrease of the quark pressure raises $p_{\rm trans}$. The role of V_1 and G_2 in the quark EoS discussed so far, provides in the same way a qualitative understanding of $c^2_{\rm QM}$ in panel (a) in Fig.4.6, although, as already noticed, the effect in Fig. 4.7 of the change in $c^2_{\rm QM}$ is negligible.

4.3.3 Expected properties of mass-radius curves

By comparing Fig. 4.7 with Fig. 3.3 we can see that when combining FCM quark matter with BHF (soft) nuclear matter, the physically allowed range of FCM parameter values yields EoSes that are mostly in regions C and A, where there is no disconnected hybrid branch. At the lowest transition densities the FCM EoS can achieve a large enough energy density discontinuity to yield a disconnected branch (region D).

For the DBHF (stiff) nuclear EoS there is a wider range of values of V_1 and G_2 that give disconnected branches, and some of them give simultaneous connected and disconnected branches. This difference can be understood in terms of the stiffness of the EoSes. A change from a soft hadronic EoS (BHF) to a stiff one (DBHF) produces a steeper growth of the hadronic pressure as a function of the baryon density. Referring again to Fig. 2 of Ref. [114], this pulls the DBHF $p(n)$ curve further away from the FCM curve, giving a larger difference in baryon density at given pressure, and hence, as noted above, a larger $\Delta\varepsilon$. This is why the curves for DBHF+FCM (right panel of Fig. 4.7) are shifted upwards along the $\Delta\varepsilon/\varepsilon_{\rm trans}$ axis compared to the BHF+FCM curves (left panel of Fig. 4.7).

We can calculate the maximum mass of a hybrid star containing an FCM core as a function of the FCM parameters, and then use the mapping described above to obtain the CSS parameter values for each FCM EoS, producing a contour plot of maximum mass (Fig. 4.8) for BHF (left panel) and DBHF (right panel) hadronic EoS. Given that the CSS parameterization is a fairly accurate representation of the FCM EoS, one would expect this to be very similar to the corresponding plot for CSS itself with $c^2_{\rm QM} = 1/3$ (Fig. 4.1), and this is indeed the case. The contours in Fig. 4.8 are restricted to the region corresponding to physically allowed FCM parameter values, so they end at the edges of that region.

The triangular shaded area at the edge of each panel shows the region of the parameter space that is accessible by the FCM and is consistent with the measurement of a $2\,M_\odot$, by having hybrid stars of maximum mass greater than $2\,M_\odot$. The (orange) cross in each panel of Fig. 4.7 is at the high-transition-pressure corner of that triangular area. The heaviest BHF+FCM hybrid star has a mass of $2.03\,M_\odot$, and the heaviest DBHF+FCM hybrid star has a mass of $2.31\,M_\odot$.

As noted in Sec. 4.2.1, the hybrid stars in this physically allowed and FCM-compatible region of the phase diagram lie on a very tiny connected branch, covering a very small range of central pressures and masses and radii, and would therefore occur only rarely in nature. These stars have very small quark matter cores (similarly see Figs.3.5 and 3.6), and their mass and radius are very similar to those of the heaviest purely hadronic star, but there could be other clear signatures of the presence of the quark matter core, such as different cooling behavior.

The CSS parameterization has another region where heavy hybrid stars occur, at low transition pressure (see Fig. 4.1), but the FCM does not predict that the quark matter EoS could be in that region.

To characterize the radius of FCM hybrid stars we cannot construct contour plots like Fig. 4.3 because, as we have just seen, the FCM predicts that only hybrid stars with mass very close to the maximum mass are allowed. There are no FCM hybrid stars with mass around $1.4\,M_\odot$. Instead, in Fig. 4.9 we show the range of radii of stars with a given maximum mass when varying FCM parameters, for our two different hadronic EoSes. The right hand edge of each shaded region traces out the mass-radius relation for hadronic stars with the corresponding hadronic EoS. The FCM hybrid stars form very small connected branches which connects to the nuclear matter where the central pressure reaches the transition pressure (See Sec. 4.2.1), so the hybrid stars do not deviate very far from the hadronic mass-radius curve. Hence the shaded regions in Fig. 4.9 are narrow, especially in the observationally allowed ($M_{\rm max} > 2\,M_\odot$) region, which perfectly matches the prediction of CSS parametrization on the maximum-mass star radius in the high transition-pressure region (see left panels of Fig. 4.2). For BHF (soft) nuclear matter, the hadronic stars, and hence the hybrid stars, are smaller because the nuclear mantle is more compressed by the self-gravitation of the star.

4.4 Conclusions

In this chapter we have shown how observational constraints on the mass and radius of hybrid stars can be expressed in a reasonably generic model-independent way as constraints on the parameters of the CSS parameterization of the high-density EoS. Our analysis assumed a sharp transition from nuclear matter to a high-density phase such as quark matter, and that the speed of sound in that phase is independent of the pressure. We found that the observation of a $2\,M_\odot$ star constrains the CSS parameters significantly. If, as predicted by many models, $c^2_{\rm QM} \lesssim 1/3$, then there are two possible scenarios.

Firstly, there is a low-transition-pressure scenario, where the transition to the high density phase occurs at $n_{\rm trans} \lesssim 2n_0$ (unshaded region on the left side of the two left panels of Figs. 4.1, 4.2, 4.3). In this scenario, the hybrid branch of the mass-radius relation will be connected to the nuclear branch if the energy density discontinuity at the transition is less than about 50%, otherwise it will be a separate "third family" or "twin star" disconnected branch. In the $c^2_{\rm QM} \lesssim 1/3$ and low-transition-pressure scenario there are strong constraints on the radius of the star, as shown in Fig. 4.4. The radius of the maximum mass star (which is typically the smallest possible star) must be greater than about 11.5 km, and the radius of a $1.4\,M_\odot$ star must be greater than about 12.2 km [106]. For a stiffer hadronic EoS, these minima are raised by about 0.15 to 0.3 km. If a neutron star of mass $2.1\,M_\odot$ were observed then this constraint would tighten, increasing the minimum radius to about 12.1 km. If a star smaller than the minimum radius were observed, we would have to conclude that $c^2_{\rm QM} > 1/3$. Conversely, if theoretical considerations established that $c^2_{\rm QM}$ is smaller than 1/3, the minimum radius would become larger [102].

Secondly, there is a high-transition-pressure scenario (white region on the right side of the left panels of Figs. 4.1, 4.2, 4.3). This tends to give a very small branch of hybrid stars with tiny quark matter cores, occuring in a narrow range of central pressures just above the transition pressure. This is why the mass and radius contours become almost vertical in this region: the hybrid star has almost the same mass and radius as the heaviest purely hadronic star (the one where the central pressure is $p_{\rm trans}$), and so the properties of these hybrid stars depend on the hadronic EoS (see Fig. 4.9).

If $c^2_{\rm QM}$ is larger than 1/3 then a larger region of the CSS parameter space becomes allowed. The right panels of Figs. 4.1, 4.2, 4.3 show the extreme case where $c^2_{\rm QM} = 1$. In this case the minimum possible radius is 9.0 km.

Our study is intended to motivate the use of the CSS parameterization as a framework in which the implications of observations of neutron stars for the high-density EoS can be expressed and discussed in a way that is reasonably model-independent [115, 116].

As an application to a specific model, we performed calculations for the FCM quark matter EoS. We showed that the FCM equation of state can be accurately represented by the CSS parameterization, and we displayed the mapping between the FCM and CSS parameters. We found that FCM quark matter has a speed of sound in a narrow range around $c^2_{\rm QM} = 0.3$, and the FCM family of EoSes covers a limited region of the space of all possible EoSes (Fig. 4.7). Once the observational constraint $M_{\rm max} > 2\,M_\odot$ is taken into account, the allowed region in the parameter space is drastically reduced to the shaded areas of Fig. 4.8. This corresponds to the high-transition-pressure scenario, with a small connected branch of hybrid stars with tiny quark matter cores. Such stars would be hard to distinguish from hadronic stars via mass and radius measurements, but the quark matter core could be detectable via other signatures, such as cooling behavior.

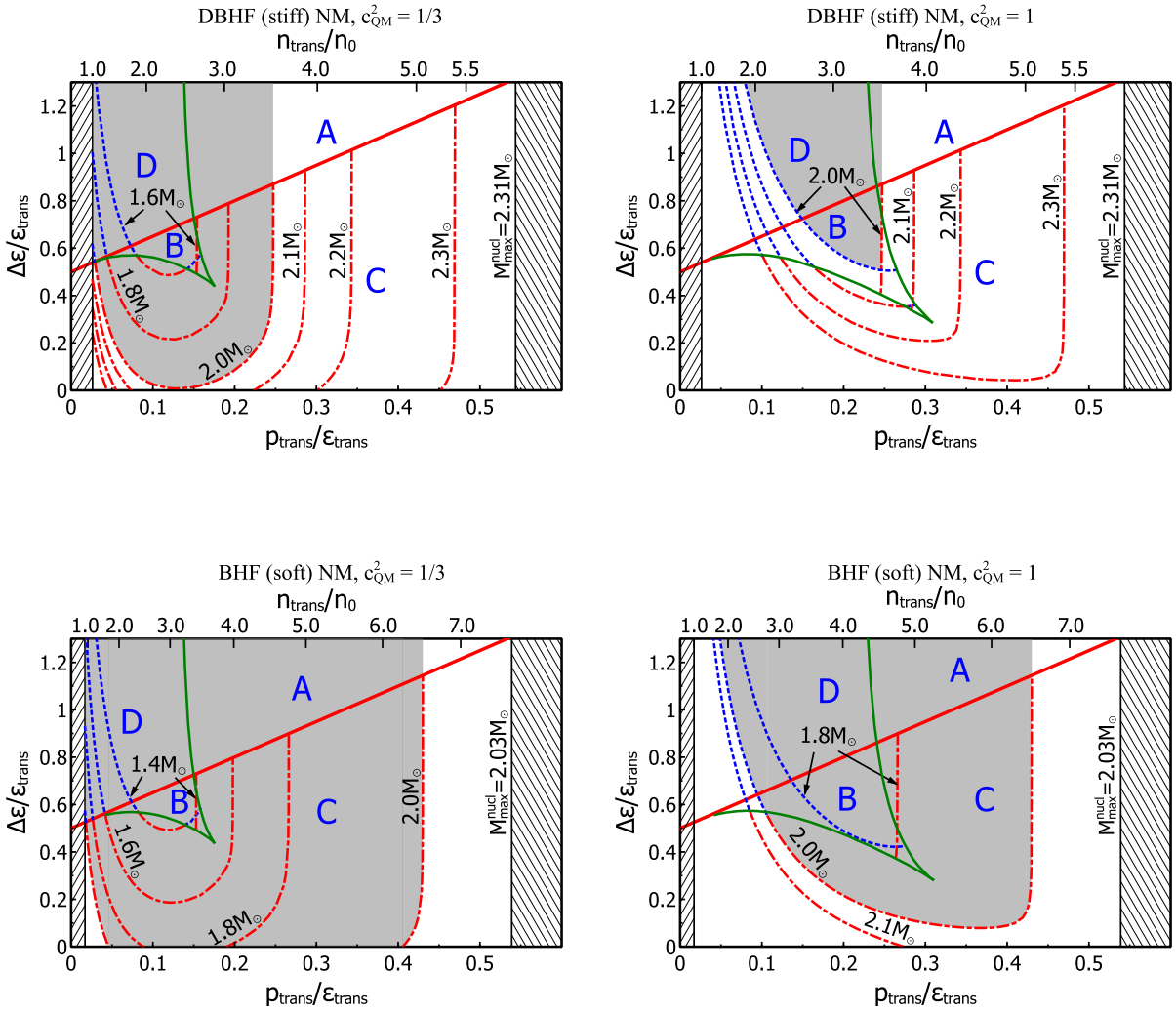

Figure 4.1: Contour plots showing the maximum hybrid star mass as a function of the CSS parameters of the high-density EoS. Each panel shows the dependence on the CSS parameters $p_{\rm trans}/\varepsilon_{\rm trans}$ and $\Delta\varepsilon/\varepsilon_{\rm trans}$. The left plots are for $c^2_{\rm QM} = 1/3$, and the right plots are for $c^2_{\rm QM} = 1$. The top row is for a DHBF (stiff) nuclear matter EoS, and the bottom row is for a BHF (soft) nuclear matter EoS. The grey shaded region is excluded by the measurement of a $2\,M_\odot$ star. The hatched band at low density (where $n_{\rm trans} < n_0$) is excluded because bulk nuclear matter would be metastable. The hatched band at high density is excluded beause the transition pressure is above the central pressure of the heaviest stable hadronic star.

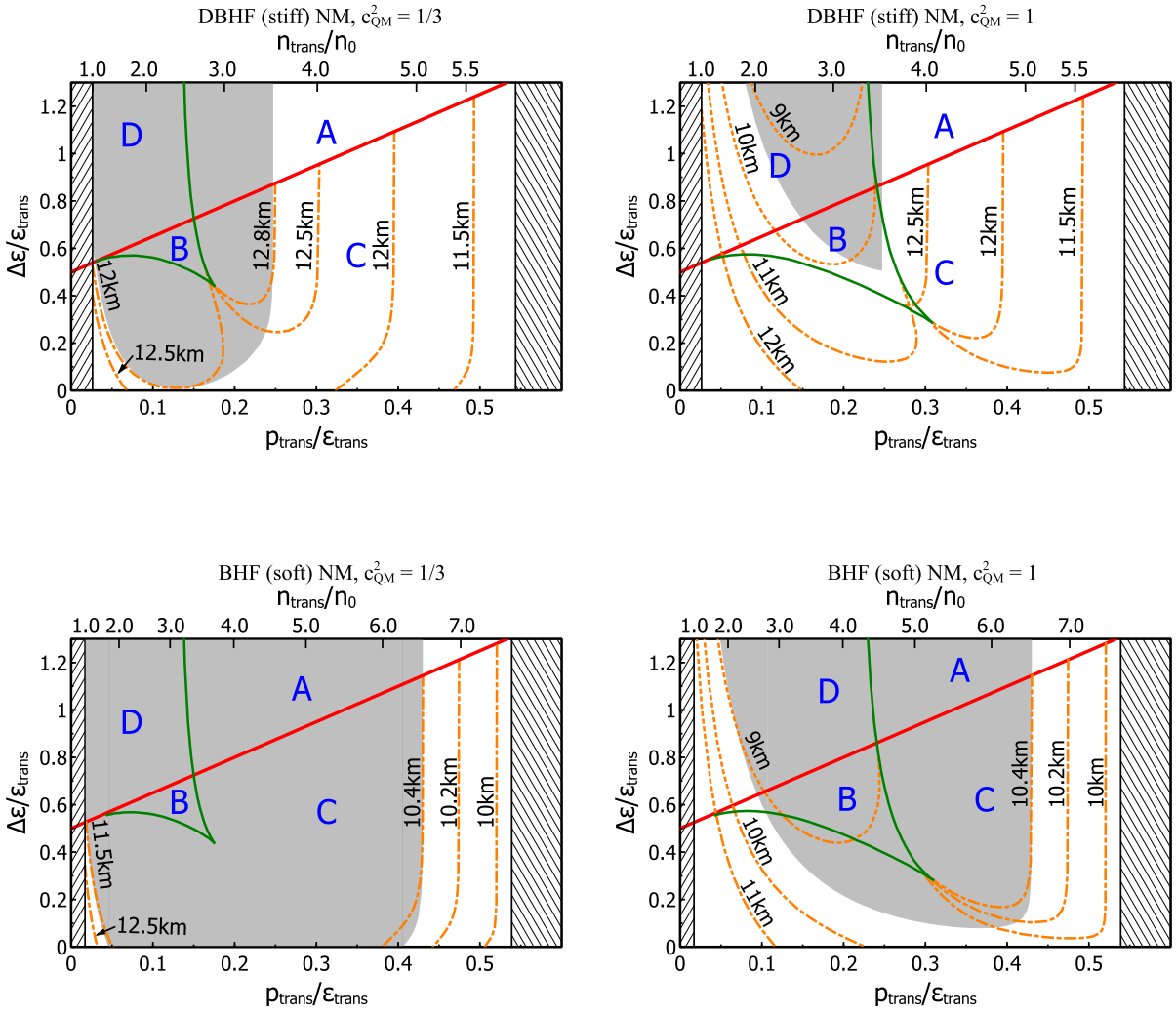

Figure 4.2: Contour plots showing the radius of the maximum-mass star as a function of the CSS parameters. Dashed lines are for the case where this star is on the disconnected branch; for dot-dashed lines it is on the connected branch. The grey shaded region is excluded by the measurement of a $2\,M_\odot$ star. The hatched band at low density (where $n_{\rm trans} < n_0$) is excluded because bulk nuclear matter would be metastable. The hatched band at high density is excluded beause the transition pressure is above the central pressure of the heaviest stable hadronic star. For a magnified version of the low-transition-pressure region for $c^2_{\rm QM} = 1/3$, see Fig. 4.4.

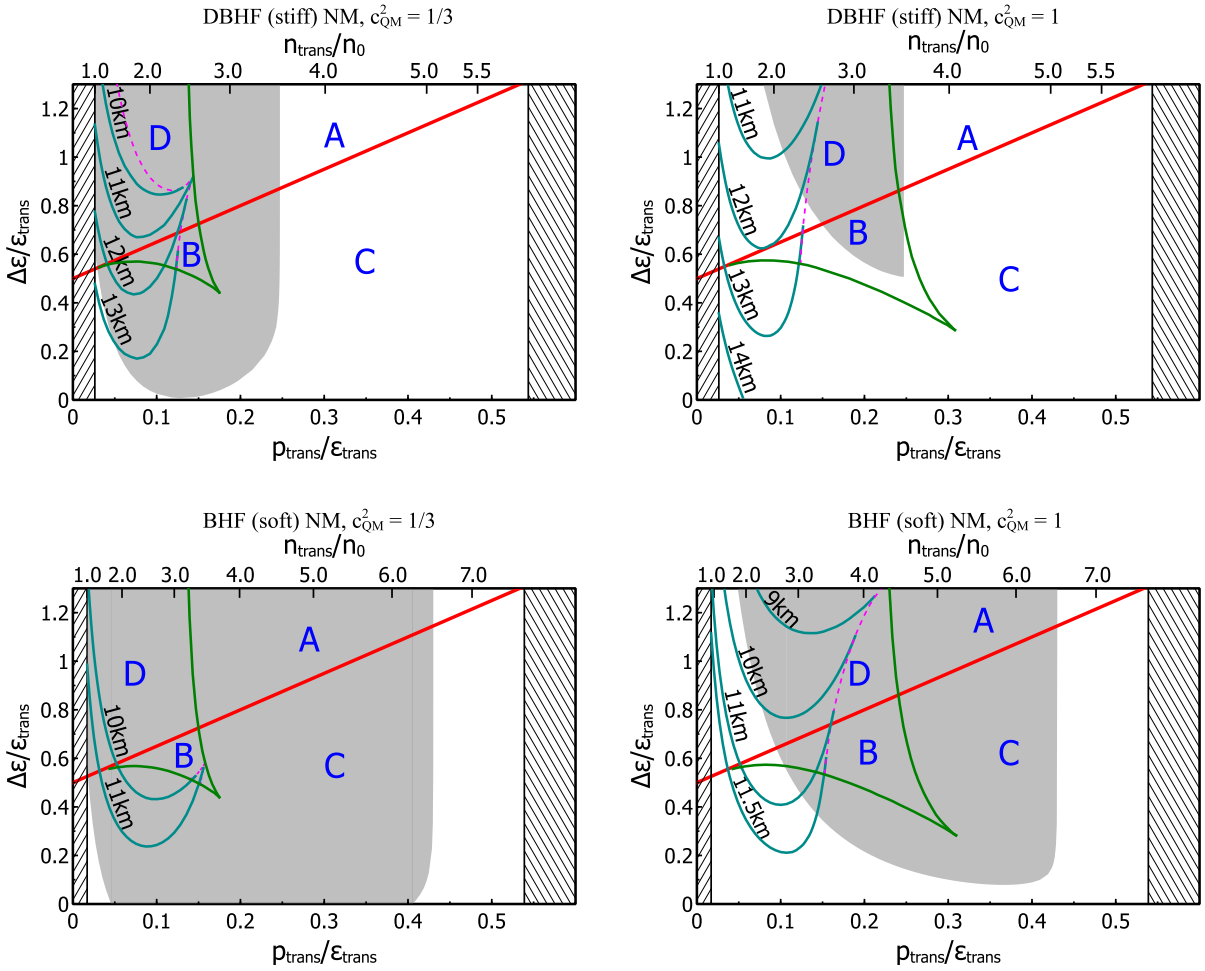

Figure 4.3: Contour plots similar to Fig. 4.2 showing the radius at of a hybrid star of mass $M = 1.4\,M_\odot$ as a function of the CSS parameters. Such stars only exist in a limited region of the space of EoSes (delimited by dashed (magenta) lines). The grey shaded region is excluded by the observational constraint $M_{\max} > 2\,M_\odot$. For a magnified version of the low-transition-pressure region for $c^2_{\rm QM} = 1/3$, see Fig. 4.4.

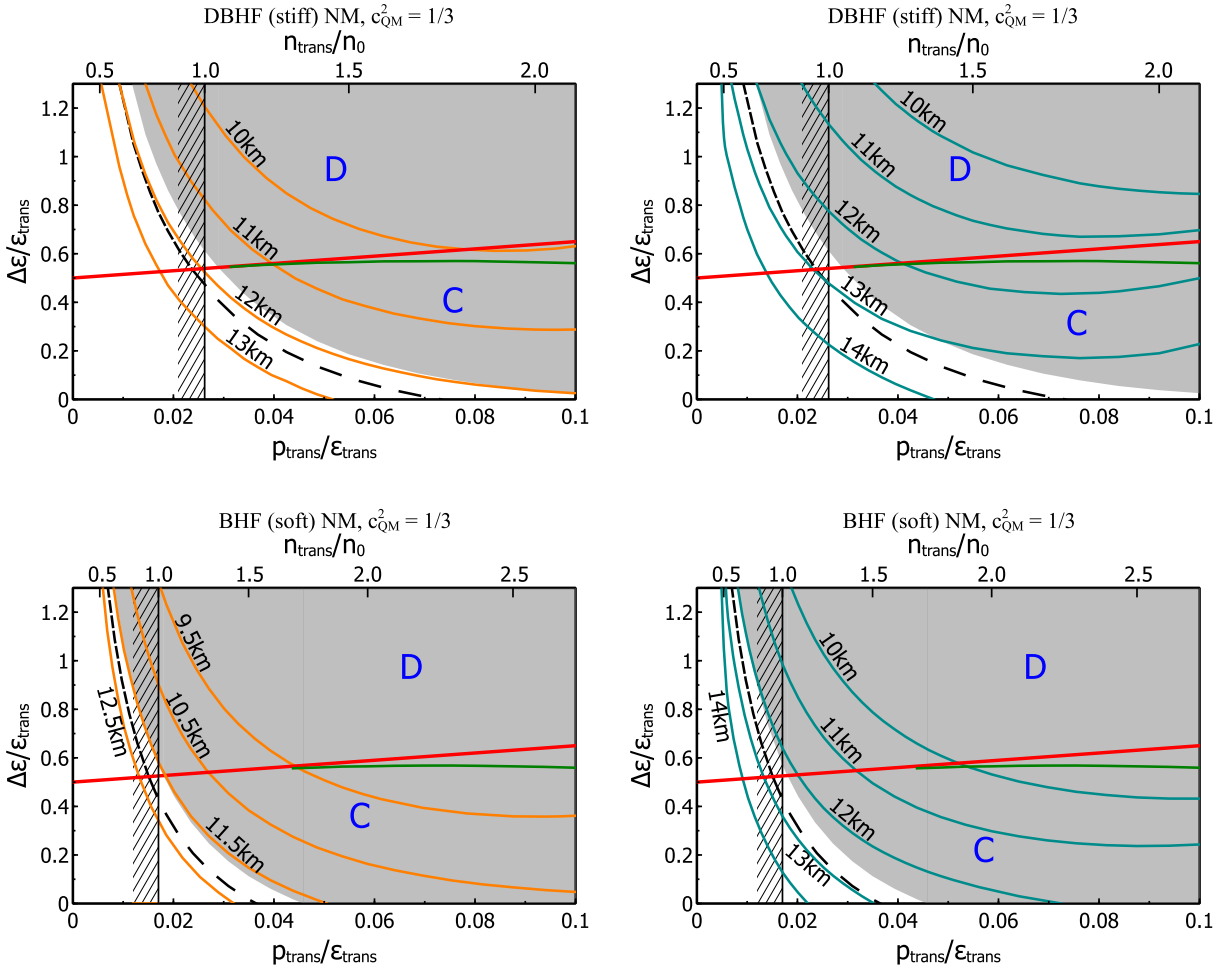

Figure 4.4: Magnified version of the $c^2_{\rm QM} = 1/3$ plots in Figs. 4.2 and 4.3. In the two left panels, the contours are for the radius of the maximum mass star, which is typically the smallest star for the given EoS. In the two right panels, the contours are for $R_{1.4}$, the radius of a $1.4\,M_\odot$ star. The region under and to the left of the hatched bar is probably unphysical because $n_{\rm trans} < n_0$, and it was excluded (hatched band) in earlier figures. The grey shaded region is excluded by the observational constraint $M_{\rm max} > 2\,M_\odot$. The dashed line shows how that region would grow if a $2.1\,M_\odot$ star were observed.

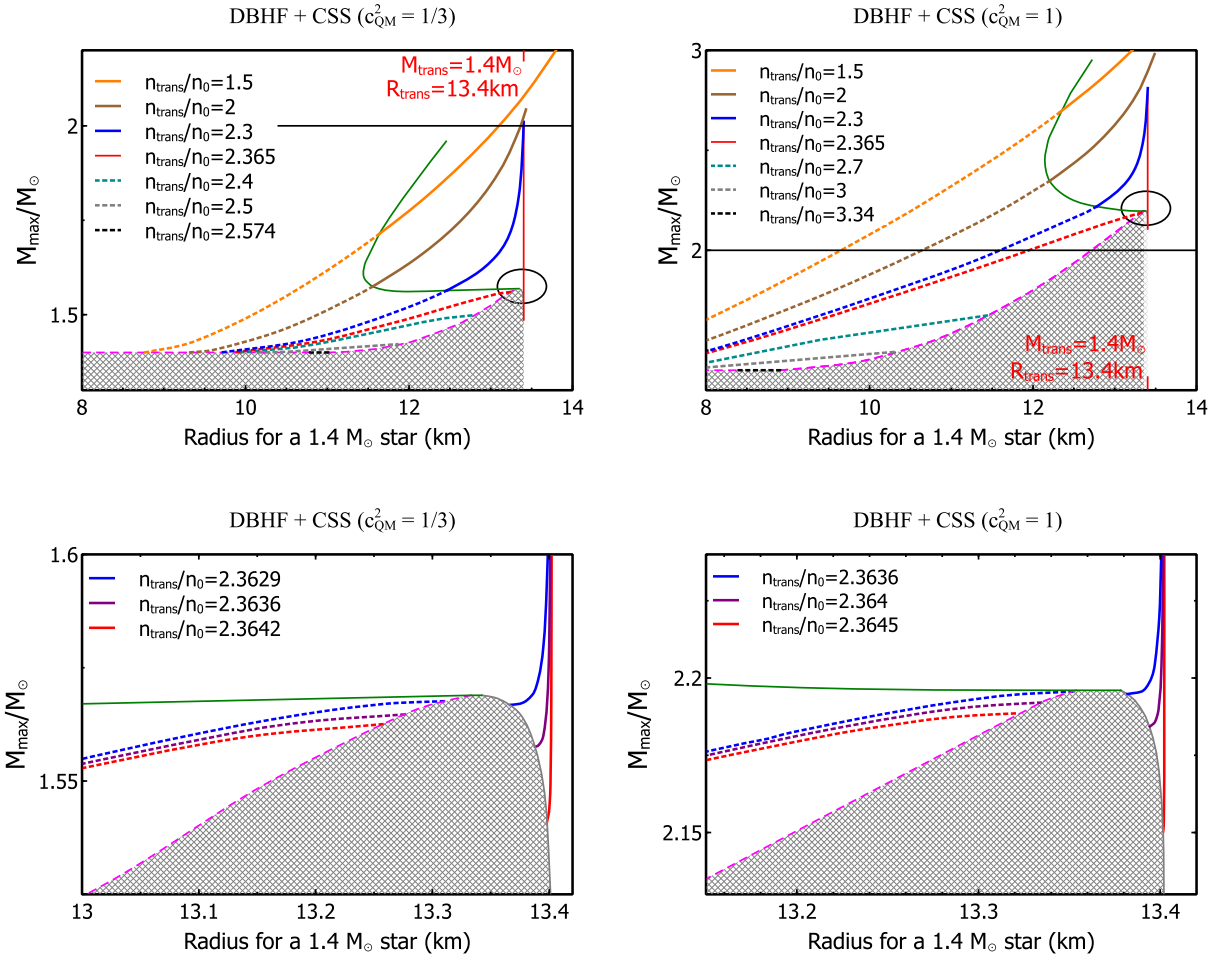

Figure 4.5: Contour plots showing how the maximum hybrid star mass and the radius for a $1.4\,M_\odot$ star vary when two of the CSS parameters, the transition density and energy density discontinuity, are varied. Shaded regions indicate where no $1.4\,M_\odot$ hybrid star exists. In the upper panels, EoSes below the horizontal lines (i.e. those with $M_{\max} < 2\,M_\odot$) are ruled out by observation, and the vertical (red) lines mark the radius for a $1.4\,M_\odot$ purely-hadronic star. Lower panels are zoomed in on the encircled region in the upper panels, where EoSes can give a $1.4\,M_\odot$ hybrid star on both connected branch (solid curves on the right) and disconnected branch (dashed curves on the left).

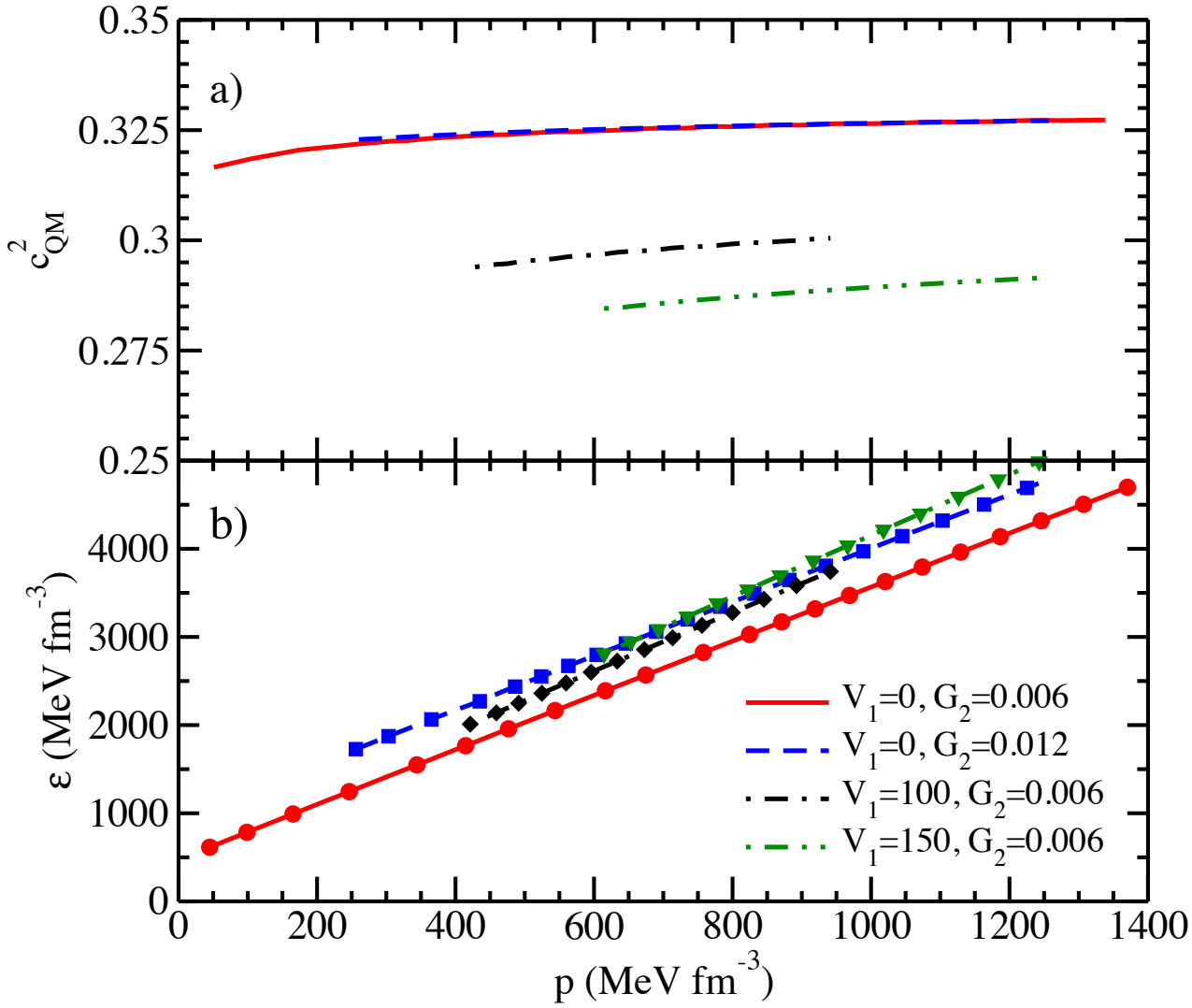

Figure 4.6: The speed of sound $c^2_{\rm QM}$ (panel (a)) is displayed vs. quark matter pressure for several values of V_1 (in MeV) and G_2 (in GeV^4). In panel (b), the FCM energy density is represented by full symbols, whereas the full lines denote the CSS parameterization given by Eq. (3.1).

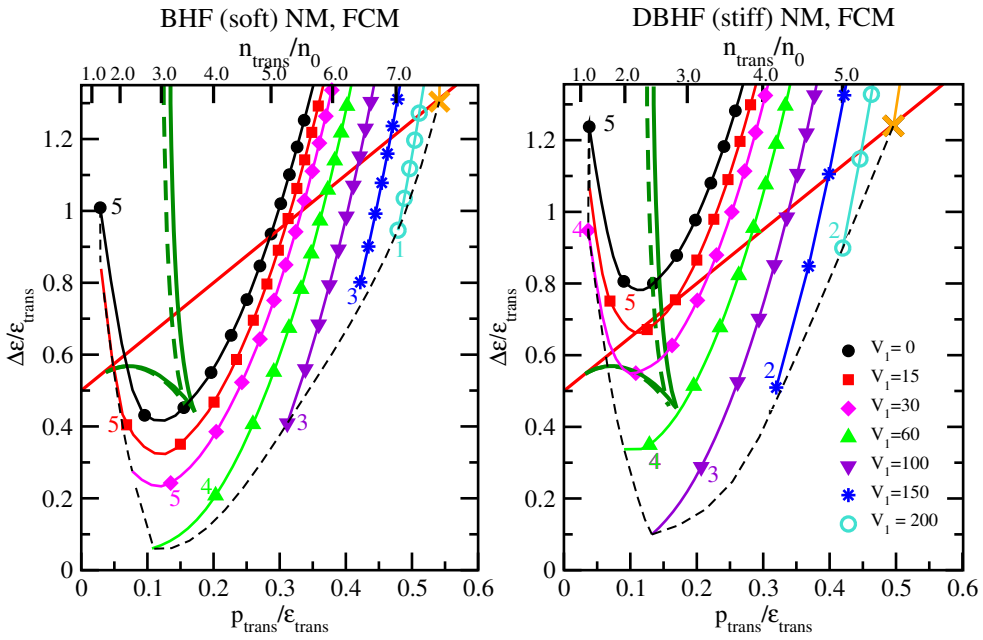

Figure 4.7: The mapping of the FCM quark matter model onto the CSS parameterization. Results are obtained using the BHF (left panel) and DBHF (right panel) nuclear matter EoS. The undecorated curves are the phase boundaries for the occurrence of connected and disconnected hybrid branches (compare Fig. 3.3 and 4.1). The thin dashed (black) line and the solid (black) line studded with circles delimit the region yielded by the FCM model. Within that region, lines decorated with symbols give CSS parameter values for FCM quark matter as G_2 is varied at constant V_1 (given in MeV). The (orange) cross denotes the EoS with the highest $p_{\rm trans}$, which gives the heaviest FCM hybrid star. See text for details.

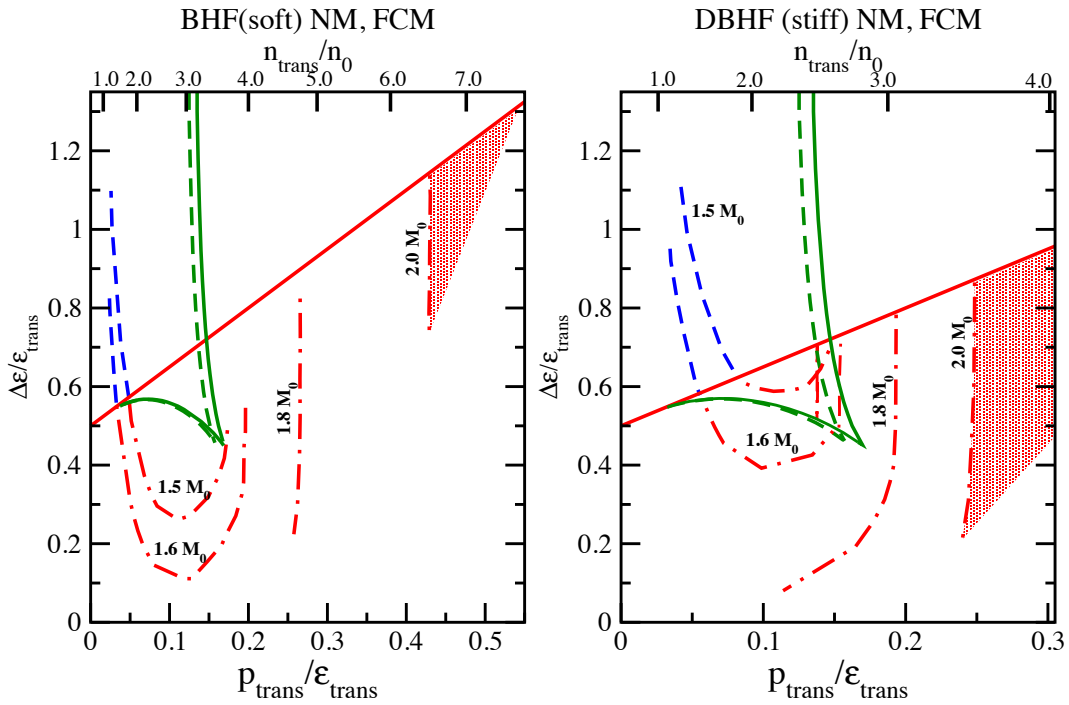

Figure 4.8: Contour plots, analogous to Fig. 4.1, showing the maximum mass of hybrid stars with FCM quark matter cores, given in terms of the corresponding CSS parameter values rather than the original FCM parameter values. As in Fig. 4.7, solid lines are phase boundaries (compare Figs. 3.3 and 4.1). The shaded sectors indicate the parameter regions accessible by the FCM and with $M_{\rm max} > 2\,M_\odot$. In each panel the lower border of the shaded region meets the phase boundary (red line) at the point with highest value of V_1 reported in Fig. 4.7 as an orange cross. Note the different scales on the x-axis for the two panels.

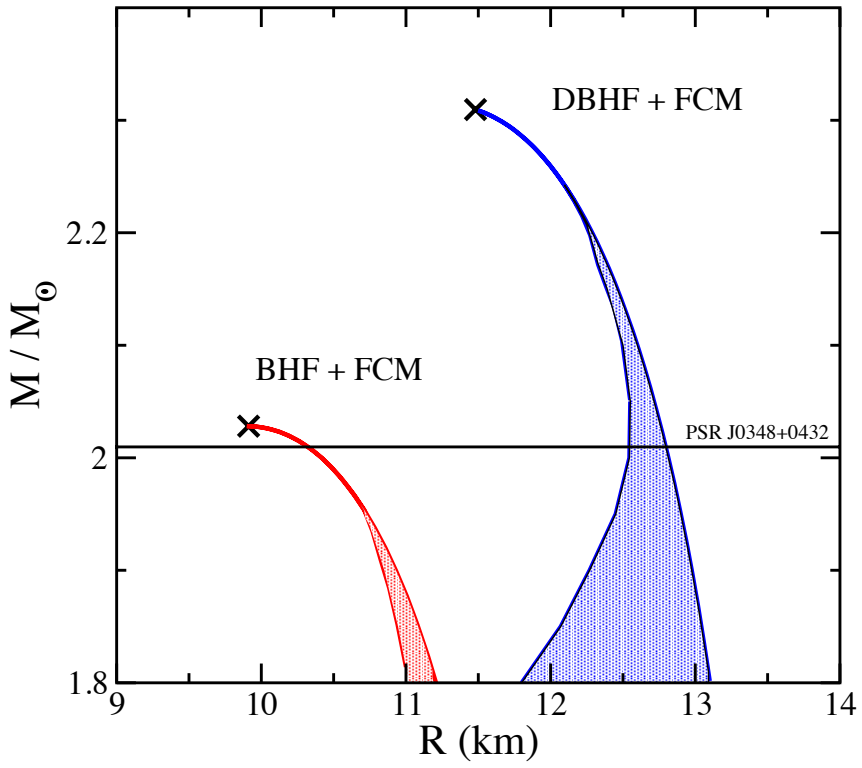

Figure 4.9: Shaded areas show range of radii of stars with a given maximum mass when varying FCM parameters. The thick dashed lines indicate the purely hadronic mass-radius configurations. The crosses at the top of the shaded regions correspond to the maximal configuration indicated by the same symbol in Fig. 4.7. The observational constraint [8] on the star mass is indicated by a horizontal line.

Chapter 5

Phase conversion dissipation in multicomponent compact stars

5.1 Introduction

Unstable global oscillation modes [27] are of particular interest since they arise spontaneously and grow until stopped by some saturation (nonlinear damping) mechanism. For neutron stars, the most important example is r-modes [20, 4] since they are unstable in typical millisecond pulsars unless sufficient damping is present. Several mechanisms for the saturation of the growth of unstable r-modes have been proposed [117, 118, 119, 120, 121, 122]. Although bulk viscosity has a nonlinear "suprathermal" regime [123, 124, 125], it has been found that this becomes relevant only at very high amplitudes, and is probably pre-empted by some other stronger mechanism [120].

The damping of mechanical oscillations of compact stars is a promising signature of the phases of dense matter in their interior. The damping of density perturbations, described locally by the bulk viscosity, is particularly important since it has been shown to vary greatly

between different phases [126, 127, 123, 128, 129, 130, 131, 132, 133, 134, 135, 136, 137, 138]. In addition to the damping properties of bulk phases, the boundary between different phases can also be relevant for dissipation. A well-known example is Ekman layer damping due to shear forces at the boundary between a fluid and a solid phase [139]. In this chapter we propose a dissipation mechanism that stems from the fact that pressure oscillations can cause the interface between two phases to move back and forth, as the two phases are periodically converted into each other. If the finite rate of this conversion produces a phase lag between the pressure oscillation and the position of the interface, energy will be dissipated in each cycle. We study the resultant damping for the case of a hybrid star with a sharp interface between the quark core and the hadronic mantle, the same stellar configuration as discussed in Chaps. 3 and 4, where the dissipation is due to quark-hadron burning at the interface. However, the mechanism is generic and could be relevant for any star with an internal interface between phases of different energy density.

In Sec. 5.2 we study a one-dimensional, simplified model describing two phases in a cylinder separated by a sharp boundary moving in response to external oscillation in the context of Newtonian gravity, and give the expression of the corresponding energy dissipation as a function of the boundary velocity. In Sec. 5.3 we continue to apply the simple model result to the more realistic case of r-mode oscillations in multicomponent stars, concerning the periodically moving phase boundary gives rise to dissipation due to a phase lag between the external pressure oscillation and the local response. In Sec. 5.4 we investigate the specific case of a hadron-quark interface, analyze the underlying interconversion process and give results of r-mode saturation amplitude, both numeric and analytic approximation, as well as its range of validity. Finally the conclusions are given in Sec. 5.5 .

5.2 Schematic Model for the Dissipation Due to Phase Transformation

5.2.1 Two phases in a cylinder

As a step towards an analysis of the dissipation due to phase conversion in an inhomogeneous multi-component star, we now construct a simplified version of the interface between different layers in a gravitationally bound system. We calculate the energy dissipated in this system when it is subjected to periodic compression and rarefaction.

Our toy system involves two incompressible phases, characterized by different densities of a conserved particle species. We assume there is a first-order pressure-induced phase transition, so the phases are separated by a sharp interface ("the phase boundary") which, in long-term equilibrium, is at the critical pressure $p_{\rm crit}$, and that there are processes that can convert each phase into the other at some finite rate. We consider a cylinder containing both phases in a homogeneous (Newtonian) gravitational field, with a piston which can be moved parallel to the direction of the field (Fig. 5.1). The high-density phase is deeper in the gravitational potential than the low-density phase. The field produces a pressure gradient in the cylinder, which can be shifted by moving the piston. This will cause the equilibrium position of the interface to shift, but, crucially, depending on the speed of the conversion process, it may take some time for the interface to move to its new equilibrium position. This causes the response of the system (its volume or density) to lag behind the externally applied force, resulting in dissipation. To calculate the energy dissipated per cycle, we simply calculate the net $p\,\mathrm{d}V$ work done by the piston in one cycle.

We assume that the equation of state of the two phases is linear,

$$p(\mu) = \begin{cases} \mu\, n_{\mathrm{L}} - \varepsilon_{\mathrm{L}} & \text{(low density phase)} \\ \mu\, n_{\mathrm{H}} - \varepsilon_{\mathrm{H}} & \text{(high density phase)} \end{cases} , \tag{5.1}$$

where μ is the chemical potential for the conserved particle number, and the two incompressible phases have fixed particle number densities n_{L} and n_{H}, and fixed energy densities ε_{L} and ε_{H}. Later we use the fact that this is a valid approximation for any equation of state, as long as the pressure oscillations are small enough.

In a Newtonian gravitational field the pressure is a function of x determined by

$$\frac{dp}{dx} = -g\,\varepsilon \ , \tag{5.2}$$

where g is the gravitational acceleration, assumed to be independent of x. Eq. (5.2) has a simple solution where the pressure varies linearly with x, with a fixed gradient $g\,\varepsilon$ in each phase (see Fig. 5.2)

$$p(x) = \begin{cases} p_{\mathrm{b}} - g\varepsilon_{\mathrm{H}}(x - x_{\mathrm{b}}) & x < x_{\mathrm{b}} \\ p_{\mathrm{b}} - g\varepsilon_{\mathrm{L}}(x - x_{\mathrm{b}}) & x \geqslant x_{\mathrm{b}} \end{cases} , \tag{5.3}$$

where x_{b} is the position of the interface between the two phases ("the boundary") and p_{b} is the pressure at the boundary. In long-term equilibrium, the boundary settles at its "ideal" position, where p_{b} is p_{crit} (see below).

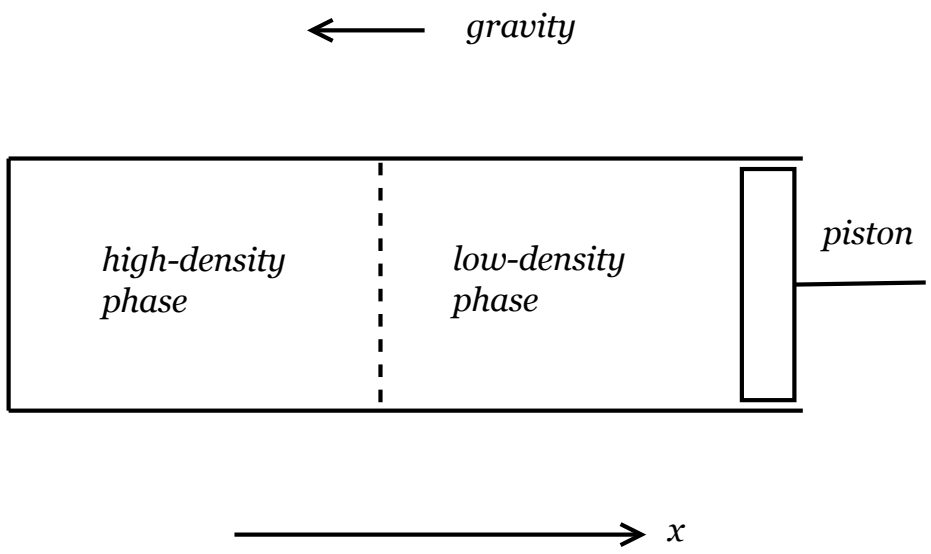

Figure 5.1: Toy model: two incompressible phases in a cylinder with piston, in a gravitational field. An oscillation of the external pressure on the piston leads to interconversion of the two phases, and hence movement of the piston.

5.2.2 External pressure oscillation

Assume that the external pressure on the piston varies periodically. When the pressure is high, part of the low-density phase is driven to a pressure above p_{crit} and starts to convert into the high density phase, and vice versa during rarefaction. The pressure at any given

location and the position of the phase boundary therefore vary in time

$$p(x,t) = \bar{p}(x) + \delta p(x,t) \,, \tag{5.4}$$

$$x_{\rm b}(t) = \bar{x}_{\rm b} + \delta x_{\rm b}(t) \,, \tag{5.5}$$

where $\bar{x}_{\rm b}$ is the equilibrium position of the boundary and $\bar{p}(x)$ is the pressure profile in long-term equilibrium. The position of the boundary at a given moment depends on the previous compression history and the phase conversion rate, and we expect that, because of the finite rate of conversion between the two phases, the oscillation of the boundary can be out of phase with the oscillation of the pressure, and this will lead to dissipation via net $p\,{\rm d}V$ work being done in each cycle.

To calculate the dissipation, we need to relate the movement of the boundary to the applied pressure oscillation. We assume that the pressure in the low density phase oscillates harmonically with amplitude $\Delta p_{\rm L}$ and frequency ω, so $\delta p_{\rm L}(t) = \Delta p_{\rm L} \sin(\omega t)$.

In equilibrium, the piston is at $\bar{x}_{\rm p}$ with pressure $\bar{p}_{\rm p}$. As part of the pressure oscillation the piston moves

$$x_{\rm p}(t) = \bar{x}_{\rm p} + \delta x_{\rm p}(t) \,, \tag{5.6}$$

and the pressure at the piston is

$$p_{\rm p}(t) = \bar{p}_{\rm p} - g\varepsilon_{\rm L}\delta x_{\rm p}(t) + \Delta p_{\rm L} \sin(\omega t) \tag{5.7}$$

The movement of the piston and the movement of the phase boundary are connected by particle number conservation inside the cylinder. The total particle number is $N_{\rm tot} =$

$(x_{\rm b}(t)n_{\rm H} + (x_{\rm p}(t) - x_{\rm b}(t))n_{\rm L})\,S$ where S is the cross sectional area. Particle number conservation $\delta N_{\rm tot} = 0$ gives

$$x_{\rm p}(t) = \bar{x}_{\rm p} + \left(1 - \frac{n_{\rm H}}{n_{\rm L}}\right)\delta x_{\rm b}(t)\ . \tag{5.8}$$

We can now express the $p\,{\rm d}V$ work done by the piston in one cycle in terms of the movement of the boundary $\delta x_{\rm b}$ induced by the pressure oscillation. In later sections we will study how the boundary moves, expressing it as a function of the speed of the phase conversion process. First, however, we define a useful concept, the "ideal boundary".

5.2.3 Ideal position of the phase boundary

In discussing the motion of the boundary it is convenient to define an "ideal position" of the boundary, $x_{\rm ib}$. Since we are assuming that an external force imposes a specified time-dependence of the pressure in the low-density phase, it is natural to define the ideal boundary at time t to be the position the boundary would reach if we held $\delta p_{\rm L}$ fixed at its current value and waited for phase conversion processes to equilibrate. Thus $x_{\rm ib}(t)$ is the solution of $p_{\rm L}(x_{\rm ib}, t) = p_{\rm crit}$. Unlike the actual boundary, the ideal boundary is determined simply by the instantaneous value of the applied pressure, with no dependence on previous history or conversion rate. The position of the ideal boundary therefore oscillates in phase with the pressure,

$$\delta x_{\rm ib}(t) = \Delta x_{\rm ib}\sin(\omega t)\ ,\ \Delta x_{\rm ib} = \frac{\Delta p_{\rm L}}{g\varepsilon_{\rm L}} \tag{5.9}$$

and its velocity is 90° out of phase with its position

$$v_{\rm ib}(t) = v_{\rm ib}^{\rm max}\cos(\omega t)\ ,\ v_{\rm ib}^{\rm max} = \omega\Delta x_{\rm ib} = \frac{\omega\Delta p_{\rm L}}{g\varepsilon_{\rm L}}\ . \tag{5.10}$$

For a harmonic pressure oscillation in the low-density phase the ideal boundary moves harmonically. Note however, that because of the discontinuity in energy density on the phase boundary, the pressure oscillation cannot be simultaneously harmonic in both phases. It is also worth noting that according to our definition $x_{\rm ib}(t)$ is not in general the place in the cylinder where the pressure at time t is $p_{\rm crit}$: these locations only coincide if the real phase boundary occurs where the pressure is above $p_{\rm crit}$.

5.2.4 Energy dissipation in one cycle

The net $p\,\mathrm{d}V$ work done by the piston in one cycle ($0 \leqslant t < \tau$, $\tau = 2\pi/\omega$) is

$$W = -S \int_0^\tau p_{\rm p}(t) \frac{\mathrm{d}x_{\rm p}(t)}{\mathrm{d}t}\,\mathrm{d}t \tag{5.11}$$

where $p_{\rm p}$ is the pressure at the location of the piston, which is determined by the applied oscillation of the piston, and $x_{\rm p}$ is the position of the piston. The piston's position depends on the movement of the boundary $\delta x_{\rm b}(t)$ (5.8), so from Eq. (5.11) the energy dissipation in one cycle is

$$\begin{aligned} W &= S\left(\frac{n_{\rm H}}{n_{\rm L}} - 1\right)\left(\int_0^\tau \bar{p}_{\rm p} \frac{\mathrm{d}\delta x_{\rm b}(t)}{\mathrm{d}t}\,\mathrm{d}t \right. \\ &\qquad \left. + \int_0^\tau \Delta p_{\rm L} \sin(\omega t) \frac{\mathrm{d}\delta x_{\rm b}(t)}{\mathrm{d}t}\,\mathrm{d}t\right) \end{aligned} \tag{5.12}$$

The movement of the boundary is constrained by the detailed physics of the conversion process, which determines how fast it can move at any given moment. For quark-hadron conversion we will see that it obeys a differential equation which expresses the fact that the boundary's maximum velocity depends on how far out of equilibrium the boundary is, and whether it needs to move inward or outward to reach equilibrium. In effect, the real

boundary is always chasing the ideal boundary (which is its long run equilibrium position), while the ideal boundary is a moving target, its sinusoidal movement linearly related to the applied pressure oscillation, see Eqs. (5.7) and (5.9).

In Eq. (5.12) we see that the dissipation vanishes if the two phases have equal densities, since then the movement of the phase boundary does not change the volume of the system, so there is no associated $p\,\mathrm{d}V$ work.

To derive the dissipation we assumed that the pressure oscillation in the low density phase is harmonic. Had we instead assumed that the pressure oscillation in the high density phase is harmonic, then the energy dissipation would be slightly bigger, with a difference $\Delta W/W \simeq \Delta\varepsilon/\varepsilon_{\mathrm{L}}$, where $\Delta\varepsilon$ is the energy density discontinuity at the interface.

5.3 R-mode Damping

We can now calculate the damping of a global oscillation mode in a hybrid star resulting from the phase conversion mechanism. A comprehensive analysis of this problem requires the detailed density oscillation of the global mode in a star with multiple components separated by density discontinuities due to first order phase transitions. So far the profiles for global oscillation modes have not been obtained for such a realistic model of a compact star. We therefore estimate the dissipation from a piecewise model for the mode profile, using the known form for a homogeneous star on either side of the phase boundary. We estimate the error due to this simplified procedure below. Although the amplitude of the mode's density and pressure oscillation varies from place to place in the star, the simple model sketched in Sec. 5.2 then applies locally for sufficiently small volume elements containing the

interface between the two phases and the entire range over which it moves in response to the oscillation.

Here we study the case of r-modes because they are unstable and a sufficiently powerful damping mechanism is required to ensure that they saturate at a low enough amplitude so that they do not spin down the fast rotating compact stars that we observe. The energy density fluctuation for an $m=2$ r-mode to leading order in the mode amplitude α is [140]

$$\frac{\delta\varepsilon}{\bar{\varepsilon}} = \sqrt{\frac{8}{189}}\alpha A R^2 \Omega^2 \left(\frac{r}{R}\right)^3 \mathrm{Re}\left[Y_3^2(\theta,\phi)e^{i\omega t}\right] \tag{5.13}$$

where $\delta\varepsilon = \varepsilon - \bar{\varepsilon}$, $Y_3^2(\theta,\phi) = \frac{1}{4}\sqrt{\frac{105}{2\pi}}e^{2i\phi}\sin^2\theta\cos\theta$, and A is the inverse speed of sound squared

$$A \equiv \frac{\partial\varepsilon}{\partial p} \tag{5.14}$$

evaluated at equilibrium. R is the radius of the star, Ω the rotational frequency of the star, and ω is the r-mode frequency $\omega = \frac{2}{3}\Omega$.

The r-mode involves flows that are dominantly angular rather than radial. At any moment there is higher pressure in some regions of solid angle in the star, and lower pressure in other regions. This means that globally the fraction of high or low pressure phase does not change much over time. However, an r-mode will still lead to conversion between the phases, since the low and high pressure regions are kilometers apart, so the gradients of pressure and density in the angular directions are extremely small, and in an oscillation at kHz frequencies there is not enough time for any response other than local movement of the boundary in the radial direction. Therefore particle transformation is required in far-separated areas despite the approximate global conservation of the amount of each of the two forms of matter. The simple cylinder and piston model of Sec. 5.2 is a valid approximation for a

small volume element that straddles the interface between the two phases. To use the results from Sec. 5.2 we simply need to use the appropriate expression for the local gravitational acceleration g. The general relativistic generalization of the Newtonian hydrostatic equation is the Oppenheimer-Volkoff (OV) equation [25] (Eq. 1.1).

5.3.1 Movement of the ideal boundary

We now calculate the dissipation of the energy of an r-mode in a star with a high density core surrounded by a low density mantle. (In the next section we look at the case where the phases are quark matter and hadronic matter.) We are interested in situations where phase conversion dissipation becomes important in r-mode oscillations when their amplitude is still fairly low (we will see in Sec. 5.4.4 that this may indeed happen), so we will assume $\delta p \ll \bar{p}$ in the region near the boundary. Therefore, we only need the EoS in a narrow pressure range around the critical pressure. The EoS can be expanded to linear order analogous to Eq. (5.1) so the pressure oscillation is given by

$$\delta p = \frac{\bar{\varepsilon}}{A}\frac{\delta\varepsilon}{\bar{\varepsilon}}. \tag{5.15}$$

When $\delta\varepsilon > 0$, according to Eq. (5.13)–(5.15) the r-mode pressure oscillation in the low density phase is

$$\delta p_{\rm L}(r,\theta,\phi,t) = \bar{\varepsilon}_{\rm L}(r)C(r)\alpha\sin^2\theta\cos\theta\cos(2\phi+\omega t) \tag{5.16}$$

where

$$C(r) \equiv \sqrt{\frac{105}{756\pi}}\Omega^2\frac{r^3}{R} \tag{5.17}$$

The ideal (i.e. long-run equilibrium at given pressure) position of the boundary $R_{\rm ib}$, analogous to $x_{\rm ib}$ in Sec. 5.2, is determined by the r-mode pressure oscillation in the low-density phase, and therefore depends on the angular co-ordinates. If we write $R_{\rm ib} = \bar{R}_{\rm b} + \delta R_{\rm ib}$, where $\bar{R}_{\rm b}$ is the equilibrium position of the phase boundary with no pressure oscillation, then from (1.1) and (5.16)

$$\delta R_{\rm ib}(t) = \frac{\delta p_{\rm L}}{dp/dr(\bar{R}_{\rm b})} = \frac{\alpha C_{\rm b}}{g_{\rm b}} \sin^2\theta \cos\theta \cos(2\phi + \omega t) \tag{5.18}$$

where

$$\begin{aligned} g_{\rm b} &\equiv g_{\rm eff}(\bar{R}_{\rm b}) \\ C_{\rm b} &\equiv C(\bar{R}_{\rm b}) = \sqrt{\frac{105}{756\pi}}\Omega^2 \frac{\bar{R}_{\rm b}^3}{R}. \end{aligned} \tag{5.19}$$

and $g_{\rm eff}(\bar{R}_{\rm b})$ is the effective gravitational acceleration at $\bar{R}_{\rm b}$ evaluated in the low-density phase.

The oscillation amplitude of the ideal boundary position, as a function of latitude θ in the star, is

$$|\delta R_{\rm ib}| = \frac{C_{\rm b}\alpha}{g_{\rm b}} |\sin^2\theta \cos\theta| \tag{5.20}$$

and the maximum value of the velocity of the ideal boundary $v_{\rm ib}^{\rm max}$ is

$$v_{\rm ib}^{\rm max} = \frac{C_{\rm b}\alpha\omega}{g_{\rm b}} |\sin^2\theta \cos\theta| \tag{5.21}$$

5.3.2 R-mode energy dissipation

We now calculate $\mathrm{d}W(\theta, \phi)$, the energy dissipated during one oscillation cycle in a radially oriented cylinder straddling the phase boundary, with an infinitesimal base area located at a given spherical angle. Integrating this result over solid angle will give the total dissipation

of the r-mode. Using Eqs. (5.12) and (5.18),

$$\mathrm{d}W(\theta,\phi) = \mathrm{d}S\left(\frac{n_{\mathrm{H}}}{n_{\mathrm{L}}} - 1\right)\Delta p_{\mathrm{L}}\int_0^{\tau}\cos(2\phi+\omega t)\frac{\mathrm{d}\delta R_{\mathrm{b}}(t)}{\mathrm{d}t}\mathrm{d}t \tag{5.22}$$

where $\Delta p_{\mathrm{L}} = g_{\mathrm{b}}\varepsilon^{\mathrm{L}}_{\mathrm{crit}}|\delta R_{\mathrm{ib}}|$, and from Eq. (5.20)

$$\Delta p_{\mathrm{L}} = \varepsilon^{\mathrm{L}}_{\mathrm{crit}} C_{\mathrm{b}}\alpha|\sin^2\theta\cos\theta| \tag{5.23}$$

and $\mathrm{d}S = \bar{R}_{\mathrm{b}}^2\sin\theta\mathrm{d}\theta\mathrm{d}\phi$. As discussed earlier, these estimates are based on an approximate r-mode profile. To estimate the uncertainty due to this simplification we compare two idealized cases, where the pressure oscillation is harmonic in the low density phase, and where it is harmonic in the high-density phase. As discussed below Eq. (5.12) the difference for an infinitesimal volume element is of order $\Delta W/W \simeq \Delta\varepsilon/\varepsilon_{\mathrm{L}}$ which directly gives an estimate for the uncertainty of the dissipation in the case of global r-modes. Typical density steps at first order transitions in a compact star are less than a factor of two, but due to the simplified model assumptions we make here our results should anyway be viewed as order of magnitude estimates.

5.4 Hadron-Quark Conversion in a Hybrid Star

The damping mechanism that we have analyzed above is generic, and will operate in any situation where there are two phases with a sharp interface. However, the amount of damping depends crucially on how the interface between the two phases moves via conversion of one phase into the other. To explore a realistic case, we estimate the boundary velocity for an

interface between strange quark matter and nuclear matter in a hybrid star, and obtain an estimate of the resultant r-mode saturation amplitude in this scenario.

There is existing literature, developed in the context of the strange matter hypothesis (that strange quark matter is the true ground state at zero pressure) on the outward-moving burning front that accompanies the transformation of a neutron star into a strange star [141, 142]. Hydrodynamical simulations of the burning process have been performed [143, 144] and possible astrophysical observables (gamma-ray bursts, neutrino emissions and gravitational waves, etc) have been discussed [145, 146]. Our situation is related to this work, but we are interested in conversion of quark matter to nuclear matter as well as nuclear matter to quark matter, since both processes occur as our burning front moves inwards and outwards in response to an oscillation in the pressure.

5.4.1 Pressure and chemical potential at the interface

In equilibrium, both pressure and baryon chemical potential are continuous across the phase boundary between nuclear and quark matter, and their values at the boundary are the critical values at which the phase transition occurs ($p = p_{\rm crit}, \mu_{\rm B} = \mu_{\rm B}^{\rm crit}$). When the system is driven out of equilibrium by global pressure oscillations, the phase boundary may temporarily be at a different pressure because the conversion between nuclear and quark matter has a limited rate. The boundary is then out of chemical equilibrium, and the baryon chemical potential is no longer continuous at the boundary because baryon number cannot flow freely through the boundary. On the timescale of chemical equilibration the pressure is still continuous because it equilibrates at the speed of sound which is of order c. The burning front will move as the phase with higher baryon chemical potential converts into the phase with lower baryon

chemical potential. The situation is illustrated in Fig. 5.3. If the pressure at the boundary is above the critical value ($p_{\rm b} = p_1 > p_{\rm crit}$), the baryon number chemical potential in quark matter is lower ($\mu_1^{\rm Q} < \mu_1^{\rm N}$). Nuclear matter (NM) is then converted into quark matter (QM) and the front moves outwards. If the pressure at the boundary is below the critical value ($p_{\rm b} = p_2 < p_{\rm crit}$) the front moves in the opposite direction converting quark matter back into nuclear matter.

As we will see below, when the boundary is out of chemical equilibrium, and moving to reestablish that equilibrium, it has around it a NM $\rightleftarrows$ QM conversion region, where the matter is out of beta equilibrium.

The chemical equilibration of quark matter can proceed via the nonleptonic channel $u + s \leftrightarrow d + u$ and also the leptonic Urca channel $d \to u + e^- + \bar{\nu}$ and $u + e^- \to d + \nu$. Following Ref. [24], we neglect the Urca channel here for simplicity, but we discuss its potential impact in Sec. 5.5. Nonleptonic beta-equilibration processes are driven by the chemical potential $\mu_{\rm K}$, which couples to the imbalance between strange and down quarks; $\mu_{\rm K}$ is zero in beta equilibrated matter, but not in the conversion region,

$$\begin{aligned} \mu_{\rm K} &\equiv \mu_{\rm d} - \mu_{\rm s} \ , \\ n_{\rm K} &= \tfrac{1}{2}(n_{\rm d} - n_{\rm s}) \ . \end{aligned} \tag{5.24}$$

In the following sections we discuss how $\mu_{\rm K}$ and $\mu_{\rm B}$ vary in the conversion region when the front is moving, in order to estimate the speed of the boundary in two half cycles of oscillation, which determines the energy dissipation over the complete period.

5.4.2 Conversion of nuclear matter into quark matter

To estimate the front speed in the NM $\rightarrow$ QM transition when $p_{\rm b} = p_1 > p_{\rm crit}$, we use the one-dimensional steady-state approximation used by Olinto [24] to analyze the conversion of neutron matter into strange quark matter. This analysis is conveniently performed in the rest frame of the boundary, where the boundary is at $x = 0$, neutron matter is at $x < 0$ and strange quark matter at $x > 0$. The transformation of neutron matter into strange quark matter requires considerable strangeness production, which can only be accomplished by flavor-changing weak interactions. The slow rate of weak interactions means that at the front nuclear matter is converted in to some form of non-beta-equilibrated quark matter (with $\mu_{\rm K} \neq 0$). In the conversion region behind the front there are flavor-changing non-leptonic interactions and strangeness diffusion. The weak interactions create strangeness and allow $\mu_{\rm K}$ to return to zero over a distance scale of order $(D_{\rm Q}\tau_{\rm Q})^{1/2}$ where $\tau_{\rm Q}$ is the timescale of the flavor-changing non-leptonic interactions and $D_{\rm Q}$ is the diffusion constant for flavor. The diffusion of strangeness towards the boundary and downness away from the boundary allows the strange matter at the boundary to have a strangeness fraction different from that of the nuclear matter which is undergoing deconfinement as the front moves.

In general, strangeness gradients could also exist in front of the boundary, as strangeness could diffuse through the boundary, creating (or adding to) hyperons on the nuclear matter side. However, following Ref. [24], we will assume that the front moves fast enough for this effect to be negligible, so $\mu_{\rm K} = 0$ everywhere ahead of the moving front, i.e. at $x < 0$. The conversion region is then limited to $x > 0$, and can be characterized by $\mu_{\rm K}(x)$, or equivalently by the K-fraction parameter $a(x)$ which decreases with increasing strangeness fraction

$$a(x) \equiv \frac{n_{\rm K}(x) - n_{\rm K}^{\rm Q}}{n_{\rm Q}}, \tag{5.25}$$

where $n_{\rm Q}$ is the baryon number density in equilibrated strange quark matter, and the K density is $n_{\rm K}^{\rm Q^\star}$ at $x = 0$ and as $x \to \infty$ it grows asymptotically to the constant value $n_{\rm K}^{\rm Q}$ for equilibrated strange quark matter. From now on for simplicity we always assume that there are equal numbers of up, down and strange quarks in equilibrated quark matter ($n_{\rm K}^{\rm Q} = 0$). In equilibrated nuclear matter there are only up and down quarks (we assumed no hyperons in front of the boundary), so $n_{\rm K} = n_{\rm d}/2 = n_{\rm N}$ for $x < 0$.

The spatial variation of a (Fig. 5.4, right panel) is determined by the steady-state transport equation, written in the rest frame of the boundary,

$$
\begin{aligned}
D_{\rm Q}\, a'' - v_{\rm N\to Q}\, a' - \mathcal{R}_{\rm Q}(a) = 0, \\
\mathcal{R}_{\rm Q}(a) = (\Gamma_{\rm d\to s} - \Gamma_{\rm s\to d})/n_{\rm Q},
\end{aligned}
\tag{5.26}
$$

where $D_{\rm Q}$ is the flavor diffusion coefficient, $v_{\rm N\to Q}$ the front speed and $\mathcal{R}_{\rm Q}(a)$ is the net rate of flavor-changing weak interactions. The boundary conditions are

$$
\begin{aligned}
a(0^-) &= \frac{n_{\rm N}}{n_{\rm Q}} \equiv a_{\rm N}, \qquad && a(x\to\infty) \to 0, \\
a(0^+) &= \frac{n_{\rm K}^{\rm Q^\star}}{n_{\rm Q}} \equiv a_{\rm Q^\star}, \qquad && a'(0^+) = -v_{\rm N\to Q}\left(\frac{a_{\rm N} - a_{\rm Q^\star}}{D_{\rm Q}}\right).
\end{aligned}
\tag{5.27}
$$

To understand the discontinuity in $a(x)$ across the boundary, let us consider how the chemical potentials vary in the conversion region. The left panel of Fig. 5.4 shows a schematic plot in the $(\mu_{\rm B}, \mu_{\rm K})$ plane. The parabolic-looking curve is the quark matter isobar for pressure $p_{\rm b} > p_{\rm crit}$. The square marked "N" is beta-equilibrated ($\mu_{\rm K} = 0$) nuclear matter at the same pressure. The spatial variation in the conversion region, shown in the right panel of Fig. 5.4, can then be mapped on the chemical potential space as follows. At $x < 0$ we have

beta-equilibrated nuclear matter (N). At $x = 0$, where $a(x)$ drops from $a_{\rm N}$ to $a_{\rm Q^\star}$, $\mu_{\rm K}$ jumps to Q*, which is out-of-equilibrium quark matter with non-zero $\mu_{\rm K}$, but at the same pressure as the nuclear matter. Then as we traverse the conversion region (increasing x), $\mu_{\rm K}$ decays to zero, finally arriving at equilibrated quark matter (Q). All of these configurations are at the same pressure, based on the assumption that the thickness of the conversion region is negligible when compared to the radius of the star. The arrows along the $\mu_{\rm K} = 0$ axis show how $\mu_{\rm B}$ varies as one moves larger distances through beta-equilibrated matter on either side of the conversion region, with the pressure rising monotonically. The arrows above the $\mu_{\rm K} = 0$ axis (blue online) show $\mu_{\rm B}$ increasing as we move inwards through nuclear matter until at N ($\mu_{\rm B} = \mu_{\rm B}^{\rm N}$) we reach the phase boundary. After traversing the phase boundary and conversion region as described above, we are at Q, in beta-equilibrated quark matter at lower $\mu_{\rm B}$, and as we move into the quark core, $\mu_{\rm B}$ rises again (arrows below $\mu_{\rm K} = 0$ axis, red online).

Olinto [24] argued that when the phase boundary is in a steady state of motion there is a "pileup" of nuclear matter in front so that nuclear and quark matter have the same density there, and the boundary has the same velocity relative to nuclear matter and quark matter, i.e. the nuclear matter near the boundary is stationary relative to the quark matter. However, we argue that this is not possible in steady state. When the phase boundary moves, part of the star is transformed from lower density nuclear matter to denser quark matter, and hydrostatic equilibrium requires the star to shrink. This means that in the outer parts of the star the nuclear matter must fall inwards under gravity, so it is moving towards the quark matter. If the inward velocity of the nuclear matter went to zero near the phase boundary, this would require that the "pileup" grows with time, which is not a steady state situation. Instead, we argue that the baryon number conservation condition is automatically fulfilled because the weight of the outer region of the star pushes nuclear matter in to the front as fast

as the front can "consume" it. The density of nuclear matter at the boundary is therefore unchanged by the movement of the boundary, and the nuclear matter velocity takes the value that is determined by baryon number conservation. As we saw in Eq. (5.12) this density step at the phase boundary is crucial for phase-conversion dissipation to occur ($a_{\rm N} < 1$).

For a fixed value of $a_{\rm Q^\star}$, there is only one $v_{\rm N\to Q}$ which guarantees a solution to Eq. (5.26) that satisfies the boundary conditions. To find the proper $v_{\rm N\to Q}$, we apply the method in [24], which analogizes Eq. (5.26) to a classical mechanical problem and solves for the correct potential term, transforming the boundary value problem into an initial value problem. Taking into account both subthermal ($\mu_{\rm K} \ll T$) and suprathermal ($\mu_{\rm K} \gg T$) regimes in the weak rate, the analytical approximation for the front speed in the NM $\to$ QM half cycle is

$$v_{\rm N\to Q} \simeq \sqrt{\frac{D_{\rm Q}}{\tau_{\rm Q}} \frac{a_{\rm Q^\star}^4 + 2\eta_{\rm Q} a_{\rm Q^\star}^2}{2a_{\rm N}(a_{\rm N} - a_{\rm Q^\star})}} \tag{5.28}$$

where $D_{\rm Q}$ is the diffusion constant for flavor, $\tau_{\rm Q}$ is the timescale of non-leptonic flavor-changing interactions, and $\eta_{\rm Q}$ gives the ratio of subthermal to suprathermal rates. Eq. (5.28) is a generalization of Eq. (12) in Ref. [24], which is only valid in the suprathermal regime. As we will see later on, $a_{\rm Q^\star}$ is much less than $a_{\rm N}$, therefore Eq. (5.28) becomes

$$v_{\rm N\to Q} \simeq \frac{1}{a_{\rm N}} \sqrt{\frac{D_{\rm Q}}{2\tau_{\rm Q}}} \sqrt{a_{\rm Q^\star}^4 + 2\eta_{\rm Q} a_{\rm Q^\star}^2} \tag{5.29}$$

The full rate for the non-leptonic strangeness-changing process has been computed in [147], yielding

$$\mathcal{R}_{\rm Q}(a) \simeq (a^3 + \eta_{\rm Q} a)/\tau_{\rm Q}, \tag{5.30}$$

$$\eta_{\rm Q} = \frac{9\pi^2 T^2}{\mu_{\rm Q}^2}, \tag{5.31}$$

$$\tau_{\rm Q} = \left(\frac{128}{27\cdot 5\pi^3} G_F^2 \cos^2\theta_c \sin^2\theta_c \mu_{\rm Q}^5\right)^{-1}, \tag{5.32}$$

where G_F is the Fermi constant, θ_c the Cabibbo angle, and therefore $\tau_{\rm Q} \simeq 1.3\times 10^{-9}\,{\rm s}\,(300\,{\rm MeV}/\mu_{\rm Q})^5$; to leading order the diffusion coefficient (see Eqs. (28) and (36) in [148])

$$D_{\rm Q} \simeq \frac{\pi q_D^{2/3}}{24\,\alpha_s^2\,h\,T^{5/3}} \tag{5.33}$$

where $h = \Gamma(\frac{8}{3})\zeta(\frac{5}{3})(2\pi)^{2/3} \simeq 1.81$, $\alpha_s = g^2/4\pi$ is the QCD coupling constant, and the Debye wave number for cold quark matter of three flavors is q_D where $q_D^2 = 3g^2\mu^2/(2\pi^2)$. The temperature dependence $T^{-5/3}$ comes from Landau damping that dominates for $T \ll \mu$ compared to the Debye screened case $D \propto T^{-2}$.

Different values of $a_{\rm Q^\star}$ give different front profiles corresponding to different front velocities. There is an upper limit on $a_{\rm Q^\star}$ which is constrained by the amplitude of external pressure oscillation, and the argument is as follows.

In order for the boundary to move, it must be favorable for neutrons to turn in to quarks at the boundary, so the total chemical potential per unit baryon number must be larger in beta-equilibrated nuclear matter (N in Fig. 5.4) than in out-of-equilibrium quark matter ($\rm Q^\star$)

$$\mu_{\rm B}^{\rm N} > \mu_{\rm B}^{\rm Q^\star} + \frac{n_{\rm K}^{\rm Q^\star}}{n_{\rm Q^\star}} \cdot \mu_{\rm K}^{\rm Q^\star} \tag{5.34}$$

On the isobar for quark matter, we parameterize the pressure at ($\mu_{\rm B}$, $\mu_{\rm K}$) as an expansion near equilibrium (Q)

$$p_{\rm QM}(\mu_{\rm B},\mu_{\rm K}) = p_{\rm Q} + n_{\rm Q}(\mu_{\rm B}-\mu_{\rm B}^{\rm Q}) + n_{\rm K}^{\rm Q}(\mu_{\rm K}-\mu_{\rm K}^{\rm Q}) + \frac{1}{2}\chi_{\rm K}^{\rm Q}(\mu_{\rm K}-\mu_{\rm K}^{\rm Q})^2 + ... \tag{5.35}$$

where $\chi_{\rm K}^{\rm Q} \equiv \partial n_{\rm K}/\partial\mu_{\rm K}$ is the susceptibility with respect to K-ness evaluated at equilibrium (Q). In equilibrated quark matter, $\mu_{\rm K}^{\rm Q} = 0$. Since the whole conversion region is at the same pressure $p_{\rm Q^\star} = p_{\rm Q} = p_{\rm b}$, so solving for $\mu_{\rm B}^{\rm Q^\star}$ we have

$$\mu_{\rm B}^{\rm Q^\star} = \mu_{\rm B}^{\rm Q} - \left(\frac{n_{\rm K}^{\rm Q}}{n_{\rm Q}} - \frac{\chi_{\rm K}^{\rm Q}\mu_{\rm K}^{\rm Q^\star}}{2\,n_{\rm Q}}\right)\cdot\mu_{\rm K}^{\rm Q^\star}. \tag{5.36}$$

Assuming that Q* is close to equilibrium, so that $n_{\rm K}^{\rm Q^\star} \approx n_{\rm K}^{\rm Q}$, $n_{\rm Q^\star} \approx n_{\rm Q}$, Eq. (5.34) becomes

$$\mu_{\rm B}^{\rm N} - \mu_{\rm B}^{\rm Q} > \frac{\chi_{\rm K}^{\rm Q}\left(\mu_{\rm K}^{\rm Q^\star}\right)^2}{2n_{\rm Q}}\ . \tag{5.37}$$

From Eq. (5.27), $a_{\rm Q^\star} = n_{\rm K}^{\rm Q^\star}/n_{\rm Q} \approx \mu_{\rm K}^{\rm Q^\star}\chi_{\rm K}^{\rm Q}/n_{\rm Q}$, then Eq. (5.37) leads to an upper bound on $a_{\rm Q^\star}$

$$a_{\rm Q^\star}^{\rm max} = \sqrt{\frac{2\Delta\mu_{\rm B}\chi_{\rm K}^{\rm Q}}{n_{\rm Q}}}, \tag{5.38}$$

with

$$\Delta\mu_{\rm B} \equiv \mu_{\rm B}^{\rm N} - \mu_{\rm B}^{\rm Q} \simeq (\gamma-1)\delta p/n_{\rm Q}, \tag{5.39}$$

where $\delta p = p_{\rm b} - p_{\rm crit} \geqslant 0$ (Fig. 5.3) and $\gamma \equiv n_{\rm Q}/n_{\rm N} = 1/a_{\rm N}$. Notice that the derivation of Eq. (5.38) is totally general and can also be applied to matter with nonzero $n_{\rm K}$ at equilibrium (see Sec. 5.4.3).

The pressure oscillation is related to how far the real boundary is away from its ideal position via

$$\delta p = g_{\rm b}\varepsilon_{\rm crit}^{\rm N}\big(\delta x_{\rm ib}(t) - \delta x_{\rm b}(t)\big), \tag{5.40}$$

where the ideal position $\delta x_{\rm ib}(t) = \Delta x_{\rm ib}\sin(\omega t)$, and the amplitude $\Delta x_{\rm ib} = \Delta p_{\rm N}/g_{\rm b}\varepsilon_{\rm crit}^{\rm N}$ (see Eq. (5.9)). If we assume that the boundary is always moving at its maximum speed ($a_{\rm Q^\star} \approx a_{\rm Q^\star}^{\rm max}$), then according to Eq. (5.29) and Eq. (5.38)–(5.40) the velocity of the boundary in the NM $\rightarrow$ QM half cycle is determined by

$$\frac{{\rm d}\delta x_{\rm b}}{{\rm d}t} \simeq \frac{1}{a_{\rm N}}\sqrt{\frac{D_{\rm Q}}{2\tau_{\rm Q}}}\sqrt{\left[\delta z/\ell_{\rm Q}\right]^2 + 2\eta_{\rm Q}\delta z/\ell_{\rm Q}} \tag{5.41}$$

where $\delta z \equiv \delta x_{\rm ib} - \delta x_{\rm b}$ is how far the boundary is from its equilibrium position at the current pressure, and $\ell_{\rm Q}$ characterizes its typical length

$$\ell_{\rm Q} = \frac{(n_{\rm Q}/\chi_{\rm K}^{\rm Q})n_{\rm Q}}{2(\gamma-1)g_{\rm b}\varepsilon_{\rm crit}^{\rm N}}. \tag{5.42}$$

5.4.3 Conversion of quark matter into nuclear matter

The conversion from quark matter to nuclear matter has not been analyzed previously because it does not arise if quark matter is absolutely stable. However, it can analogously be described in terms of conversion and diffusion behind the boundary, now on the hadronic side where strangeness is carried by hyperons. There are various hyperons that could be present in dense hadronic matter and correspondingly multiple weak reactions involving these hyperons. For an illustrative calculation we only consider one such process, $n+n \rightarrow p+\Sigma^-$, which is a reasonable choice because Σ^- hyperons are expected to be among the first to appear when nuclear matter is compressed, see e.g. [149]. For simplicity, we also neglect electrons

in the system, which is admittedly not a good approximation, but we are only aiming to provide an illustrative example. In this case

$$\mu_{\rm K} = 2\mu_{\rm n} - \mu_{\rm p} - \mu_{\Sigma} \tag{5.43}$$

$$n_{\rm K} = \frac{1}{6}(2n_{\rm n} - n_{\rm p} - n_{\Sigma}) \ . \tag{5.44}$$

Moving away from the boundary on the hadronic side, into the conversion region, the K density is $n_{\rm K}^{\rm N\star}$ at $x = 0$ and as $x \to -\infty$ it grows asymptotically to the nonzero constant value $n_{\rm K}^{\rm N} \simeq n_{\rm n}/3 \approx n_{\rm N}/3$ for equilibrated nuclear matter with Σ^- hyperons, where $n_{\rm N}$ is the baryon number density in equilibrated nuclear matter. As before we neglect strangeness conversion ahead of the boundary, which is the quark matter region in this case. In equilibrated quark matter we assume there are equal numbers of up, down and strange quarks, so $n_{\rm K} = 0$ for $x > 0$.

As in Sec. 5.4.2 we define a parameter to characterize the deviation of the K fraction from its equilibrium value,

$$b(x) \equiv \frac{n_{\rm K}(x) - n_{\rm K}^{\rm N}}{n_{\rm N}} \tag{5.45}$$

and the steady-state transport equation for $b(x)$ in the rest frame of the boundary is

$$D_{\rm N}\, b'' - v_{\rm Q\twoheadrightarrow N}\, b' - \mathcal{R}_{\rm N}(b) = 0, \tag{5.46}$$

$$\mathcal{R}_{\rm N}(b) = (\Gamma_{\rm n+n\to p+\Sigma^-} - \Gamma_{\rm p+\Sigma^-\to n+n})/n_{\rm N}, \tag{5.47}$$

where $D_{\rm N}$ is the flavor diffusion coefficient, $v_{\rm Q\twoheadrightarrow N}$ is the front speed for the QM $\to$ NM transition and $R_{\rm N}(b)$ the strangeness-changing reaction rate divided by the baryon number

density in nuclear matter. The boundary conditions are

$$\begin{aligned} b(0^-) &= \frac{n_{\rm K}^{\rm N^\star} - n_{\rm K}^{\rm N}}{n_{\rm N}} \equiv b_{\rm N^\star}, \quad b(x \to -\infty) \to 0, \\ b(0^+) &= \frac{-n_{\rm K}^{\rm N}}{n_{\rm N}} \equiv b_{\rm Q}, \qquad\qquad b'(0^-) = v_{\rm Q \to N} \left(\frac{b_{\rm Q} - b_{\rm N^\star}}{D_{\rm N}} \right). \end{aligned} \tag{5.48}$$

The right panel of Fig. 5.5 shows how $b(x)$ varies through the phase boundary and transition region. The left panel of Fig. 5.5 shows schematically the behavior in the $(\mu_{\rm B}, \mu_{\rm K})$ plane. The short curve through N and N* is the nuclear matter isobar for pressure $p_{\rm b} < p_{\rm crit}$. The dot marked "Q" is beta-equilibrated quark matter at the same pressure, which exists (see right panel) at $x = 0^+$. The point N* is out-of-equilibrium nuclear matter which is found just behind the boundary at $x = 0^-$. The point N is beta-equilibrated nuclear matter, which is found at the tailing end of the conversion region. All these forms of matter are at the same pressure as long as thickness of the conversion region is much smaller than the radius of the star. The arrows represent how the chemical composition changes as one moves from the hadronic outer part of the star through the conversion region to the quark core. At the boundary $\mu_{\rm B}^{\rm N} < \mu_{\rm B}^{\rm Q}$ and $\mu_{\rm K}$ in out-of-equilibrium nuclear matter is negative because of the presence of massive hyperons.

Following the same logic as in the previous section, we find the analytic approximation for the velocity of the boundary

$$\begin{aligned} v_{\rm Q \to N} \qquad &\simeq \qquad -\sqrt{\frac{D_{\rm N}}{\tau_{\rm N}} \frac{b_{\rm N^\star}^4 + 2\eta_{\rm N} b_{\rm N^\star}^2}{2 b_{\rm Q}(b_{\rm Q} - b_{\rm N^\star})}} \\ &\xrightarrow{|b_{\rm N^\star}| \ll |b_{\rm Q}|} \quad \frac{1}{b_{\rm Q}} \sqrt{\frac{D_{\rm N}}{2\tau_{\rm N}}} \sqrt{b_{\rm N^\star}^4 + 2\eta_{\rm N} b_{\rm N^\star}^2} \end{aligned} \tag{5.49}$$

where $-b_{\rm Q} \lesssim 1/3$. The full rate for the weak interaction has been computed in [130]

$$\mathcal{R}_{\rm N}(b) \simeq (b^3 + \eta_{\rm N} b)/\tau_{\rm N}, \tag{5.50}$$

$$\eta_{\rm N} = \frac{4\pi^2 T^2 \left(\chi_{\rm K}^{\rm N}\right)^2}{n_{\rm N}^2} \tag{5.51}$$

and the time scale

$$\tau_{\rm N} = \left[\frac{-2\,\chi G_F^2}{3\cdot(2\pi)^5}\,\cos^2\theta_c\,\sin^2\theta_c\,m_{\rm n}^{*2} m_{\rm p}^*\,m_\Sigma^*\,k_{\rm F}^\Sigma\,n_{\rm N}^2\left(\chi_{\rm K}^{\rm N}\right)^{-3}\right]^{-1}, \tag{5.52}$$

where χ is determined by the reduced symmetric and antisymmetric coupling constants with typical value ~ 0.1 and $\chi_{\rm K}^{\rm N} \equiv \partial n_{\rm K}/\partial\mu_{\rm K}$ is evaluated at nuclear matter in equilibrium (N). Both $k_{\rm F}^\Sigma$ and $\chi_{\rm K}^{\rm N}$ are functions of $n_{\rm N}$, depending on the nuclear matter EoS. The timescale for relevant weak interactions to happen in nuclear matter is much longer than that in quark matter (Eq. (5.32)), because the baryons are non-relativistic and their densities are lower. For typical transition densities in hybrid stars we studied, the ratio $\tau_{\rm N}/\tau_{\rm Q}$ is of order 10^2.

To estimate the diffusion coefficient $D_{\rm N} \simeq \frac{1}{3} v_{\rm N}\lambda_{\rm N}$ we estimate $v_{\rm N}$ by the Fermi velocity of hyperons ($v_{\rm N} \simeq v_{\rm F}^\Sigma = k_{\rm F}^\Sigma/m_\Sigma^*$), and the mean free path by $\lambda_{\rm N} \simeq v_{\rm F}^\Sigma/\nu_{\rm n\Sigma}$, where $\nu_{\rm n\Sigma}$ is the hadron/hyperon collision frequency similar to the hadron/hadron collision frequency $\nu_{\rm np}$ (see Eq. (55) of [150]). As a result,

$$D_{\rm N} \simeq \frac{m_{\rm n}^2\,{k_{\rm F}^\Sigma}^2}{32\,m_{\rm n}^*\,m_\Sigma^{*4}\,T^2\,S_{\rm n\Sigma}(k_{\rm F}^n, k_{\rm F}^\Sigma)}, \tag{5.53}$$

where $S_{\rm n\Sigma}$ is the effective hadron/hyperon scattering cross section which we for simplicity approximate by the proton/neutron cross section given in Eq. (58) of [150]. Given the nuclear matter EoS, $k_{\rm F}^\Sigma$ and $S_{\rm n\Sigma}$ can be expressed in terms of the baryon density $n_{\rm N}$. The

strangeness diffusion coefficient in nuclear matter is typically much smaller than in quark matter (Eq. (5.33)), because hadrons and hyperons are non-relativistic while quarks are moving nearly at the speed of light and because the long-range interactions between the quark interactions give the different temperature dependence $D_{\rm N}/D_{\rm Q} \propto (T/\mu)^{1/3}$. At temperatures relevant to neutron stars, this ratio is of order 10^{-2}.

The K-fraction in nuclear matter at the boundary with quark matter, $b_{\rm N^\star}$, is constrained by how far out of equilibrium the boundary is. For the boundary to move towards its "ideal" position the total chemical potential per baryon number in beta-equilibrated quark matter (Q in Fig. 5.4) must be larger than that in the non-beta-equilibrated nuclear matter on the other side of the boundary (N*). Following the same logic as in Sec. 5.4.2 we obtain a condition similar to Eq.(5.37)

$$\mu_{\rm B}^{\rm Q} - \mu_{\rm B}^{\rm N} > \frac{\left(-\mu_{\rm K}^{\rm N^\star}\right)^2 \chi_{\rm K}^{\rm N}}{2 n_{\rm N}}. \tag{5.54}$$

From Eq. (5.48), $b_{\rm N^\star} = -n_{\rm K}^{\rm N^\star}/n_{\rm N} \approx -\mu_{\rm K}^{\rm N^\star}\chi_{\rm K}^{\rm N}/n_{\rm N}$, so Eq. (5.54) gives an upper bound on $-b_{\rm N^\star}$ and hence on the front speed $v_{\rm Q\to N}$

$$(-b_{\rm N^\star})^{\rm max} = \sqrt{\frac{2\Delta\mu_{\rm B}\chi_{\rm K}^{\rm N}}{n_{\rm N}}}, \tag{5.55}$$

$$\Delta\mu_{\rm B} = \mu_{\rm B}^{\rm Q} - \mu_{\rm B}^{\rm N} \simeq (\gamma - 1)\delta p/n_{\rm Q}, \tag{5.56}$$

where

$$\delta p = g_{\rm b}\varepsilon_{\rm crit}^{\rm N}(x_{\rm b}(t) - \Delta x_{\rm ib}\sin(\omega t)) \ . \tag{5.57}$$

Assuming that the boundary moves at its maximum speed, $(-b_{\mathrm{N}^\star}) \approx (-b_{\mathrm{N}^\star})^{\max}$, the boundary velocity in the QM $\to$ NM half cycle is

$$\frac{\mathrm{d}\delta x_{\mathrm{b}}}{\mathrm{d}t} \simeq \frac{1}{b_{\mathrm{Q}}}\sqrt{\frac{D_{\mathrm{N}}}{2\tau_{\mathrm{N}}}}\sqrt{\left[\delta z/\ell_{\mathrm{N}}\right]^2 + 2\eta_{\mathrm{N}}\delta z/\ell_{\mathrm{N}}} \tag{5.58}$$

where $\delta z \equiv \delta x_{\mathrm{b}} - \delta x_{\mathrm{ib}}$ is how far the boundary is from its equilibrium position at the current pressure, with the typical length

$$\ell_{\mathrm{N}} = \frac{(n_{\mathrm{N}}/\chi_{\mathrm{K}}^{\mathrm{N}})n_{\mathrm{Q}}}{2(\gamma-1)g_{\mathrm{b}}\varepsilon_{\mathrm{crit}}^{\mathrm{N}}} \ . \tag{5.59}$$

Therefore with the periodic condition $\delta x_{\mathrm{b}}(t) = \delta x_{\mathrm{b}}(2\pi/\omega + t)$, Eq. (5.41) and Eq. (5.58) fully specify the movement of the phase boundary in response to the external pressure oscillation. Next we compute the energy dissipation in this process and see whether it is capable of saturating the r-mode.

5.4.4 Dissipated power and saturation amplitude

From Sec. 5.3.2 we know that during one cycle of an r-mode of amplitude α the energy dissipated in a radially oriented cylinder with an infinitesimal base area $\mathrm{d}S$ straddling the phase boundary at (θ, ϕ) is

$$\mathrm{d}W(\alpha,\theta,\phi) = \mathrm{d}S\,(\gamma-1)\,\Delta p_{\mathrm{N}}\int_0^{\tau}\cos(2\phi+\omega t)\frac{\mathrm{d}\delta R_{\mathrm{b}}}{\mathrm{d}t}\mathrm{d}t \tag{5.60}$$

where the position of the phase boundary $\delta R_{\mathrm{b}}(t)$ is the same as $\delta x_{\mathrm{b}}(t)$ in Sec. 5.4.2 and Sec. 5.4.3, which we assume to move at its maximal speed (see Eqs. (5.41) and (5.58)), and

$\mathrm{d}S = \bar{R}_\mathrm{b}^2 \sin\theta \mathrm{d}\theta \mathrm{d}\phi$. From Eq. (5.23)

$$\Delta p_\mathrm{N} = g_\mathrm{b} \varepsilon_\mathrm{crit}^\mathrm{N} |\delta R_\mathrm{ib}| = \varepsilon_\mathrm{crit}^\mathrm{N} C_\mathrm{b} \alpha |\sin^2\theta \cos\theta| \tag{5.61}$$

Integrating Eq. (5.60) over solid angle gives the total dissipation of the r-mode in one cycle of oscillation and hence the total power dissipated P_dis. The r-mode amplitude stops growing (saturates) when this equals the power injected via back-reaction from gravitational radiation P_gr.

As an illustrative example, Fig. 5.7 shows the dissipated power as a function of r-mode amplitude for a hybrid star rotating with frequency $f = 600\,\mathrm{Hz}$, with quark core size $\bar{R}_\mathrm{b}/R = 0.56$ and temperature $T = 10^8\,\mathrm{K}$. For the quark matter EoS we use the CSS parameterization (Chap. 3) with $n_\mathrm{trans} = 4n_0$, $\Delta\varepsilon/\varepsilon_\mathrm{trans} = 0.2$, and $c_\mathrm{QM}^2 = 1$. The hadronic matter EoS is taken from Ref. [86].

In the subthermal regime, the dissipated power first rises with the r-mode amplitude α as α^3 at very low amplitude, before entering a resonant region with a maximum in P_dis/α^2. At high amplitude in the suprathermal regime, the dissipated power is proportional to α^2. The power in gravitational radiation from the r-mode P_gr (Eq. (B.17)) rises as α^2, and is also shown in Fig. 5.7 for this particular hybrid star. At low amplitude, the phase conversion dissipation is suppressed relative to the gravitational radiation, and therefore plays no role in damping the r-mode. If other damping mechanisms are too weak to suppress the r-mode, its amplitude will grow. However, as the amplitude grows the phase conversion dissipation becomes stronger, and in this example there is a saturation amplitude α_sat at which it equals the gravitational radiation, and the mode stops growing.

Varying parameters such as the size of the quark matter core, rotation frequency or temperature of the star, etc, will shift the curves in Fig. 5.7, and if the phase conversion dissipation is too weak then there will be no intersection point ($P_{\rm gr}$ will be greater than $P_{\rm dis}$ at all α) and phase conversion dissipation will not stop the growth of the mode. However, we can see from Fig. 5.7 that if saturation occurs, the resultant $\alpha_{\rm sat}$ is in the low-amplitude regime, where an analytical approach is available, and the saturation amplitude is extraordinarily low, of order 10^{-12}. This is typical of all model hybrid stars that we investigated. In Appendix B we derive the analytical expression for the dissipated power in the low-amplitude regime (dashed (black) line in Fig. 5.7), obtaining

$$P_{\rm dis}^{\rm sub}(\alpha) \approx \frac{\alpha^3}{15}\left(\frac{105}{756\pi}\right)^{3/2}\frac{\gamma-1}{\Delta\tilde{p}_{\rm N}}\frac{(\varepsilon_{\rm crit}^{\rm N})^2\Omega^7\bar{R}_{\rm b}^{11}}{g_{\rm b}R^3}\ . \tag{5.62}$$

This expression allows us to assess how the strength of phase conversion dissipation depends on the various parameters involved. It is particularly sensitive to the size of the quark core, and this will be important when considering a whole family of hybrid stars with different central pressures and hence different core sizes.

The results of such an investigation are shown in Fig. 5.8, where the solid (red) curve gives the numerically calculated saturation amplitude ($\alpha_{\rm sat}$ in Fig. 5.7) as a function of the size of the quark matter core as a radial fraction of the star, $\bar{R}_{\rm b}/R$. To construct this curve we used the hadronic and quark matter EoS of Fig. 5.7 and varied the central pressure, yielding a family of different star configurations. As $\bar{R}_{\rm b}/R$ decreases, the dissipation power $P_{\rm dis}$ decreases rapidly relative to the gravitational radiation $P_{\rm gr}$. The relative shift in the two corresponding curves in Fig. 5.7 leads to an upper limit on $\alpha_{\rm sat}$ when $P_{\rm gr}$ is tangent to $P_{\rm dis}$. This corresponds to the end of the solid curve in Fig. 5.8 at $\alpha_{\rm sat}^{\rm max}$ at the critical value of the

quark core size, $(\bar{R}_{\rm b}/R)_{\rm crit}$, below which the phase-conversion mechanism cannot saturate the r-mode any more.

The black dashed curve in Fig. 5.8 is the low-amplitude analytical approximation Eq. (B.20) to $\alpha_{\rm sat}$,

$$\begin{aligned}
\alpha_{\rm sat}^{\rm approx} &= \left(\frac{2^{22}\pi^{9/2}}{3^3\cdot 5^{5/2}}\right) G\,\frac{\tilde{D}_{\rm N}}{\tau_{\rm N}}\,\frac{\left(\chi_{\rm K}^{\rm N}\right)^3}{n_{\rm Q} n_{\rm N}^3 b_{\rm Q}^2}\,\frac{g_{\rm b}^3 M^2 \tilde{J}^2}{\Omega}\,\frac{R^9}{\bar{R}_{\rm b}^{11}} \\
&\approx 4.2\times 10^{-11}\,\gamma \left(\frac{\tilde{D}_{\rm N}}{1.5\,{\rm MeV}^3}\right)\left(\frac{\tau_{\rm N}}{2\times 10^{-8}\,{\rm s}}\right)^{-1} \\
&\times \left(\frac{b_{\rm Q}}{1/3}\right)^{-2}\left(\frac{n_{\rm N}}{2\,n_0}\right)^{-4}\left(\frac{\chi_{\rm K}^{\rm N}}{(100\,{\rm MeV})^2}\right)^3\left(\frac{g_{\rm b}}{g_{\rm u}}\right)^3 \\
&\times \left(\frac{\varepsilon_{\rm crit}^{\rm Q}}{2\,\varepsilon_{\rm crit}^{\rm N}}\right)^3\left(\frac{\varepsilon_{\rm crit}^{\rm N}}{600\,{\rm MeV\,fm^{-3}}}\right)^3\left(\frac{M}{1.4\,M_\odot}\right)^2 \\
&\times \left(\frac{\tilde{J}}{0.02}\right)^2\left(\frac{f}{1{\rm kHz}}\right)^{-1}\left(\frac{R}{10\,{\rm km}}\right)\left(\frac{\bar{R}_{\rm b}/R}{0.4}\right)^{-8}
\end{aligned} \tag{5.63}$$

where $D_{\rm N}\equiv \tilde{D}_{\rm N}\cdot T^{-2}$ (see Eq. (5.53)), and $g_{\rm u}$ is the Newtonian gravitational acceleration at the phase boundary when the quark core has uniform density $\varepsilon=\varepsilon_{\rm crit}^{\rm Q}$ ($g_{\rm u}\equiv \frac{4}{3}\pi G\varepsilon_{\rm crit}^{\rm Q}\bar{R}_{\rm b}$). This approximation is very accurate when the the phase conversion damping is strong, but it does not capture the sudden weakening of that dissipation when, for example, the core radius becomes small. It is therefore useful to have some idea of its range of validity.

5.4.5 Range of validity of low-amplitude approximation

The range of validity of Eqs. (5.62) and (5.63) is found by calculating the next-to-leading (NLO) contribution, and requiring that it be less than a fraction ϵ of the total dissipated

power. We find (see Appendix C) that the approximation is valid when

$$\begin{aligned}\epsilon &\geqslant \frac{2^{39}\pi^5}{3^{12}5^4}\frac{G^2}{(\gamma-1)^2}\frac{g_{\rm b}M^4\tilde{J}^4\Omega^6}{\left(\varepsilon^{\rm N}_{\rm crit}\right)^2}\left(\frac{R}{\bar{R}_{\rm b}}\right)^{16}\\ &\simeq 2.96\left(\frac{\gamma-1}{0.5}\right)^{-2}\left(\frac{\varepsilon^{\rm Q}_{\rm crit}}{2\,\varepsilon^{\rm N}_{\rm crit}}\right)^2\left(\frac{g_{\rm b}}{g_{\rm u}}\right)^2\left(\frac{M}{1.4\,M_\odot}\right)^4\\ &\times\left(\frac{\tilde{J}}{0.02}\right)^4\left(\frac{f}{1\,{\rm kHz}}\right)^6\left(\frac{R}{10\,{\rm km}}\right)^2\left(\frac{\bar{R}_{\rm b}/R}{0.4}\right)^{-14}.\end{aligned} \tag{5.64}$$

We see that the validity of the low-amplitude approximation is mainly determined by the size of the quark matter core and the rotation frequency of the star.

5.5 Conclusions

In this chapter we have described how phase conversion in a multi-component compact star provides a mechanism for damping density oscillations, via the phase lag in the response of the interface between components of different baryon densities to the applied pressure oscillation. The phase lag arises from the finite rate of interconversion between the phases, which limits the speed with which the interface can move. We studied the case where the two phases are separated by a sharp boundary (first-order phase transition) and analyzed the movement of the interface in the approximation of a steady state, neglecting additional acceleration effects and complicated hydrodynamic effects like turbulence. In particular, we studied the astrophysically interesting case of the damping of r-mode oscillations [20, 4] in a two-component star. We found that phase conversion dissipation does not affect the r-mode instability region, because it vanishes as α^3 at low r-mode amplitude α. However, depending on the values of relevant parameters, phase conversion dissipation can either saturate the

r-mode at extremely low amplitudes, $\alpha_{\rm sat} \lesssim 10^{-10}$ in the explicit example of hadron-quark transformation at the sharp quark-hadron interface in a hybrid star, or be insufficient to saturate the r-mode at all. The reason for this behavior stems, analogously to the bulk visocity [124], from the resonant character of the dissipation, which is relatively strong when the time scale of the dissipation matches the time scale of the external oscillation (see Fig. 5.7). Whether saturation is possible depends therefore on the microscopic and astrophysical parameters, like in particular on the mass of the quark core which should not be too small.

Our main result is (5.60), which must be evaluated using numerical solutions of (5.41) and (5.58). We also give the low-amplitude analytic expressions for the power dissipated (5.62) and the saturation amplitude (5.63) which are valid when the dissipation is sufficiently strong, obeying (5.64) with $\epsilon \ll 1$.

Our results have significant implications for astrophysical signatures of exotic high-density phases of matter, such as quark matter. The observed data for millisecond pulsars is not consistent with the minimal model of pulsars as stars made of nuclear matter with damping of r-modes via bulk and shear viscosity [36]. Resolving this discrepancy requires either a new mechanism for stabilizing r-modes, or a new mechanism for saturating unstable r-modes at $\alpha_{\rm sat} \lesssim 10^{-8} - 10^{-7}$ [151, 36, 152]. Previously proposed mechanisms have problems to achieve this. Suprathermal bulk viscosity and hydrodynamic oscillations both give $\alpha_{\rm sat} \sim 1$ [120, 117]. The non-linear coupling of the r-mode to viscously damped daughter modes could give $\alpha_{\rm sat} \sim 10^{-6}$ to 10^{-3} [153, 121]. The recently proposed vortex/fluxtube cutting mechanism [122] might give sufficiently small saturation amplitudes but is present only at sufficiently low temperatures $T \ll T_c \lesssim 10^9$ K, which could be exceeded by the r-mode (and/or accretion)

heating [36]. One of the main results of this chapter is that phase conversion dissipation can provide saturation at the required amplitude to explain millisecond pulsar data.

Secondly, due to the extremely low r-mode saturation amplitude of our proposed mechanism hybrid stars would behave very differently from neutron or strange stars. As discussed in [36], if the known millisecond sources were hybrid stars then, for the low saturation amplitudes that we have found, they would have cooled out of the r-mode instability region quickly (in millions of years) so that they would have very low temperatures by now. In contrast, in neutron stars r-modes would be present and would provide such strong heating that the temperature of observed millisecond pulsars would be $T_\infty \sim O(10^5 - 10^6)$ K [36]. This prediction assumes a (so far unknown) saturation mechanism that would saturate the mode at a value $\alpha_{\rm sat} \lesssim 10^{-8}$ required by the pulsar data. This temperature is significantly higher than what standard cooling estimates suggest for such old sources. The same holds for strange quark stars where the enhanced viscous damping can explain the pulsar data, but even in this case the star would spin down along the boundary of the corresponding stability window which would keep it at similarly high temperatures. Measurements of or bounds on temperatures of isolated millisecond pulsars provide therefore a promising way to discriminate hybrid stars.

Our analysis considered only strangeness-changing non-leptonic processes when we discussed the hadron-quark transformation as an example of phase conversion dissipation. However, there are also leptonic processes that equilibrate the non-strange neutron-proton or up-down ratio. For ordinary bulk viscosity in hadronic or quark matter these processes are only relevant at temperatures far above the temperature of a neutron star because their rate is parametrically smaller than the strangeness changing rate discussed here by a factor of $(T/\mu)^2$ [127]. However, leptonic processes might play an important role in phase conversion

dissipation because hadronic matter has more electrons and up quarks than quark matter, so, just as for strangeness, there will be a conversion region behind the moving boundary where conversion and diffusion of up-ness is occurring. Taking this into account could change the estimates given here and should be studied in more detail in the future.

As well as the quark-hadron interface in a hybrid star, any first-order phase transition that leads to a sharp interface between two phases with different baryon densities could, via the mechanism discussed here, cause dissipation of global pressure oscillation modes. One possibility would be different phases of quark matter, perhaps with different Cooper pairing patterns, such as the color-flavor locked (CFL) phase, the 2-flavor color superconductor (2SC) or various forms of inhomogeneous and asymmetric pairing [2], which are all generally connected by first order phase transitions. Because cross-flavor pairing induces shifts in the Fermi surfaces of the participating species, different color superconducting phases will often have different flavor fractions, so movement of the interface between them requires weak interactions, as in the case of the quark-hadron interface. The dissipation mechanism discussed here may therefore be expected to operate, albeit mildly suppressed by the smallness of the baryon number density differences between these phases.

Our discussion was limited to the case of a sharp interface, which is the expected configuration if the surface tension is large enough. If the surface tension is small there will instead be a mixed phase region where domains of charged hadronic and quark matter coexist [45, 46]. We expect that the phase conversion dissipation mechanism will operate in this case too, as the domains expand and shrink in response to pressure oscillations. However, to estimate this contribution is far more complicated since it requires us to consider the dynamic formation, growth, and merging of these structures, taking into account the costs and gains due to surface tension and electric field energy, but we expect that the dissipation due to such

transformations will be roughly comparable to the estimates given here. A similar mechanism should also be relevant for the "nuclear pasta" mixed phases in the inner crust of an ordinary neutron star. In this case in addition to the slow beta equilibration processes there may also be slow strong interaction equilibration processes, whose rate is suppressed by tunneling factors for the transition between geometric domains of different size. This could further enhance the dissipation.

The phase conversion mechanism for damping relies on the transition between two phases being first order. If there is a crossover then dissipation due to particle conversion is described by the standard bulk viscosity. Examples are the appearance of hyperons in the dense interior or the crossover from npe to $npe\mu$ hadronic matter, where the conserved particle density is lepton number instead of baryon number [154]. The conversion is then not restricted to a thin transition region and partial conversion giving rise to bulk viscosity dissipation takes place all over the relevant part of the star. The additional effect, that the size of the region where muons are present changes as well, is negligible, since the muon fraction continuously goes to zero. This is also reflected by the vanishing of the prefactor in the parenthesis of our general expressions Eq. (5.12).

We obtained a reasonable first estimate of the size of the damping by treating the movement of the phase boundary in the steady-state approximation [24], assuming that it can accelerate arbitrarily fast and that it can move as fast as allowed by general thermodynamic constraints. In reality the acceleration of the phase boundary near the turning points of its motion might be further slowed down by the fact that the steady-state conversion region has to form, and if it therefore cannot accelerate fast enough there will be additional dissipation during this part of the cycle, even if the phase boundary is eventually fast enough to stay in chemical equilibrium near the equilibrium position. Our analysis showed that even being out of

chemical equilibrium for only a small fraction of a cycle causes the system to dissipate a huge amount of energy, so it is possible that including these additional acceleration effects may yield an even lower r-mode saturation amplitude and saturate r-modes even in stars with small quark cores. Including the realistic acceleration of the phase boundary will require solving the full time dependent evolution of the phase conversion front. Similarly, it is likely that turbulence plays a major role in the phase conversion, as found in several analyses [144, 143, 155] of the one-time burning of a (meta-stable) neutron star. The inclusion of these complications is an interesting future project.

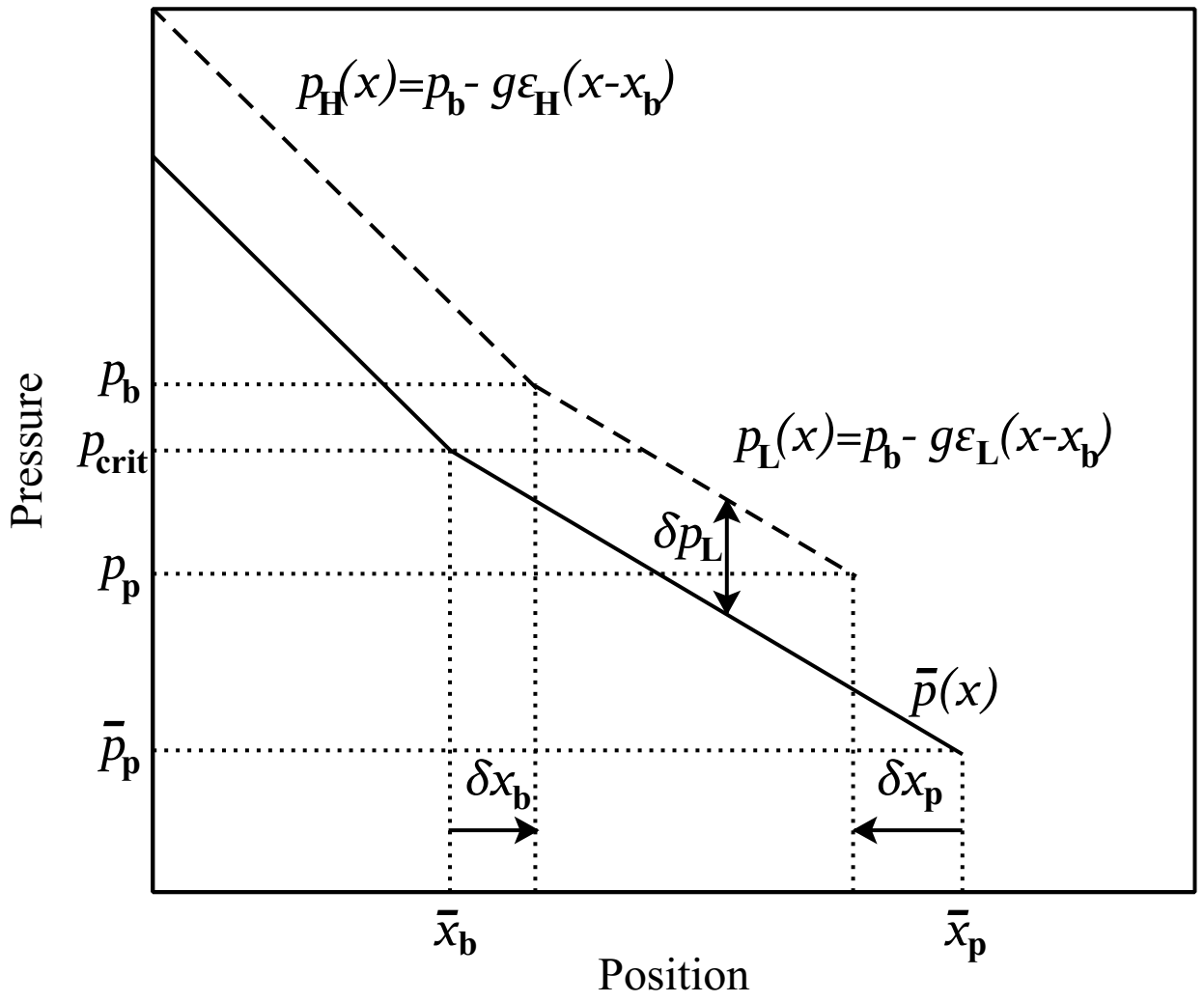

Figure 5.2: Pressure gradients in the cylinder of Fig. 5.1. Solid line $\bar{p}(x)$ is the pressure profile in long-term equilibrium. Dashed line is a snapshot of the system at a moment when the piston has moved inward a distance $\delta x_{\rm p}$, the pressure everywhere has risen, and the phase boundary has moved out a distance $\delta x_{\rm b}$ as the low density phase in part of the region with $p > p_{\rm crit}$ has converted to the high-density phase.

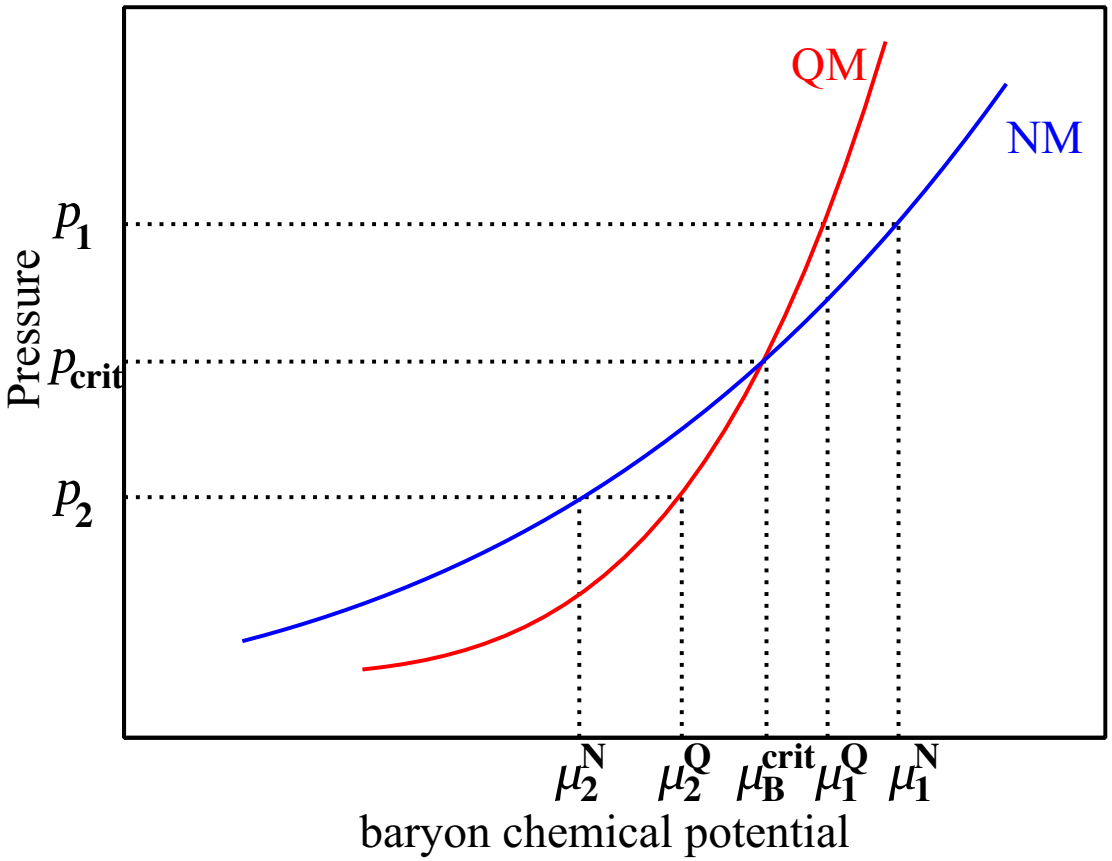

Figure 5.3: Schematic plot of the pressure as a function of baryon chemical potential in beta-equilibrated ($\mu_K = 0$) nuclear matter and quark matter. At a given pressure, the phase with lower μ_B is thermodynamically favored.

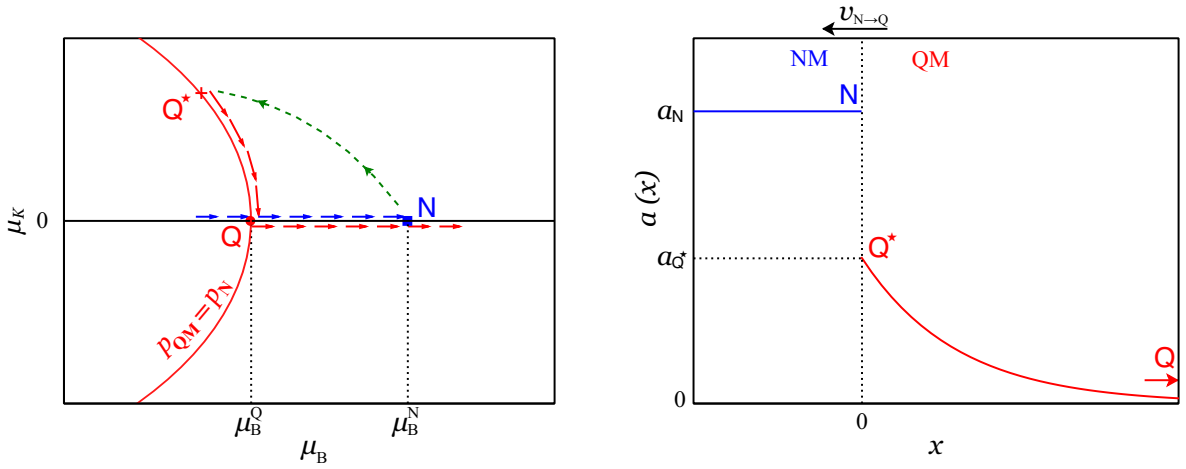

Figure 5.4: Conversion of nuclear matter into quark matter. Right panel: spatial variation of the K-fraction parameter a (Eq. (5.25)) in the conversion region where the pressure is above $p_{\rm crit}$ (see Fig. 5.3). Left panel: corresponding path in the $(\mu_{\rm B}, \mu_{\rm K})$ plane of chemical potentials. The quark matter isobar (red curve) is at the same pressure as the equilibrated nuclear matter (point N), and the arrows follow increasing pressure except from N to Q* to Q where pressure is constant (traversing increasing x in the right panel).

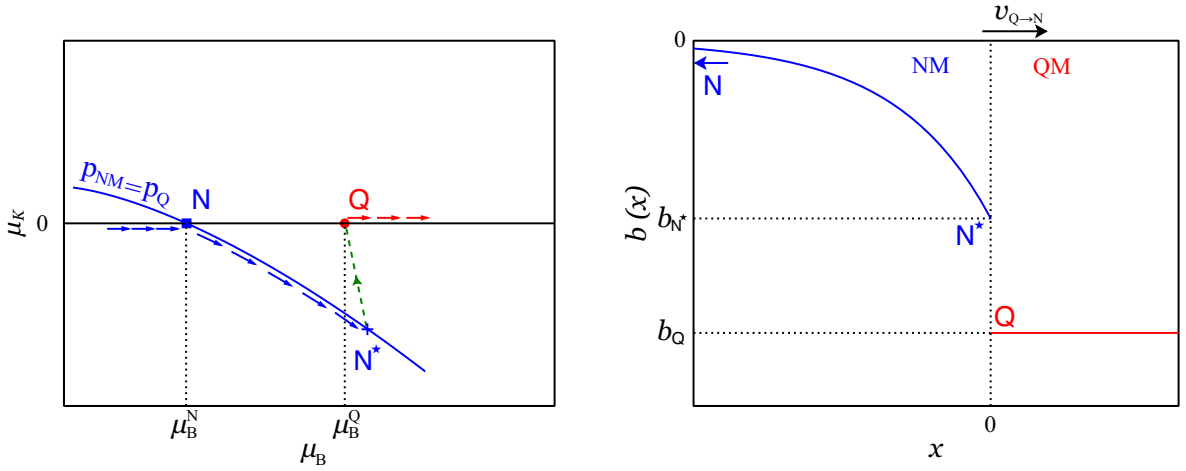

Figure 5.5: Conversion of quark matter into nuclear matter. Right panel: spatial variation of the K-fraction parameter b (Eq. (5.45)) in the conversion region where the pressure is below $p_{\rm crit}$ (see Fig. 5.3). Left panel: corresponding path in the $(\mu_{\rm B}, \mu_{\rm K})$ plane of chemical potentials. The nuclear matter isobar (blue curve) is at the same pressure as the equilibrated quark matter (point Q), and the arrows and the arrows follow increasing pressure except from N to N* to Q where pressure is constant (traversing increasing x in the right panel).

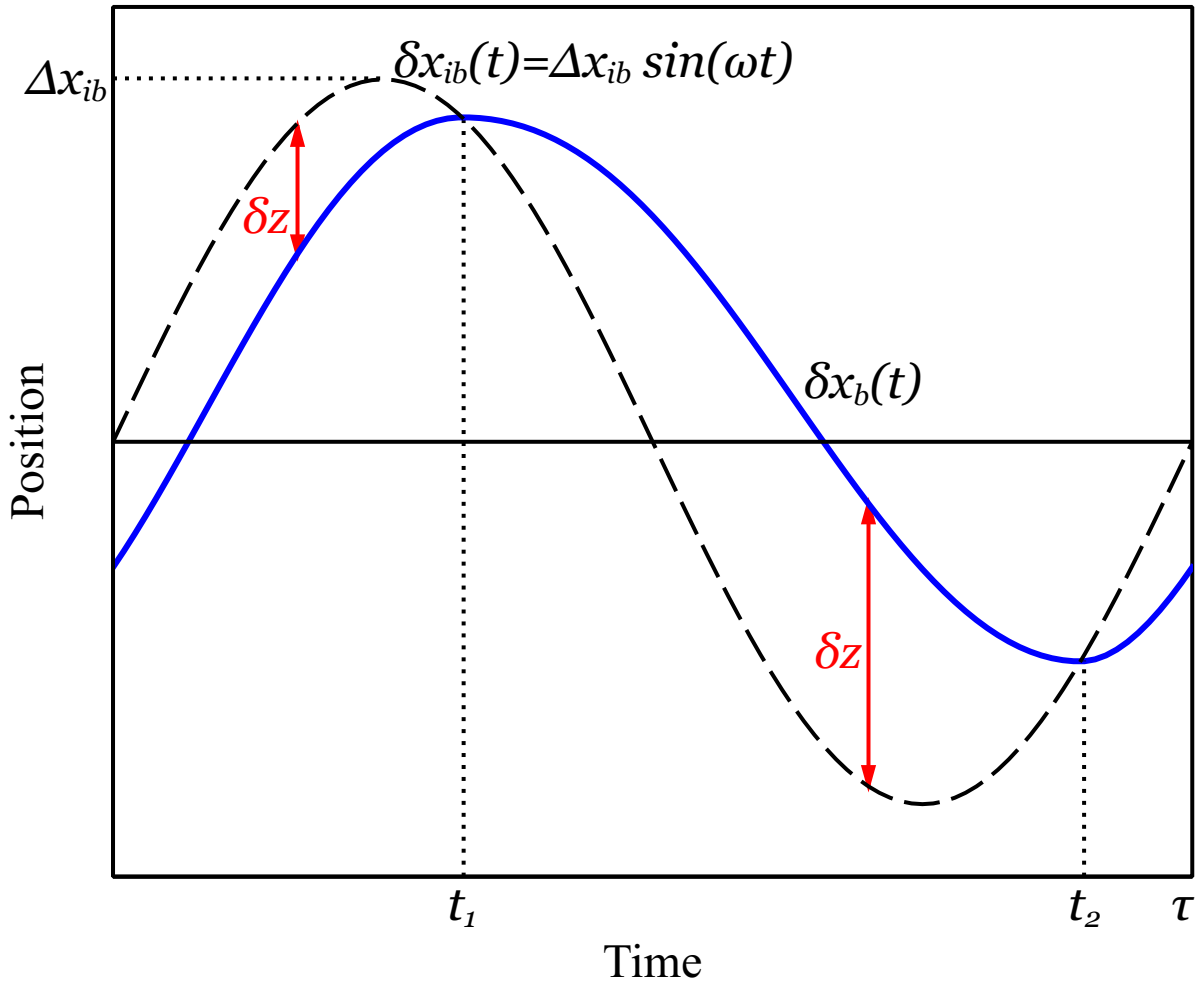

Figure 5.6: Diagram showing how the ideal boundary position (dashed line) and the real boundary position (solid (blue) line) vary in time. The ideal boundary is where the phase boundary would be if the phase conversion process equilibrated instantaneously, and it is determined by the instantaneous external pressure (Eq. (5.9)). The real boundary is always "chasing" the ideal boundary, with velocity given by Eq. (5.41) and (5.58) where $\delta z(t)$ is its distance from the ideal boundary. The real boundary coincides with the ideal boundary twice per cycle, at $t = t_1$ and $t = t_2$.

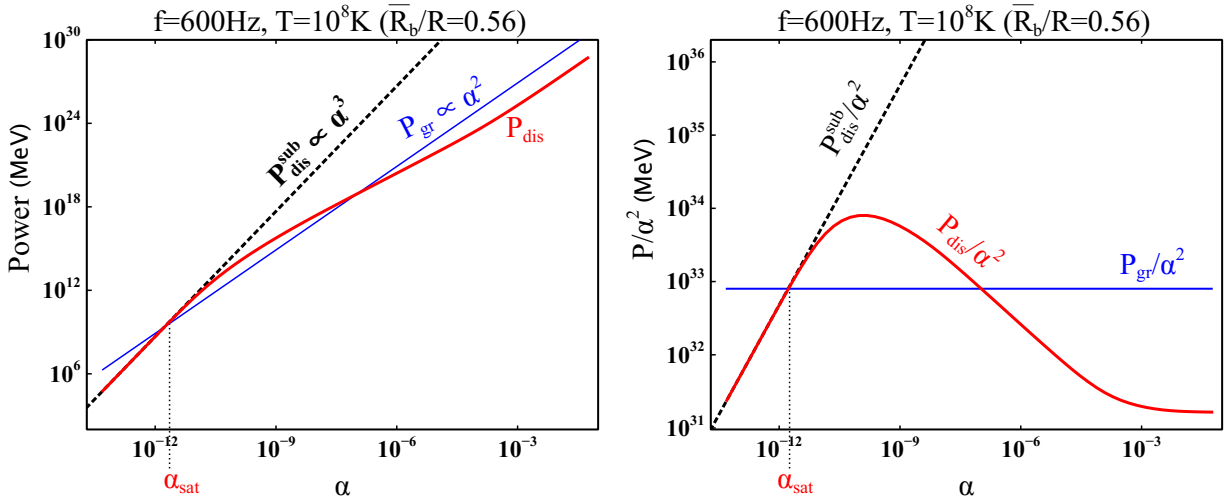

Figure 5.7: The left panel shows dissipated power due to phase conversion $P_{\rm dis}$ (thick solid red curve) as a function of r-mode amplitude α for a specific example hybrid star (see text). The right panel shows the same quantity where the vertical axis now shows the ratio $P_{\rm dis}/\alpha^2$. At first $P_{\rm dis}$ is proportional to α^3 at very low amplitude (dashed line), then at some intermediate amplitude varies less quickly, with a maximum in $P_{\rm dis}/\alpha^2$, and finally changes to α^2 at higher amplitude. Also shown is gravitational radiation power $P_{\rm gr}$ (thin solid blue straight line) which is proportional to α^2 at all amplitudes. The r-mode amplitude will stop growing when dissipation balances radiation, at the first point of intersection between the two curves. This defines the saturation amplitude $\alpha_{\rm sat}$.

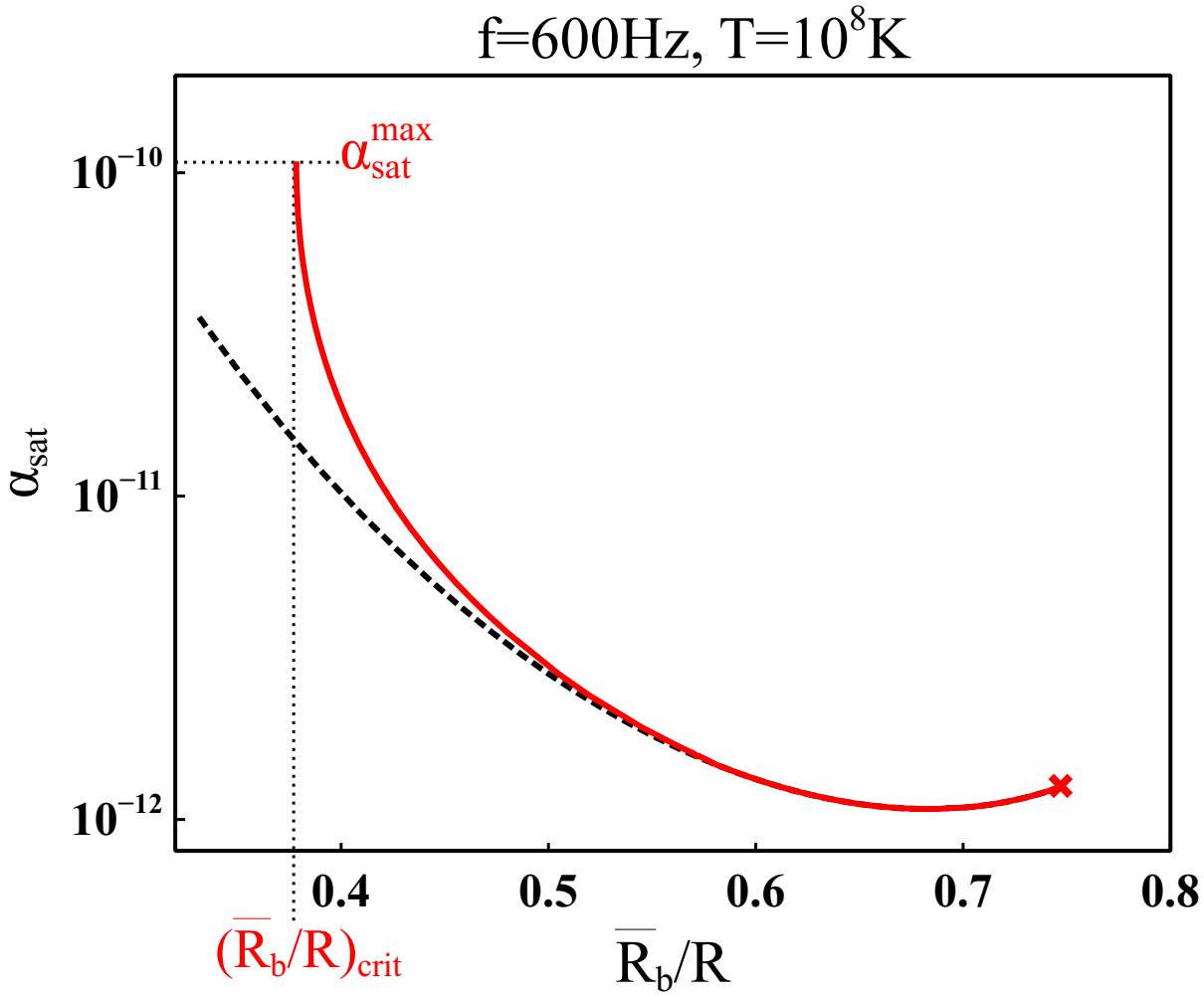

Figure 5.8: R-mode saturation amplitude (red solid curve) and its low-amplitude analytical approximation (black dashed curve) as a function of the radius of the quark matter core $\bar{R}_{\rm b}$ divided by the star radius R in a family of hybrid stars. For $\bar{R}_{\rm b}/R < (\bar{R}_{\rm b}/R)_{\rm crit} \approx 0.38$, damping is too weak to saturate the r-mode. At $\bar{R}_{\rm b}/R \gtrsim 0.75$ the hybrid star is unstable against gravitational collapse. The mass fraction of the core is in the range $0.12 \lesssim M_{\rm core}/M_{\rm star} \lesssim 0.68$ for all the configurations shown on the red solid curve.

Appendix A

Constant-Sound-Speed equation of state

Here we briefly recapitulate (see, e.g., Ref. [77]) the construction of a thermodynamically consistent equation of state of the form in Eq. (3.1)

$$\varepsilon\left(p\right) = \varepsilon_0 + \frac{1}{c^2} p \ . \tag{A.1}$$

We start by writing the pressure in terms of the chemical potential

$$\begin{aligned} p(\mu_B) &= A\,\mu_B^{1+\beta} - B \ , \\ \mu_B(p) &= \left(\frac{p+B}{A}\right)^{1/(1+\beta)} \ . \end{aligned} \tag{A.2}$$

Note that we have introduced an additional parameter A with mass dimension $3-\beta$. The value of A can be varied without affecting the energy-pressure relation (A.1). When constructing a first-order transition from some low-pressure EoS to a high-pressure EoS of the form (A.1), we must choose A so that the pressure is a monotonically increasing function of μ_B (i.e. so that the jump in n_B at the transition is not negative). The derivative with

respect to μ_B yields

$$n_B(\mu_B) = (1+\beta)\, A\, \mu_B^{\beta} \tag{A.3}$$

and using $p = \mu_B n_B - \varepsilon$, we obtain the energy density

$$\varepsilon(\mu_B) = B + \beta\, A\, \mu_B^{1+\beta}\ . \tag{A.4}$$

Then Eq. (A.2) gives energy density as a function of pressure

$$\varepsilon(p) = (1+\beta)B + \beta p \tag{A.5}$$

which is equivalent to Eq. (A.1) with $1/c^2 = \beta$ and $\varepsilon_0 = (1+\beta)B$.

Appendix B

Angular integral and saturation amplitude in the subthermal regime

To determine the velocity of the boundary in the NM $\rightarrow$ QM half cycle, we define a dimensionless parameter $y(\varphi) \equiv \delta x_{\mathrm{b}}/\Delta x_{\mathrm{ib}}$ with $\varphi = \omega t$, then Eq. (5.41) becomes

$$\left(\frac{\mathrm{d}y}{\mathrm{d}\varphi}\right)_{\mathrm{N}\rightarrow\mathrm{Q}} \simeq A_{\mathrm{Q}}\sqrt{\rho_{\mathrm{Q}}(\sin\varphi - y)^2 + (\sin\varphi - y)} \tag{B.1}$$

where A_{Q} represents an overall amplitude of the speed

$$A_{\mathrm{Q}} = \frac{3}{a_{\mathrm{N}}}\sqrt{\frac{D_{\mathrm{Q}}}{2\tau_{\mathrm{Q}}}\frac{(\gamma-1)\eta_{\mathrm{Q}}}{(n_{\mathrm{Q}}/\chi_{\mathrm{K}}^{\mathrm{Q}})n_{\mathrm{Q}}}}\,\frac{g_{\mathrm{b}}\varepsilon_{\mathrm{crit}}^{\mathrm{N}}}{\Omega\sqrt{\Delta p_{\mathrm{N}}}}, \tag{B.2}$$

while ρ_{Q} is the ratio of suprathermal to subthermal contribution

$$\rho_{\mathrm{Q}} = \frac{(\gamma-1)\Delta p_{\mathrm{N}}}{\eta_{\mathrm{Q}}(n_{\mathrm{Q}}/\chi_{\mathrm{K}}^{\mathrm{Q}})n_{\mathrm{Q}}}. \tag{B.3}$$

Similarly in the QM $\rightarrow$ NM half cycle Eq. (5.58) becomes

$$\left(\frac{\mathrm{d}y}{\mathrm{d}\varphi}\right)_{\mathrm{Q}\rightarrow\mathrm{N}} \simeq A_{\mathrm{N}}\sqrt{\rho_{\mathrm{N}}(\sin\varphi - y)^2 + (\sin\varphi - y)} \tag{B.4}$$

and the two coefficients are

$$A_{\mathrm{N}} = \frac{3}{b_{\mathrm{Q}}}\sqrt{\frac{D_{\mathrm{N}}}{2\tau_{\mathrm{N}}}\frac{(\gamma-1)\eta_{\mathrm{N}}}{(n_{\mathrm{N}}/\chi_{\mathrm{K}}^{\mathrm{N}})n_{\mathrm{Q}}}}\frac{g_{\mathrm{b}}\varepsilon_{\mathrm{crit}}^{\mathrm{N}}}{\Omega\sqrt{\Delta p_{\mathrm{N}}}}, \tag{B.5}$$

$$\rho_{\mathrm{N}} = \frac{(\gamma-1)\Delta p_{\mathrm{N}}}{\eta_{\mathrm{N}}(n_{\mathrm{N}}/\chi_{\mathrm{K}}^{\mathrm{N}})n_{\mathrm{Q}}}. \tag{B.6}$$

Combining Eq. (B.1) and Eq. (B.4), and setting $s(\varphi) \equiv \sin\varphi - y(\varphi)$ we have

$$\cos\varphi - \frac{\mathrm{d}s}{\mathrm{d}\varphi} = \begin{cases} A_{\mathrm{N}\rightarrow\mathrm{Q}}\sqrt{\rho_{\mathrm{Q}}s(\varphi)^2 + s(\varphi)}, & s(\varphi) \geqslant 0, \\ A_{\mathrm{Q}\rightarrow\mathrm{N}}\sqrt{\rho_{\mathrm{N}}s(\varphi)^2 - s(\varphi)}, & \text{otherwise.} \end{cases} \tag{B.7}$$

With the periodic condition ($s(\varphi) = s(2\pi + \varphi)$), one can solve for the full profile of the interface position and continue to calculate the dissipated energy.

The total dissipation of the r-mode in one cycle of the oscillation is

$$W(\alpha) = \int_0^{\pi}\int_0^{2\pi} \mathrm{d}S(\gamma-1)\frac{(\Delta p_{\mathrm{N}})^2}{g_{\mathrm{b}}\varepsilon_{\mathrm{crit}}^{\mathrm{N}}}V(\Delta p_{\mathrm{N}}) \tag{B.8}$$

where the integral $V(\Delta p_{\mathrm{N}})$ depends on the velocity of the boundary in both directions

$$V(\Delta p_{\mathrm{N}}) \equiv \int_0^{2\pi} \sin\varphi\,\frac{\mathrm{d}(\sin\varphi - s)}{\mathrm{d}\varphi}\,\mathrm{d}\varphi \tag{B.9}$$

and $s(\varphi)$ is the solution to Eq. (B.7). In general this integral can be computed numerically as long as coefficients A's and ρ's in the differential equation Eq. (B.7) are known.

At small oscillation when $\Delta p_{\rm N}$ is tiny, however, the subthermal regime dominates ($\rho_{\rm Q}, \rho_{\rm N} \ll 1$) and Eq. (B.7) can be simplified as

$$\cos\varphi - \left(\frac{{\rm d}s}{{\rm d}\varphi}\right)_{\rm sub} = \begin{cases} A_{\rm Q}\sqrt{s(\varphi)}, & s(\varphi) \geqslant 0, \\ A_{\rm N}\sqrt{-s(\varphi)}, & \text{otherwise.} \end{cases} \tag{B.10}$$

Since both $A_{\rm Q}$ and $A_{\rm N}$ are much greater than 1, to leading order the analytical solution to Eq. (B.10) is

$$s(\varphi) = \Theta(\cos\varphi)\cdot\frac{\cos^2\varphi}{A_{\rm Q}^2} - \Theta(-\cos\varphi)\cdot\frac{\cos^2\varphi}{A_{\rm N}^2} \tag{B.11}$$

where Θ is the Heaviside step function. The integral Eq. (B.9) becomes

$$\begin{aligned} V_{\rm sub}(\Delta p_{\rm N}) &= \frac{4}{3}\left(\frac{1}{A_{\rm Q}^2} + \frac{1}{A_{\rm N}^2}\right) \\ &= \frac{4}{3}\Delta p_{\rm N}\left(\frac{1}{\Delta\tilde{p}_{\rm Q}} + \frac{1}{\Delta\tilde{p}_{\rm N}}\right) \end{aligned} \tag{B.12}$$

where

$$\Delta\tilde{p}_{\rm Q} \equiv \frac{9}{a_{\rm N}^2}(\gamma-1)\frac{D_{\rm Q}}{\tau_{\rm Q}}\frac{\eta_{\rm Q}\left(g_{\rm b}\varepsilon_{\rm crit}^{\rm N}\right)^2}{n_{\rm Q}\left(n_{\rm Q}/\chi_{\rm K}^{\rm Q}\right)}\frac{1}{\Omega^2}, \tag{B.13}$$

$$\Delta\tilde{p}_{\rm N} \equiv \frac{9}{b_{\rm Q}^2}(\gamma-1)\frac{D_{\rm N}}{\tau_{\rm N}}\frac{\eta_{\rm N}\left(g_{\rm b}\varepsilon_{\rm crit}^{\rm N}\right)^2}{n_{\rm Q}\left(n_{\rm N}/\chi_{\rm K}^{\rm N}\right)}\frac{1}{\Omega^2}. \tag{B.14}$$

At sufficiently low oscillation amplitude , the integral $V_{\rm sub}(\Delta p_{\rm N})$ is dominated by the term with the smaller value of A. For the class of models we have analyzed, in general $A_{\rm Q} \gg A_{\rm N} \gg 1$ ($\Delta\tilde{p}_{\rm Q} \gg \Delta\tilde{p}_{\rm N} \gg \Delta p_{\rm N}$), because in nuclear matter diffusion is less efficient ($D_{\rm N}/D_{\rm Q} \approx O(10^{-2})$) and weak interactions take more time to proceed ($\tau_{\rm N}/\tau_{\rm Q} \approx O(10^2)$). Therefore the

QM $\rightarrow$ NM transition half cycle dominates the dissipation and Eq. (B.12) becomes

$$V_{\rm sub}(\Delta p_{\rm N}) \xrightarrow{\Delta\tilde{p}_{\rm Q}\gg\Delta\tilde{p}_{\rm N}\gg\Delta p_{\rm N}} \frac{4}{3}\Delta p_{\rm N}/\Delta\tilde{p}_{\rm N}. \tag{B.15}$$

Performing the angular integral in Eq. (B.8) gives the expression for dissipated power $P_{\rm dis} \equiv W \cdot (\Omega/2\pi)$ at low amplitude

$$P_{\rm dis}^{\rm sub}(\alpha) \approx \frac{\alpha^3}{15}\left(\frac{105}{756\pi}\right)^{3/2}\frac{\gamma-1}{\Delta\tilde{p}_{\rm N}}\frac{(\varepsilon_{\rm crit}^{\rm N})^2\Omega^7\bar{R}_{\rm b}^{11}}{g_{\rm b}R^3}. \tag{B.16}$$

The power emitted by the mode as gravitational radiation is [156]

$$P_{\rm gr} \equiv \left(\frac{{\rm d}\tilde{E}}{{\rm d}t}\right)_{\rm GR} = \frac{2^{17}\pi}{3^8 5^2}\alpha^2 GM^2R^6\tilde{J}^2\Omega^8 \tag{B.17}$$

The radial integral constant is given by

$$\tilde{J} \equiv \frac{1}{MR^4}\int_0^R \varepsilon(r)r^6{\rm d}r \tag{B.18}$$

and its typical value for hybrid stars is $\simeq 2\times10^{-2}$.

The saturation amplitude $\alpha_{\rm sat}$ is determined by the equation

$$P_{\rm dis} = \left(\frac{{\rm d}\tilde{E}}{{\rm d}t}\right)_{\rm GR} \tag{B.19}$$

Solving Eq. (B.19) with Eqs. (B.14)-(B.18), we obtain the low-amplitude approximation for $\alpha_{\rm sat}$

$$\alpha_{\rm sat}^{\rm approx} = \left(\frac{2^{22}\pi^{9/2}}{3^3\cdot5^{5/2}}\right)G\frac{\tilde{D}_{\rm N}}{\tau_{\rm N}}\frac{\left(\chi_{\rm K}^{\rm N}\right)^3}{n_{\rm Q}n_{\rm N}^3b_{\rm Q}^2}\frac{g_{\rm b}^3M^2\tilde{J}^2}{\Omega}\frac{R^9}{\bar{R}_{\rm b}^{11}} \tag{B.20}$$

where $D_{\rm N} \equiv \tilde{D}_{\rm N}\cdot T^{-2}$ (see Eq. (5.53)).

Appendix C

Range of validity of the analytical approximation for the saturation amplitude

To give an estimate for the validity of the analytic expression for the saturation amplitude, we have to compute Eq. (B.11) to NNLO

$$\begin{aligned} s(\varphi) = \cos^2\varphi & \left[\frac{\Theta(\cos\varphi)}{A_{\mathrm{Q}}^2} - \frac{\Theta(-\cos\varphi)}{A_{\mathrm{N}}^2} \right] \\ & + (4\cos^2\varphi\sin^2\varphi) \left(\frac{1}{A_{\mathrm{Q}}^4} + \frac{1}{A_{\mathrm{N}}^4} \right) \\ & + (-8\cos^4\varphi + 20\cos^2\varphi\sin^2\varphi) \\ & \times \left[\frac{\Theta(\cos\varphi)}{A_{\mathrm{Q}}^6} - \frac{\Theta(-\cos\varphi)}{A_{\mathrm{N}}^6} \right] + ... \end{aligned} \tag{C.1}$$

in order to obtain the NLO correction to Eq. (B.12)

$$V_{\mathrm{sub}}(\Delta p_{\mathrm{N}}) = \frac{4}{3}\left(\frac{1}{A_{\mathrm{Q}}^2}+\frac{1}{A_{\mathrm{N}}^2}\right) - \frac{16}{5}\left(\frac{1}{A_{\mathrm{Q}}^6}+\frac{1}{A_{\mathrm{N}}^6}\right)+... \tag{C.2}$$

This yields the correction term to the dissipated power in the low-amplitude regime

$$P_{\mathrm{dis}}^{\mathrm{sub}}(\alpha) \;=\; P_0(\alpha)+P_1(\alpha)+... \tag{C.3}$$

where P_0 is the previous result Eq. (B.16) and the NLO correction reads

$$P_1(\alpha) \;=\; -\frac{2\alpha^5}{105}\left(\frac{105}{756\pi}\right)^{5/2} \times\frac{\gamma-1}{\left(\Delta\tilde{p}_{\mathrm{N}}\right)^3}\frac{(\varepsilon_{\mathrm{crit}}^{\mathrm{N}})^4\Omega^{11}\bar{R}_{\mathrm{b}}^{17}}{g_{\mathrm{b}}R^5} \tag{C.4}$$

The requirement that the analytical approximation for the saturation amplitude (Eq. (B.20)) deviates from the exact result by less than a fraction ϵ, i.e. $P_1(\alpha_{\mathrm{sat}}^{\mathrm{LO}}) \leqslant \epsilon P_0(\alpha_{\mathrm{sat}}^{\mathrm{LO}})$ yields the bound on the underlying parameters

$$\frac{2^{39}\pi^5}{3^{12}5^4}\frac{G^2}{(\gamma-1)^2}\frac{g_{\mathrm{b}}M^4\tilde{J}^4\Omega^6}{\left(\varepsilon_{\mathrm{crit}}^{\mathrm{N}}\right)^2}\left(\frac{R}{\bar{R}_{\mathrm{b}}}\right)^{16} \;\leqslant\; \epsilon, \tag{C.5}$$

We can see for the set of parameter values on the left-hand side below $\epsilon \ll 1$, Eq. (B.20) is a good approximation. With the EoS we applied in Fig. 5.8, for $\bar{R}_{\mathrm{b}}/R = 0.56$, the left-hand side is ≈ 0.04; for $\bar{R}_{\mathrm{b}}/R = (\bar{R}_{\mathrm{b}}/R)_{\mathrm{crit}} = 0.38$ at $\alpha = \alpha_{\mathrm{sat}}^{\mathrm{max}}$, it is ≈ 4.

References

[1] P. Demorest, T. Pennucci, S. Ransom, M. Roberts, and J. Hessels, *Shapiro Delay Measurement of A Two Solar Mass Neutron Star*, Nature **467** (2010) 1081–1083, [arXiv:1010.5788].

[2] M. G. Alford, A. Schmitt, K. Rajagopal, and T. Schfer, *Color superconductivity in dense quark matter*, Rev.Mod.Phys. **80** (2008) 1455–1515, [arXiv:0709.4635].

[3] N. Glendenning, *Compact stars: Nuclear physics, particle physics, and general relativity*, .

[4] N. Andersson and K. D. Kokkotas, *The R mode instability in rotating neutron stars*, Int.J.Mod.Phys. **D10** (2001) 381–442, [gr-qc/0010102].

[5] R. Schaeffer, L. Zdunik, and P. Haensel, *Phase transitions in stellar cores. I - Equilibrium configurations*, Astron. Astrophys. **126** (Sept., 1983) 121–145.

[6] L. Lindblom, *Phase transitions and the mass radius curves of relativistic stars*, Phys.Rev. **D58** (1998) 024008, [gr-qc/9802072].

[7] J. M. Lattimer and M. Prakash, *What a Two Solar Mass Neutron Star Really Means*, in *From Nuclei To Stars: Festschrift in Honor of Gerald E Brown* (S. Lee, ed.), pp. 275–304. World Scientific, 2011. arXiv:1012.3208.

[8] J. Antoniadis, P. Freire, N. Wex, T. Tauris, R. Lynch, and et al., *A Massive Pulsar in a Compact Relativistic Binary*, Science **340** (2013) 1233232, [arXiv:1304.6875].

[9] A. Akmal, V. Pandharipande, and D. Ravenhall, *The Equation of state of nucleon matter and neutron star structure*, Phys.Rev. **C58** (1998) 1804–1828, [nucl-th/9804027].

[10] S. Gandolfi, J. Carlson, and S. Reddy, *The maximum mass and radius of neutron stars and the nuclear symmetry energy*, Phys.Rev. **C85** (2012) 032801, [arXiv:1101.1921].

[11] I. M. Barbour, S. E. Morrison, E. G. Klepfish, J. B. Kogut, and M.-P. Lombardo, *Results on finite density QCD*, Nucl. Phys. Proc. Suppl. **60A** (1998) 220–234, [hep-lat/9705042].

[12] M. G. Alford, A. Kapustin, and F. Wilczek, *Imaginary chemical potential and finite fermion density on the lattice*, Phys. Rev. **D59** (1999) 054502, [hep-lat/9807039].

[13] J. Cox, C. Gattringer, K. Holland, B. Scarlet, and U. J. Wiese, *Meron-cluster solution of fermion and other sign problems*, Nucl. Phys. Proc. Suppl. **83** (2000) 777–791, [hep-lat/9909119].

[14] S. Hands, *Simulating dense matter*, Prog. Theor. Phys. Suppl. **168** (2007) 253–260, [hep-lat/0703017].

[15] A. R. Bodmer, *Collapsed nuclei*, Phys. Rev. **D4** (1971) 1601–1606.

[16] E. Witten, *Cosmic Separation of Phases*, Phys. Rev. **D30** (1984) 272–285.

[17] J. Madsen, *Physics and astrophysics of strange quark matter*, Lect.Notes Phys. **516** (1999) 162–203, [astro-ph/9809032].

[18] F. Weber, *Strange quark matter and compact stars*, Prog. Part. Nucl. Phys. **54** (2005) 193–288, [astro-ph/0407155].

[19] F. Ozel, D. Psaltis, S. Ransom, P. Demorest, and M. Alford, *The Massive Pulsar PSR J1614-2230: Linking Quantum Chromodynamics, Gamma-ray Bursts, and Gravitational Wave Astronomy*, Astrophys.J. **724** (2010) L199–L202, [arXiv:1010.5790].

[20] N. Andersson, *A New class of unstable modes of rotating relativistic stars*, Astrophys.J. **502** (1998) 708–713, [gr-qc/9706075].

[21] E. Farhi and R. L. Jaffe, *Strange Matter*, Phys. Rev. **D30** (1984) 2379.

[22] T. Sumi, K. Kamiya, A. Udalski, D. Bennett, I. Bond, *et. al.*, *Unbound or Distant Planetary Mass Population Detected by Gravitational Microlensing*, Nature **473** (2011) 349–352, [arXiv:1105.3544].

[23] J. Antoniadis, P. C. Freire, N. Wex, T. M. Tauris, R. S. Lynch, *et. al.*, *A Massive Pulsar in a Compact Relativistic Binary*, Science **340** (2013) 6131, [arXiv:1304.6875].

[24] A. V. Olinto, *On the Conversion of Neutron Stars Into Strange Stars*, Phys.Lett. **B192** (1987) 71.

[25] J. R. Oppenheimer and G. M. Volkoff, *On Massive neutron cores*, Phys. Rev. **55** (1939) 374–381.

[26] S. Chandrasekhar, *Solutions of two problems in the theory of gravitational radiation*, Phys.Rev.Lett. **24** (1970) 611–615.

[27] J. Friedman and B. F. Schutz, *Secular instability of rotating Newtonian stars*, Astrophys.J. **222** (1978) 281.

[28] H.-J. Schulze and T. Rijken, *Maximum mass of hyperon stars with the nijmegen esc08 model*, Phys. Rev. C **84** (Sep, 2011) 035801.

[29] Y. Yamamoto, T. Furumoto, N. Yasutake, and T. A. Rijken, *Hyperon mixing and universal many-body repulsion in neutron stars*, Phys. Rev. C **90** (2014) 045805, [arXiv:1406.4332].

[30] M. M. Nagels, T. A. Rijken, and Y. Yamamoto, *Extended-soft-core Baryon-Baryon Model Esc08 II. Hyperon-Nucleon Interactions*, ArXiv e-prints (2015) [arXiv:1501.0663].

[31] I. Vidaña, D. Logoteta, C. Providência, A. Polls, and I. Bombaci, *Estimation of the effect of hyperonic three-body forces on the maximum mass of neutron stars*, EPL (Europhysics Letters) **94** (2011) 11002, [arXiv:1006.5660].

[32] M. Alford, D. Blaschke, A. Drago, T. Klahn, G. Pagliara, *et. al.*, *Quark matter in compact stars?*, Nature **445** (2007) E7–E8, [astro-ph/0606524].

[33] F. Ozel, G. Baym, and T. Guver, *Astrophysical Measurement of the Equation of State of Neutron Star Matter*, Phys.Rev. **D82** (2010) 101301, [arXiv:1002.3153].

[34] S. Guillot, M. Servillat, N. A. Webb, and R. E. Rutledge, *Measurement of the Radius of Neutron Stars with High S/N Quiescent Low-mass X-ray Binaries in Globular Clusters*, Astrophys.J. **772** (2013) 7, [arXiv:1302.0023].

[35] F. Ozel, D. Psaltis, T. Guver, G. Baym, C. Heinke, *et. al.*, *The Dense Matter Equation of State from Neutron Star Radius and Mass Measurements*, arXiv:1505.0515.

[36] M. G. Alford and K. Schwenzer, *What the Timing of Millisecond Pulsars Can Teach us about Their Interior*, Phys.Rev.Lett. **113** (2014) 251102, [arXiv:1310.3524].

[37] N. Andersson, K. Glampedakis, W. Ho, and C. Espinoza, *Pulsar glitches: The crust is not enough*, Phys.Rev.Lett. **109** (2012) 241103, [arXiv:1207.0633].

[38] J. Piekarewicz, F. Fattoyev, and C. Horowitz, *Pulsar Glitches: The Crust may be Enough*, Phys.Rev. **C90** (2014), no. 1 015803, [arXiv:1404.2660].

[39] C. Alcock, E. Farhi, and A. Olinto, *Strange stars*, Astrophys. J. **310** (1986) 261–272.

[40] M. Stejner and J. Madsen, *Gaps below strange star crusts*, Phys. Rev. **D72** (2005) 123005, [astro-ph/0512144].

[41] V. V. Usov, *Low-mass normal-matter atmospheres of strange stars and their radiation*, Astrophys. J. **481** (1997) L107–L110, [astro-ph/9703037].

[42] P. Jaikumar, S. Reddy, and A. W. Steiner, *The strange star surface: A crust with nuggets*, Phys. Rev. Lett. **96** (2006) 041101, [nucl-th/0507055].

[43] M. G. Alford, K. Rajagopal, S. Reddy, and A. W. Steiner, *The stability of strange star crusts and strangelets*, Phys. Rev. **D73** (2006) 114016, [hep-ph/0604134].

[44] M. G. Alford and D. A. Eby, *Thickness of the strangelet-crystal crust of a strange star*, Phys. Rev. **C78** (2008) 045802, [arXiv:0808.0671].

[45] D. G. Ravenhall, C. J. Pethick, and J. R. Wilson, *Structure of matter below nuclear saturation density*, Phys. Rev. Lett. **50** (1983) 2066–2069.

[46] N. K. Glendenning, *First order phase transitions with more than one conserved charge: Consequences for neutron stars*, Phys. Rev. **D46** (1992) 1274–1287.

[47] M. Alford, C. Kouvaris, and K. Rajagopal, *Evaluating the gapless color-flavor locked phase*, Phys. Rev. **D71** (2005) 054009, [hep-ph/0406137].

[48] R. C. Tolman, *Static solutions of Einstein's field equations for spheres of fluid*, Phys. Rev. **55** (1939) 364–373.

[49] T. Maruyama, S. Chiba, H.-J. Schulze, and T. Tatsumi, *Hadron-quark mixed phase in hyperon stars*, Phys. Rev. **D76** (2007) 123015, [arXiv:0708.3277].

[50] J. Madsen, *Shell model versus liquid drop model for strangelets*, Phys. Rev. **D50** (1994) 3328–3331, [hep-ph/9407314].

[51] P. Amore, M. C. Birse, J. A. McGovern, and N. R. Walet, *Colour superconductivity in finite systems*, Phys. Rev. **D65** (2002) 074005, [hep-ph/0110267].

[52] J. Madsen, *Intermediate mass strangelets are positively charged*, Phys. Rev. Lett. **85** (2000) 4687–4690, [hep-ph/0008217].

[53] J. Madsen, *Color-flavor locked strangelets*, Phys. Rev. Lett. **87** (2001) 172003, [hep-ph/0108036].

[54] J. Madsen, *Universal Charge-Radius Relation for Subatomic and Astrophysical Compact Objects*, Phys. Rev. Lett. **100** (2008) 151102, [arXiv:0804.2140].

[55] M. Oertel and M. Urban, *Surface effects in color superconducting strangelets and strange stars*, Phys. Rev. **D77** (2008) 074015, [arXiv:0801.2313].

[56] M. B. Christiansen and N. K. Glendenning, *Finite size effects and the mixed quark-hadron phase in neutron stars*, Phys. Rev. **C56** (1997) 2858–2864, [astro-ph/9706056].

[57] M. B. Christiansen and J. Madsen, *Inhomogeneity scale from the cosmological quark-hadron transition*, J. Phys. **G23** (1997) 2039–2046.

[58] M. G. Alford, K. Rajagopal, and F. Wilczek, *Color flavor locking and chiral symmetry breaking in high density QCD*, Nucl.Phys. **B537** (1999) 443–458, [hep-ph/9804403].

[59] M. S. Berger and R. L. Jaffe, *Radioactivity in strange quark matter*, Phys. Rev. **C35** (1987) 213–225.

[60] M. S. Berger and R. L. Jaffe, *Erratum: Radioactivity in strange quark matter*, Phys. Rev. C **44** (Jul, 1991) 566.

[61] E. E. Salpeter, *Energy and Pressure of a Zero-Temperature Plasma*, Astrophys. J. **134** (1961) 669–682.

[62] J. M. Bardeen, K. S. Thorne, and D. W. Meltzer, *A Catalogue of Methods for Studying the Normal Modes of Radial Pulsation of General-Relativistic Stellar Models*, The Astrophysical Journal **145** (Aug., 1966) 505.

[63] N. Glendenning, C. Kettner, and F. Weber, *A Possible new class of dense white dwarfs*, Phys.Rev.Lett. **74** (1995) 3519–3521.

[64] A. Bauswein, H.-T. Janka, R. Oechslin, G. Pagliara, I. Sagert, *et. al.*, *Mass Ejection by Strange Star Mergers and Observational Implications*, Phys.Rev.Lett. **103** (2009) 011101, [arXiv:0812.4248].

[65] J. Friedman and R. Caldwell, *Evidence against a strange ground state for baryons*, Phys.Lett. **B264** (1991) 143–148.

[66] A. L. Watts and S. Reddy, *Magnetar oscillations pose challenges for strange stars*, Mon. Not. Roy. Astron. Soc. **379** (2007) L63, [astro-ph/0609364].

[67] M. Mannarelli, K. Rajagopal, and R. Sharma, *The Rigidity of crystalline color superconducting quark matter*, Phys.Rev. **D76** (2007) 074026, [hep-ph/0702021].

[68] J. Sandweiss, *Overview of strangelet searches and Alpha Magnetic Spectrometer: When will we stop searching?*, J.Phys. **G30** (2004) S51–S59.

[69] D. Veras, J. R. Crepp, and E. B. Ford, *Formation, Survival, and Detectability of Planets Beyond 100 AU*, Astrophys.J. **696** (2009) 1600–1611, [arXiv:0902.2779].

[70] M. Bailes, S. Bates, V. Bhalerao, N. Bhat, M. Burgay, *et. al.*, *Transformation of a Star into a Planet in a Millisecond Pulsar Binary*, Science **333** (2011) 1717, [arXiv:1108.5201].

[71] Z. F. Seidov, *The Stability of a Star with a Phase Change in General Relativity Theory*, Sov. Astron. **15** (Oct., 1971) 347.

[72] M. G. Alford, K. Rajagopal, S. Reddy, and F. Wilczek, *The Minimal CFL nuclear interface*, Phys.Rev. **D64** (2001) 074017, [hep-ph/0105009].

[73] L. F. Palhares and E. S. Fraga, *Droplets in the cold and dense linear sigma model with quarks*, Phys.Rev. **D82** (2010) 125018, [arXiv:1006.2357].

[74] M. B. Pinto, V. Koch, and J. Randrup, *The Surface Tension of Quark Matter in a Geometrical Approach*, arXiv:1207.5186.

[75] J. Macher and J. Schaffner-Bielich, *Phase transitions in compact stars*, Eur.J.Phys. **26** (2005) 341–360, [astro-ph/0411295].

[76] K. Masuda, T. Hatsuda, and T. Takatsuka, *Hadron-Quark Crossover and Massive Hybrid Stars*, arXiv:1212.6803.

[77] J. Zdunik and P. Haensel, *Maximum mass of neutron stars and strange neutron-star cores*, Astron. Astrophys. **551** (Mar., 2013) A61, [arXiv:1211.1231].

[78] N. Chamel, A. Fantina, J. Pearson, and S. Goriely, *Maximum mass of neutron stars with exotic cores*, Astron. Astrophys. **553** (2013) A22, [arXiv:1205.0983].

[79] B. Agrawal, *Equations of state and stability of color-superconducting quark matter cores in hybrid stars*, Phys.Rev. **D81** (2010) 023009, [arXiv:1001.1584].

[80] L. Bonanno and A. Sedrakian, *Composition and stability of hybrid stars with hyperons and quark color-superconductivity*, Astron.Astrophys. **539** (2012) A16, [arXiv:1108.0559].

[81] R. Lastowiecki, D. Blaschke, H. Grigorian, and S. Typel, *Strangeness in the cores of neutron stars*, Acta Phys.Polon.Supp. **5** (2012) 535–540, [arXiv:1112.6430].

[82] A. Kurkela, P. Romatschke, A. Vuorinen, and B. Wu, *Looking inside neutron stars: Microscopic calculations confront observations*, arXiv:1006.4062.

[83] A. Kurkela, P. Romatschke, and A. Vuorinen, *Cold Quark Matter*, Phys.Rev. **D81** (2010) 105021, [arXiv:0912.1856].

[84] M. Alford, M. Braby, M. Paris, and S. Reddy, *Hybrid stars that masquerade as neutron stars*, Astrophys.J. **629** (2005) 969–978, [nucl-th/0411016].

[85] G. Shen, C. Horowitz, and S. Teige, *A New Equation of State for Astrophysical Simulations*, Phys.Rev. **C83** (2011) 035802, [arXiv:1101.3715].

[86] K. Hebeler, J. Lattimer, C. Pethick, and A. Schwenk, *Constraints on neutron star radii based on chiral effective field theory interactions*, Phys.Rev.Lett. **105** (2010) 161102, [arXiv:1007.1746].

[87] J. M. Lattimer and Y. Lim, *Constraining the Symmetry Parameters of the Nuclear Interaction*, arXiv:1203.4286.

[88] A. W. Steiner, J. M. Lattimer, and E. F. Brown, *The Equation of State from Observed Masses and Radii of Neutron Stars*, Astrophys. J.**722** (2010), no. 1 33, [arXiv:1005.0811].

[89] J. L. Zdunik, P. Haensel, and R. Schaeffer, *Phase transitions in stellar cores. II - Equilibrium configurations in general relativity*, Astron. Astrophys. **172** (Jan., 1987) 95–110.

[90] A. B. Migdal, A. Chernoutsan, and I. Mishustin, *Pion condensation and dynamics of neutron stars*, Phys.Lett. **B83** (1979) 158–160.

[91] B. Kämpfer, *On stabilizing effects of relativity in cold spheric stars with a phase transition in the interior*, Physics Letters B **101** (May, 1981) 366–368.

[92] N. K. Glendenning and C. Kettner, *Possible third family of compact stars more dense than neutron stars*, Astron. Astrophys. **L9** (2000) 353.

[93] K. Schertler, C. Greiner, J. Schaffner-Bielich, and T. M. H., *Quark phases in neutron stars and a "third family" of compact stars as a signature for phase transitions*, Nucl. Phys. **A677** (2000) 463, [astro-ph/0001467].

[94] V. Thorsson, M. Prakash, and J. M. Lattimer, *Composition, Structure, and Evolution of Neutron Stars with Kaon Condenstaes*, Nucl. Phys. **A572** (1994) 693.

[95] E. S. Fraga, R. D. Pisarski, and J. Schaffner-Bielich, *Small, dense quark stars from perturbative QCD*, Phys. Rev. **D63** (2001) 121702, [hep-ph/0101143].

[96] S. Banik and D. Bandyopadhyay, *Color superconducting quark matter core in the third family of compact stars*, Phys. Rev. **D67** (2003) 123003.

[97] J. Zdunik, M. Bejger, P. Haensel, and E. Gourgoulhon, *Phase transitions in rotating neutron stars cores: back bending, stability, corequakes and pulsar timing*, Astron.Astrophys. **450** (2006) 747–758, [astro-ph/0509806].

[98] I. Mishustin, M. Hanauske, A. Bhattacharyya, L. Satarov, H. Stoecker, *et. al.*, *Catastrophic rearrangement of a compact star due to the quark core formation*, Phys.Lett. **B552** (2003) 1–8, [hep-ph/0210422].

[99] L.-M. Lin, K. Cheng, M.-C. Chu, and W.-M. Suen, *Gravitational waves from phase-transition induced collapse of neutron stars*, Astrophys.J. **639** (2006) 382–396, [astro-ph/0509447].

[100] J. M. Lattimer and M. Prakash, *The Ultimate energy density of observable cold matter*, Phys.Rev.Lett. **94** (2005) 111101, [astro-ph/0411280].

[101] M. G. Alford, S. Han, and M. Prakash, *Generic conditions for stable hybrid stars*, Phys.Rev. **D88** (2013), no. 8 083013, [arXiv:1302.4732].

[102] P. F. Bedaque and A. W. Steiner, *Sound velocity bound and neutron stars*, Phys.Rev.Lett. **114** (2015) 031103, [arXiv:1408.5116].

[103] T. Gross-Boelting, C. Fuchs, and A. Faessler, *Covariant representations of the relativistic Bruckner T matrix and the nuclear matter problem*, Nucl.Phys. **A648** (1999) 105–137, [nucl-th/9810071].

[104] G. Taranto, M. Baldo, and G. Burgio, *Selecting microscopic Equations of State*, Phys.Rev. **C87** (2013) 045803, [arXiv:1302.6882].

[105] A. V. Yudin, T. L. Razinkova, D. K. Nadyozhin, and A. D. Dolgov, *Special point on the mass-radius diagram of hybrid stars*, Astronomy Letters **40** (apr, 2014) 201–211, [arXiv:1404.0865].

[106] J. M. Lattimer, *The nuclear equation of state and neutron star masses*, Ann.Rev.Nucl.Part.Sci. **62** (2012) 485–515, [arXiv:1305.3510].

[107] J. M. Lattimer, "Neutron stars and core-collapse supernovae." APS 2015 April Meeting. http://meetings.aps.org/link/BAPS.2015.APR.R9.1.

[108] A. Di Giacomo, H. G. Dosch, V. Shevchenko, and Y. Simonov, *Field correlators in QCD: Theory and applications*, Phys.Rept. **372** (2002) 319–368, [hep-ph/0007223].

[109] Y. Simonov and M. Trusov, *Deconfinement transition for nonzero baryon density in the field correlator method*, JETP Lett. **85** (2007) 598–601, [hep-ph/0703228].

[110] Y. Simonov and M. Trusov, *Vacuum phase transition at nonzero baryon density*, Phys.Lett. **B650** (2007) 36–40, [hep-ph/0703277].

[111] I. Bombaci and D. Logoteta, *A link between measured neutron star masses and lattice QCD data*, Monthly Notices of the Royal Astronomical Society - Letters, Vol. 433, **L79-L83** (2013) [arXiv:1212.5907].

[112] S. Plumari, G. Burgio, V. Greco, and D. Zappala, *Quark matter in Neutron Stars within the Field Correlator Method*, Phys.Rev. **D88** (2013), no. 8 083005, [arXiv:1307.3055].

[113] M. Baldo, P. Castorina, and D. Zappala, *Gluon condensation and deconfinement critical density in nuclear matter*, Nucl.Phys. **A743** (2004) 3–12, [nucl-th/0311038].

[114] M. Baldo, G. Burgio, P. Castorina, S. Plumari, and D. Zappala, *Astrophysical constraints on the confining models: The Field Correlator Method*, Phys.Rev. **D78** (2008) 063009, [arXiv:0804.2328].

[115] S. Benic, D. Blaschke, D. E. Alvarez-Castillo, T. Fischer, and S. Typel, *A new quark-hadron hybrid equation of state for astrophysics - I. High-mass twin compact stars*, arXiv:1411.2856.

[116] A. Ayriyan, D. Alvarez-Castillo, D. Blaschke, H. Grigorian, and M. Sokolowski, *New Bayesian analysis of hybrid EoS constraints with mass-radius data for compact stars*, arXiv:1412.8226.

[117] L. Lindblom, J. E. Tohline, and M. Vallisneri, *Nonlinear evolution of the r modes in neutron stars*, Phys.Rev.Lett. **86** (2001) 1152–1155, [astro-ph/0010653].

[118] P. Arras, E. E. Flanagan, S. M. Morsink, A. K. Schenk, S. A. Teukolsky, *et. al.*, *Saturation of the R mode instability*, Astrophys.J. **591** (2003) 1129–1151, [astro-ph/0202345].

[119] R. Bondarescu, S. A. Teukolsky, and I. Wasserman, *Spin Evolution of Accreting Neutron Stars: Nonlinear Development of the R-mode Instability*, Phys.Rev. **D76** (2007) 064019, [arXiv:0704.0799].

[120] M. G. Alford, S. Mahmoodifar, and K. Schwenzer, *Viscous damping of r-modes: Large amplitude saturation*, Phys.Rev. **D85** (2012) 044051, [arXiv:1103.3521].

[121] R. Bondarescu and I. Wasserman, *Nonlinear Development of the R-Mode Instability and the Maximum Rotation Rate of Neutron Stars*, Astrophys.J. **778** (2013) 9, [arXiv:1305.2335].

[122] B. Haskell, K. Glampedakis, and N. Andersson, *A new mechanism for saturating unstable r-modes in neutron stars*, Mon.Not.Roy.Astron.Soc. **441** (2014) 1662, [arXiv:1307.0985].

[123] J. Madsen, *Bulk viscosity of strange quark matter, damping of quark star vibration, and the maximum rotation rate of pulsars*, Phys.Rev. **D46** (1992) 3290–3295.

[124] M. G. Alford, S. Mahmoodifar, and K. Schwenzer, *Large amplitude behavior of the bulk viscosity of dense matter*, J.Phys. **G37** (2010) 125202, [arXiv:1005.3769].

[125] M. G. Alford, S. Reddy, and K. Schwenzer, *Bridging the Gap by Squeezing Superfluid Matter*, Phys.Rev.Lett. **108** (2012) 111102, [arXiv:1110.6213].

[126] R. Sawyer, *Bulk viscosity of hot neutron-star matter and the maximum rotation rates of neutron stars*, Phys.Rev. **D39** (1989) 3804–3806.

[127] P. Haensel and R. Schaeffer, *Bulk viscosity of hot-neutron-star matter from direct URCA processes*, Phys.Rev. **D45** (1992) 4708–4712.

[128] P. Haensel, K. Levenfish, and D. Yakovlev, *Bulk viscosity in superfluid neutron star cores. I. direct urca processes in npe mu matter*, Astron.Astrophys. **357** (2000) 1157–1169, [astro-ph/0004183].

[129] P. Haensel, K. Levenfish, and D. Yakovlev, *Bulk viscosity in superfluid neutron star cores. 2. Modified Urca processes in npe mu matter*, Astron.Astrophys. **327** (2001) 130–137, [astro-ph/0103290].

[130] P. Haensel, K. Levenfish, and D. Yakovlev, *Bulk viscosity in superfluid neutron star cores. 3. Effects of sigma- hyperons*, Astron.Astrophys. **381** (2002) 1080–1089, [astro-ph/0110575].

[131] P. B. Jones, *Bulk viscosity of neutron star matter*, Phys.Rev. **D64** (2001) 084003.

[132] M. G. Alford and A. Schmitt, *Bulk viscosity in 2SC quark matter*, J.Phys. **G34** (2007) 67–102, [nucl-th/0608019].

[133] C. Manuel and F. J. Llanes-Estrada, *Bulk viscosity in a cold CFL superfluid*, JCAP **0708** (2007) 001, [arXiv:0705.3909].

[134] M. G. Alford, M. Braby, S. Reddy, and T. Schfer, *Bulk viscosity due to kaons in color-flavor-locked quark matter*, Phys.Rev. **C75** (2007) 055209, [nucl-th/0701067].

[135] M. Mannarelli and C. Manuel, *Bulk viscosities of a cold relativistic superfluid: Color-flavor locked quark matter*, Phys.Rev. **D81** (2010) 043002, [arXiv:0909.4486].

[136] X. Wang and I. A. Shovkovy, *Bulk viscosity of spin-one color superconducting strange quark matter*, Phys.Rev. **D82** (2010) 085007, [arXiv:1006.1293].

[137] K. Schwenzer, *How long-range interactions tune the damping in compact stars*, arXiv:1212.5242.

[138] C. Manuel, J. Tarrus, and L. Tolos, *Bulk viscosity coefficients due to phonons in superfluid neutron stars*, JCAP **1307** (2013) 003, [arXiv:1302.5447].

[139] L. Lindblom, B. J. Owen, and G. Ushomirsky, *Effect of a neutron star crust on the r mode instability*, Phys.Rev. **D62** (2000) 084030, [astro-ph/0006242].

[140] M. Alford, S. Mahmoodifar, and K. Schwenzer, *Viscous damping of r-modes: Small amplitude instability*, Phys.Rev. **D85** (2012) 024007, [arXiv:1012.4883].

[141] I. Tokareva and A. Nusser, *On the possibility of combustion of neutrons into strange quark matter*, Phys.Lett. **B639** (2006) 232–236, [astro-ph/0502344].

[142] R. Mallick, A. Bhattachryya, S. K. Ghosh, and S. Raha, *Conversion of nuclear to 2-flavour quark matter in rotating compact stars: A general relativistic perspective*, arXiv:0806.1800.

[143] M. Herzog and F. K. Ropke, *Three-dimensional hydrodynamic simulations of the combustion of a neutron star into a quark star*, Phys.Rev. **D84** (2011) 083002, [arXiv:1109.0539].

[144] G. Pagliara, M. Herzog, and F. K. Rpke, *Combustion of a neutron star into a strange quark star: The neutrino signal*, Phys.Rev. **D87** (2013), no. 10 103007, [arXiv:1304.6884].

[145] R. Ouyed, D. Leahy, and P. Jaikumar, *Predictions for signatures of the quark-nova in superluminous supernovae*, arXiv:0911.5424.

[146] T. Chan, K. Cheng, T. Harko, H. Lau, L. Lin, *et. al.*, *Could the compact remnant of SN 1987A be a quark star?*, Astrophys.J. **695** (2009) 732–746, [arXiv:0902.0653].

[147] J. Madsen, *Rate of the weak reaction s + u to u + d in quark matter*, Phys.Rev. **D47** (1993) 325–330.

[148] H. Heiselberg and C. Pethick, *Transport and relaxation in degenerate quark plasmas*, Phys.Rev. **D48** (1993) 2916–2928.

[149] J. Schaffner and I. N. Mishustin, *Hyperon rich matter in neutron stars*, Phys.Rev. **C53** (1996) 1416–1429, [nucl-th/9506011].

[150] P. Shternin and D. Yakovlev, *Shear viscosity in neutron star cores*, Phys.Rev. **D78** (2008) 063006, [arXiv:0808.2018].

[151] S. Mahmoodifar and T. Strohmayer, *Upper Bounds on r-mode Amplitudes from Observations of Low-mass X-Ray Binary Neutron Stars*, Astrophys.J. **773** (2013) 140, [arXiv:1302.1204].

[152] B. Haskell, N. Degenaar, and W. C. Ho, *Constraining the physics of the r-mode instability in neutron stars with X-ray and UV observations*, Mon.Not.Roy.Astron.Soc. **424** (2012) 93, [arXiv:1201.2101].

[153] J. Brink, S. A. Teukolsky, and I. Wasserman, *Nonlinear couplings of R-modes: Energy transfer and saturation amplitudes at realistic timescales*, Phys.Rev. **D70** (2004) 121501, [gr-qc/0406085].

[154] M. G. Alford and G. Good, *Leptonic contribution to the bulk viscosity of nuclear matter*, Phys.Rev. **C82** (2010) 055805, [arXiv:1003.1093].

[155] B. Niebergal, R. Ouyed, and P. Jaikumar, *Numerical Simulation of the Hydrodynamical Combustion to Strange Quark Matter*, Phys.Rev. **C82** (2010) 062801, [arXiv:1008.4806].

[156] L. Lindblom, B. J. Owen, and S. M. Morsink, *Gravitational radiation instability in hot young neutron stars*, Phys.Rev.Lett. **80** (1998) 4843–4846, [gr-qc/9803053].

[157] S. Banerjee, A. Bhattacharyya, S. K. Ghosh, S. Raha, B. Sinha, *et. al.*, *Massive Compact Halo Objects from the relics of the cosmic quark - hadron transition*, Mon.Not.Roy.Astron.Soc. **340** (2003) 284, [astro-ph/0211560].

[158] A. Y. Potekhin and G. Chabrier, *Equation of state of fully ionized electron - ion plasmas. 2. Extension to relativistic densities and to the solid phase*, Phys.Rev. **E62** (2000) 8554–8563, [astro-ph/0009261].

[159] M. G. Alford, J. A. Bowers, and K. Rajagopal, *Crystalline color superconductivity*, Phys. Rev. **D63** (2001) 074016, [hep-ph/0008208].

[160] R. Casalbuoni and G. Nardulli, *Inhomogeneous superconductivity in condensed matter and QCD*, Rev. Mod. Phys. **76** (2004) 263–320, [hep-ph/0305069].

[161] H. Heiselberg, *Screening in quark droplets*, Phys. Rev. **D48** (1993) 1418–1423.

[162] Y. Lyubarsky, D. Eichler, and C. Thompson, *Diagnosing magnetars with transient cooling*, Astrophys. J. **580** (2002) L69–L72, [astro-ph/0211110].

[163] A. I. Chugunov, *Seismic signatures of strange stars with crust*, Mon. Not. Roy. Astron. Soc. **371** (2006) 363–368, [astro-ph/0606310].

[164] A. Burrows, S. Reddy, and T. A. Thompson, *Neutrino opacities in nuclear matter*, Nucl. Phys. **A777** (2006) 356–394, [astro-ph/0404432].

[165] D. Page and V. V. Usov, *Thermal Evolution and Light Curves of Young Bare Strange Stars*, Phys. Rev. Lett. **89** (2002) 131101, [astro-ph/0204275].

[166] P. Jaikumar, C. Gale, D. Page, and M. Prakash, *Distinguishing bare quark stars from neutron stars*, Int. J. Mod. Phys. **A19** (2004) 5335–5342, [astro-ph/0407091].

[167] T. Harko and K. S. Cheng, *Photon emissivity of the electrosphere of bare strange stars*, Astrophys. J. **622** (2005) 1033–1043, [astro-ph/0412280].

[168] O. L. Caballero, S. Postnikov, C. J. Horowitz, and M. Prakash, *Shear Viscosity of the outer crust of Neutron stars: Ion Contribution*, arXiv:0807.4353.

[169] J. Madsen, *Probing strange stars and color superconductivity by r- mode instabilities in millisecond pulsars*, Phys. Rev. Lett. **85** (2000) 10–13, [astro-ph/9912418].

[170] P. Jaikumar, G. Rupak, and A. W. Steiner, *Viscous damping of r-mode oscillations in compact stars with quark matter*, arXiv:0806.1005.

[171] O. Y. Gnedin, D. G. Yakovlev, and A. Y. Potekhin, *Thermal relaxation in young neutron stars*, Mon. Not. Roy. Astron. Soc. **324** (2001) 725, [astro-ph/0012306].

[172] A. R. Zhitnitsky, *'Nonbaryonic' dark matter as baryonic color superconductor*, JCAP **0310** (2003) 010, [hep-ph/0202161].

[173] M. M. Forbes, K. Lawson, and A. R. Zhitnitsky, *The electrosphere of macroscopic 'quark nuclei': A source for diffuse MeV emissions from dark matter*, arXiv:0910.4541.

[174] E. W. Weisstein, "Jacobi elliptic functions.." From MathWorld–A Wolfram Web Resource. http://mathworld.wolfram.com/JacobiEllipticFunctions.html.

[175] E. F. Brown, *Nuclear Heating and Melted Layers in the Inner Crust of an Accreting Neutron Star*, The Astrophysical Journal **531** (Mar., 2000) 988–1002, [astro-ph/].

[176] J. M. Lattimer, K. A. van Riper, M. Prakash, and M. Prakash, *Rapid cooling and the structure of neutron stars*, The Astrophysical Journal **425** (Apr., 1994) 802–813.

[177] N. K. Glendenning and F. Weber, *Nuclear solid crust on rotating strange quark stars*, The Astrophysical Journal **400** (Dec., 1992) 647–658.

[178] L. Bildsten and G. Ushomirsky, *Viscous Boundary-Layer Damping of R-Modes in Neutron Stars*, Astrophys. J. Lett. **529** (Jan., 2000) L33–L36, [astro-ph/].

[179] B. Kampfer, *On the possibility of stable quark and pion condensed stars*, J.Phys. **A14** (1981) L471–L475.

[180] S. C. Pieper, R. B. Wiringa, and J. Carlson, *Quantum Monte Carlo calculations of excited states in A = 6 - 8 nuclei*, Phys.Rev. **C70** (2004) 054325, [nucl-th/0409012].

[181] J. Negele and H. Orland, *Quantum Many-Particle Systems*. Addison-Wesley, Reading, MA, 1st ed., 1988.

[182] J. E. Hirsch, *Discrete Hubbard-Stratonovich transformation for fermion lattice models*, Phys. Rev. **B28** (1983) 4059–4061.

[183] M. Prakash, J. Cooke, and J. Lattimer, *Quark - hadron phase transition in protoneutron stars*, Phys.Rev. **D52** (1995) 661–665.

[184] H.-J. Schulze and T. Rijken, *Maximum mass of hyperon stars with the Nijmegen ES C-08 model*, Phys.Rev. **C84** (2011) 035801.

[185] Y. Yamamoto, T. Furumoto, N. Yasutake, and T. A. Rijken, *Hyperon mixing and universal many-body repulsion in neutron stars*, Phys.Rev. **C90** (2014), no. 4 045805, [arXiv:1406.4332].

[186] I. Vidana, D. Logoteta, C. Providencia, A. Polls, and I. Bombaci, *Estimation of the effect of hyperonic three-body forces on the maximum mass of neutron stars*, Europhys.Lett. **94** (2011) 11002, [arXiv:1006.5660].

[187] T. Katayama and K. Saito, *Neutron stars with Hyperons in Dirac-Brueckner-Hartree-Fock approach*, arXiv:1410.7166.

[188] T. Kojo, P. D. Powell, Y. Song, and G. Baym, *Phenomenological QCD equation of state for massive neutron stars*, Phys.Rev. **D91** (2015), no. 4 045003, [arXiv:1412.1108].

[189] S. Benic, *Heavy hybrid stars from multi-quark interactions*, Eur.Phys.J. **A50** (2014) 111, [arXiv:1401.5380].

[190] D. E. Alvarez-Castillo, S. Benić, D. Blaschke, and R. Łastowiecki, *Crossover transition to quark matter in heavy hybrid stars*, Acta Phys.Polon.Supp. **7** (2014), no. 1 203–208, [arXiv:1311.5112].

[191] M. Baldo, ed., *Nuclear Methods and The Nuclear Equation of State*. World Scientific, Singapore, 1999.

[192] B. Day, *Three-body correlations in nuclear matter*, Phys.Rev. **C24** (1981) 1203–1271.

[193] H. Song, M. Baldo, G. Giansiracusa, and U. Lombardo, *Bethe-Brueckner-Goldstone Expansion in Nuclear Matter*, Phys.Rev.Lett. **81** (1998) 1584–1587.

[194] M. Baldo, A. Fiasconaro, H. Q. Song, G. Giansiracusa, and U. Lombardo, *High density symmetric nuclear matter in the Bethe-Brueckner-Goldstone approach*, Phys.Rev. **C65** (2002) 017303.

[195] M. Baldo, A. Polls, A. Rios, H.-J. Schulze, and I. Vidana, *Comparative study of neutron and nuclear matter with simplified Argonne nucleon-nucleon potentials*, Phys.Rev. **C86** (2012) 064001, [arXiv:1207.6314].

[196] M. Baldo, I. Bombaci, and G. Burgio, *Microscopic nuclear equation of state with three-body forces and neutron star structure*, Astron.Astrophys. **328** (1997) 274–282, [astro-ph/9707277].

[197] X. R. Zhou, G. F. Burgio, U. Lombardo, H.-J. Schulze, and W. Zuo, *Three body forces and neutron star structure*, Phys.Rev. **C69** (2004) 018801.

[198] R. B. Wiringa, V. Stoks, and R. Schiavilla, *An Accurate nucleon-nucleon potential with charge independence breaking*, Phys.Rev. **C51** (1995) 38–51, [nucl-th/9408016].

[199] J. Carlson, V. Pandharipande, and R. B. Wiringa, *Three-nucleon interaction in 3-body, 4-body, and infinite-body systems*, Nucl.Phys. **A401** (1983) 59–85.

[200] R. Schiavilla, V. Pandharipande, and R. B. Wiringa, *Momentum distributions in a A = 3 and 4 nuclei*, Nucl.Phys. **A449** (1986) 219–242.

[201] Z. Li, U. Lombardo, H.-J. Schulze, and W. Zuo, *Consistent nucleon-nucleon potentials and three-body forces*, Phys.Rev. **C77** (2008) 034316.

[202] Z. Li and H. Schulze, *Nuclear matter with chiral forces in Brueckner-Hartree-Fock approximation*, Phys.Rev. **C85** (2012) 064002.

[203] M. Baldo, G. Burgio, and H. Schulze, *Onset of hyperon formation in neutron star matter from Brueckner theory*, Phys.Rev. **C58** (1998) 3688–3695.

[204] M. Baldo, G. Burgio, and H. Schulze, *Hyperon stars in the Brueckner-Bethe-Goldstone theory*, Phys.Rev. **C61** (2000) 055801, [nucl-th/9912066].

[205] G. Brown and W. Weise, *Relativistic Effects in Nuclear Physics*, Comments Nucl.Part.Phys. **17** (1987) 39.

Vita

Sophia Han

Degrees

B.S. Materials Science and Engineering, June 2009
Ph.D. Physics, August 2015

Publications

Mark G. Alford, Sophia Han and Sanjay Reddy (2012). *Strangelet dwarfs*, Journal of Physics G: Nuclear and Particle Physics, **39** 065201,

Mark G. Alford, Sophia Han and Madappa Prakash (2013). *Generic conditions for stable hybrid stars*, Physical Review D, **88** 083013,

Mark G. Alford, Sophia Han and Kai Schwenzer (2014). *Phase conversion dissipation in multicomponent compact stars*, Physical Review C, **91**, 055804,

Mark G. Alford, Fiorella Burgio, Sophia Han, Gabriele Taranto and Dario Zappala (2015). *Constraining and applying a generic high-density equation of state*, under review.

Mark G. Alford and Sophia Han (2015). *Characteristics of hybrid compact stars with a sharp hadron-quark interface*, under review.

August 2015